UNIVERSITY OF OKLAHOMA

GRADUATE COLLEGE

TRANSPORT AND SPECTROSCOPIC STUDIES OF LIQUID AND POLYMER ELECTROLYTES

A DISSERTATION

SUBMITTED TO THE GRADUATE FACULTY

in partial fulfillment of the requirements for the

Degree of

DOCTOR OF PHILOSOPHY

By

DHARSHANI NIMALI BOPEGE
Norman, Oklahoma
2012

TRANSPORT AND SPECTROSCOPIC STUDIES OF LIQUID AND POLYMER ELECTROLYTES

A DISSERTATION APPROVED FOR THE
HOMER L. DODGE DEPARTMENT OF PHYSICS AND ASTRONOMY

BY

Dr. John Moore-Furneaux, Chair

Dr. Roger E. Frech

Dr. Daniel T. Glatzhofer

Dr. Michael B. Santos

Dr. Xinyu Dai

This dissertation is dedicated to my loving parents.

Acknowledgements

First of all, I am thankful to the Department of Physics, University of Oklahoma for giving me an opportunity to pursue my degree in this great place and for providing me with financial support during past years. I am greatly thankful for all wonderful people who helped me through this journey, which would not have been possible without their personal support. I especially want to thank my advisor in Physics, **Dr. John Furneaux** for your valuable guidance during my research. I appreciate your help to understanding the instrument problems and time spent teaching me how to deal with problems. I am profoundly thankful to my advisor in Chemistry, **Dr. Roger Frech** for giving me such a wonderful opportunity to work in Frech group and for the guidance and advice you have given me to understand the research problems and to develop my carrier. I am grateful to my other committee members, **Dr. Danial Glatzhofer**, **Dr. Mike Santos**, and **Dr. Xinyu Dai** for their guidance and great support for my graduate studies. Also, I would like to thank my former committee members, **Dr. Eddie Baron**, **Dr. Sheena Murphy**, and **Dr. Ralph Wheeler**. In addition, I am thankful to **Dr. Powell** for knowledge and support he provided me to resolve crystal structures.

I was very fortunate to have excellent and very professional colleagues. **Allison Fleshman**, **Rachel Mason**, **Gwen Giffin**, and **Nathalie Rocher**, I wish to give my sincere gratitude for your friendship, numerous support for my research, and encouragement provided during hard times. Some work in this thesis would not be possible without the great help of **Matt Petrowsky** and I am grateful to you.

Priyanta Wijesinghe, **Kosala Ekanayake**, thank you both for your friendship and listening to my stories. I am also thankful to all Sri Lankan friends who made me feel like I am in my home country. I would like to give my sincere thanks to **Danette Loyd** and **Debbi Barnhill** in physics office staff and entire chemistry office staff for all your help on my paperwork and TA duties.

Finally, this dissertation is not possible without the love, encouragement, and patience of my family. My parents, **Sumanadasa and Kamala Bopege**, I am deeply grateful for you always there for me being when I needed you, and I am indebted to both of you for your unconditional love, care, support and strength you given for me all these years to pursue my dreams. I feel proud of my siblings, **Awanthi and Nuwan Bopege** for their achievements and I am thankful for your support past years. I am also grateful to my in-laws, **Hemachandra and Rupa Maddumage** for their love and understanding. Finally, none of this have been possible without my beloved husband, **Hemantha Maddumage**. During past years, your love, encouragement, understanding and support is appreciated, and I am blessed to have a husband like you. I love you.

Table of Contents

List of Tables

List of Figures

Abstract

Liquid and polymer electrolytes are interesting and important materials to study as they are used in Li rechargeable batteries and other electrochemical devices. It is essential to investigate the fundamental properties of electrolytes such as ionic conductivity, diffusion, and ionic association to enhance battery performance in different battery markets. This dissertation mainly focuses on the temperature-dependent charge and mass transport processes and ionic association of different electrolyte systems. Impedance spectroscopy and pulsed field gradient nuclear magnetic resonance spectroscopy were used to measure the ionic conductivity and diffusion coefficients of ketone and acetate based liquid electrolytes. In this study, charge and mass transport in non-aqueous liquid electrolytes have been viewed from an entirely different perspective by introducing the compensated Arrhenius formalism. Here, the conductivity and diffusion coefficient are written as an Arrhenius-like expression with a temperature-dependent static dielectric constant dependence in the exponential prefactor. The compensated Arrhenius formalism reported in this dissertation very accurately describes temperature-dependent conductivity data for acetate and ketone-based electrolytes as well as temperature-dependent diffusion data of pure solvents. We found that calculated average activation energies of ketone-based electrolytes are close to each other for both conductivity and diffusion data (in the range 24-26 kJ/mol). Also, this study shows that average activation energies of acetate-based electrolytes are higher than those for the ketone systems (in the range 33-37 kJ/mol). Further, we observed

higher dielectric constants and ionic conductivities for both dilute and concentrated ketone solutions with temperature.

Vibrational spectroscopy (Infrared and Raman) was used to probe intermolecular interactions in both polymer and liquid electrolytes, particularly those which contain lithium trifluoromethanesulfonate, $LiCF_3SO_3$, abbreviated here as lithium triflate(LiTf). The molar absorption coefficients of $\nu_s(SO_3)$, $\delta_s(CF_3)$, and $\delta_s(SO_3)$ vibrational modes of triflate anion in the LiTf-2-pentanone system were found to be 6708±89, 5182±62, and 189±2 kg mol^{-1} cm^{-1}, respectively using Beer-Lambert law. Our results show that there is strong absorption by $\nu_s(SO_3)$ mode and weak absorption by $\delta_s(CF_3)$ mode. Also, the absorptivity of each mode is independent of the ionic association with Li ions. This work allows for the direct quantitative comparison of calculated concentrations in different samples and different experimental conditions. In addition, this dissertation reports the temperature-dependent vibrational spectroscopic studies of pure poly(ethylene oxide) and LiTf-poly(ethylene oxide) complexes.

A significant portion of this dissertation focuses on crystallographic studies of ketone-salt (LiTf:2-pentanone and NaTf:2-hexanone) and amine-acid (diethyleneamine: H_3PO_4, N,N'-dimethylethylenediamine:H_3PO_4, and piperazine:H_3PO_4) systems. Here, sodium trifluoromethanesulfonate, $NaCF_3SO_3$ is abbreviated as NaTf. As model compounds, these systems provide valuable information about ion-ion interactions, which are helpful for understanding complex polymer systems. During this study, five crystal structures were solved using single X-ray diffractometry, and their vibrational modes were studied in the mid-infrared region. In the

secondary amine/phosphoric acid systems, the nature of hydrogen-bonding network was examined.

Chapter 1

Introduction

Today, we are dependent on fossil fuels more than anytime during human history. However, unless we are able to find alternatives to oil and gas, the whole civilization could face an inevitable disaster in the near future as these resources are limited and not replenished naturally at the rate we consume them. Another adverse effect of fossil fuel is the air pollution that can also lead to global warming. A considerable effort has been put into alternative energy research, such as rechargeable battery technology, hydrogen fuel cell technology, wind energy, and solar energy. Finding more efficient, convenient, and pollution-free secondary energy sources is a major goal of future energy research.

Currently, Li-ion rechargeable battery technology has emerged as a viable power source since it has several advantages over conventional batteries (nickel, cadmium, and lead based systems). They are largely used in portable electronic devices, automobile industry, and military and aerospace applications. Li-ion batteries have a great demand due to their high power density, cell voltages, lack of memory effect, low environmental impact, and light weight. During the past years, researchers have studied ways to enhance battery performance and to develop new materials that can be used as anodes, cathodes and electrolytes [1–4].

In addition to Li-ion batteries, hydrogen-based fuel cells are another form of power generation. According to the Hydrogen Fuel Initiative (HFI) program introduced in 2003, research is aimed to producing hydrogen fuel cell vehicles by

2020 [5]. Fuel cells have uses in a wide range of applications such as transportation and stationary power generation, with large and small scale.

1.1 Li Battery and Fuel Cell Basics

1.1.1 Li rechargeable battery

There are two types of batteries available commercially: primary and secondary batteries. A primary battery cannot be used more than once because it cannot recharge after a complete discharge. On the other hand, a secondary battery is rechargeable and can be used multiple times. There are various types of secondary batteries available in the market: lead-acid, nickel cadmium (NiCd), nickel metal hydride (NiMH), lithium ion (Li-ion), and lithium ion polymer (Li-ion polymer) to name a few. The Li ion rechargeable battery has highest energy density per unit volume (Wh/l) and per unit weight (Wh/kg) compared to the conventional nickel batteries such as NiCd and NiMH [3, 4]. As a clean energy source, the demand of Li-ion batteries is increasing exponentially in the market. Therefore, it has the potential to be a promising power source for the future portable electronic devices such as laptops, cellular phones, digital cameras, MP3 players, iPods, power tools and hybrid electric vehicles (HEV).

An electrical battery is a combination of one or more electrochemical cells. In general, a cell consists of a positive (cathode) and a negative (anode) electrode, an electrolyte, and a separator. Often the electrolyte is the separator. Fig.1.1 shows the schematic diagram of a Li rechargeable battery. In the anode, the oxidation

process occurs, donating electrons. The reduction process happens at the cathode by accepting these electrons. For an example:

The anode reaction: $Li(C) \rightleftharpoons Li^+ + e^-$

The cathode reaction: $Li^+ + e^- + CoO_2 \rightleftharpoons LiCoO_2$

Overall reaction: $Li^+ + CoO_2 \rightleftharpoons LiCoO_2$

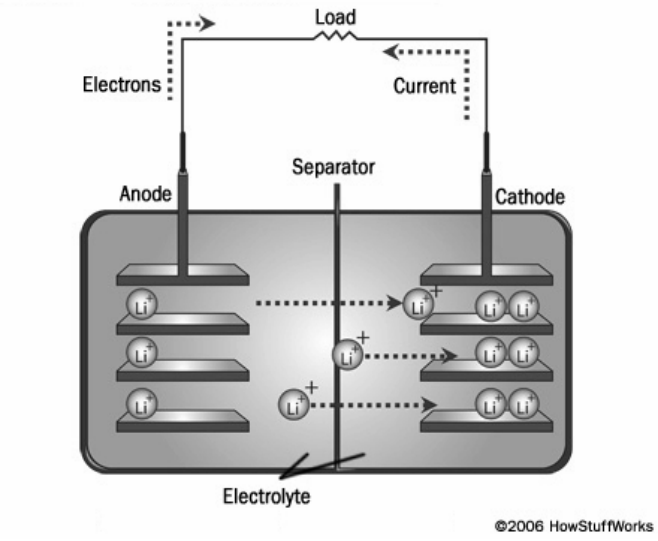

Figure 1.1: Schematic diagram of Li-ion battery

Several anode, cathode, and electrolyte materials are used in a commercially available Li ion rechargeable batteries. The major anode-active materials are graphite and hard carbons. Metal oxides such as $LiCoO_2$, $LiMn_2O_4$, $LiNiO_2$, $LiFePO_4$, and Li_2FePO_4F are several materials that are used as cathodes.

An electrolyte in an Li-ion battery is a mixture of two or more organic liquids and an inorganic salt dissolved in the liquid. Ethylene carbonate (EC), dimethyl carbonate (DMC), and diethyl carbonate (DEC) are favorable organic liquids used

in electrolytes. Further, $LiPF_6$, $LiBF_4$, $LiClO_4$ are widely used lithium salts in the battery industry. The separator is a barrier between the anode and cathode, which prevents contact between electrodes. A good electrolyte should possess several characteristic features: good ionic conductivity, good chemical stability, low-cost and environmental compatibility. Therefore, an immense amount of research has been carried out to develop new materials to use as an electrolyte in Li-ion battery.

1.1.2 Fuel cells

A fuel cell is an electrochemical device that generates an electric current by a chemical reaction of fuel and oxygen. Major components of a fuel cell are the anode (negative electrode), the cathode (positive electrode) and the electrolyte. A catalyst is used to increase the chemical reaction rate at the electrodes. Fuel cells are categorized into several types depending on the fuel and the electrolyte used, as well as the composition of the electrodes. The hydrogen fuel cell is the most common among these. Fig. 1.2 illustrates the block diagram of a fuel cell. Hydrogen gas in the anode oxidizes and creates positively charged cations and negatively charged electrons. These positive ions travel through the medium of the electrolyte, while the electron passes through a wire to the external circuit to produce an electric current. When the positive ions reach the cathode, they react with the oxygen supplied from the cathode. In some fuel cells, oxygen reacts with positive ions and electrons arriving from the electrical circuit and produces water and heat at the cathode. In hydrocarbon fuel cells, carbon dioxide forms as a waste product in addition to water. Choosing a material to be used as the electrolyte is a key

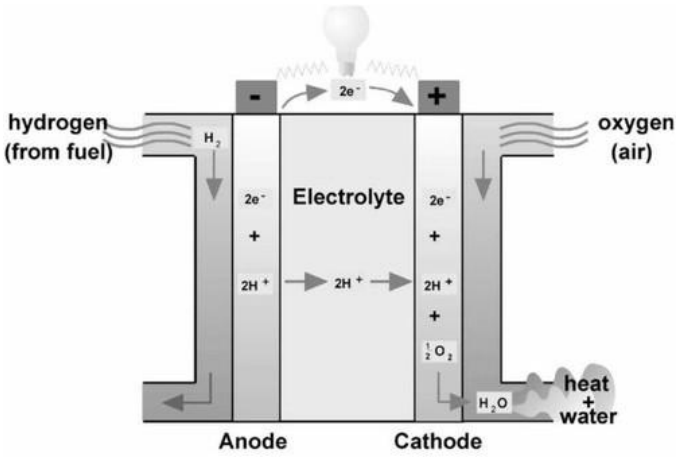

Figure 1.2: Schematic diagram of a PEM fuel cell [6]

step of fuel cell production. A few commonly used liquid electrolytes are alkalines, molten carbonate salts, phosphoric acid, while proton exchange membranes (PEMs) and solid oxides are some examples of solid electrolytes. For instance, alkaline fuel cells (AFC) use a potassium hydroxide/water mixture as their electrolytes and they are mostly utilized in spacecraft and military applications. Both molten carbonate and solid oxide fuel cells have applications in distributed generation and electric utilities. The electrolyte of a molten carbonate fuel cell is sodium or magnesium carbonate, while the solid oxide fuel cell uses a ceramic oxide; *e.g.* calcium or zirconium oxide. Phosphoric acid fuel cells are widely used in power generation applications and PEM fuel cells that employ polymer electrolytes as electrolytes have applications in transportation, portable and backup power fields. However, more efficient techniques to be developed to handle temperature and waste products.

1.2 Polymer Electrolytes

A polymer electrolyte (PE) is made by dissolving a salt in a polymer. Alkali metal salts are favorable in the electrochemical device industry because they provide large electrochemical potentials. According to Gray [7], a PE is "A (liquid) solvent-free system where the ionically conducting phase is formed by dissolving salts in a high molecular weight polar polymer matrix." Moreover, other materials categorized as gel electrolytes, plasticized electrolytes, or ionic rubbers are also referred to as polymer electrolytes. In the past few decades, polymer electrolytes have been intensively studied. In 1973, Fenton *et al.* reported the first poly(ethylene oxide)/alkali salt complexes [8]. Later, Wright and co-workers discovered the high conductivities of these materials (1975) [9]. In 1979, Armand *et al.* introduced the usage of PEs in electrochemical devices [10]. The most widely used salts in PEs are lithium trifluoromethanesulfonate ($LiCF_3SO_3$), lithium percholorte ($LiClO_4$), lithium hexafluorophosphate ($LiPF_6$), and lithium trifluoroborate ($LiBF_4$).

Polymer systems are generally biphasic at room temperature, consisting of crystalline and amorphous regions. Amorphous regions of a polymer are characterized by a glass transition temperature (T_g), which is the transition temperature between the rigid (glass) and viscous states. Basically, ionic conduction occurs in the amorphous region and, hence, exhibits higher conductivities than the crystalline phase. Polyethylene oxide (PEO) and polyethylene glycol (PEG) serve as the favorite host polymers for PEs among researchers. Polymers consist of repeated units of identical structures [7, 11–13]; Fig. 1.3 shows the chemical structural

formula of PEO.

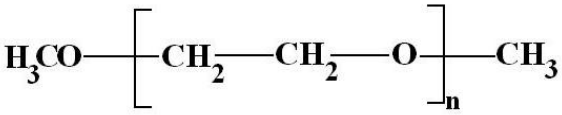

Figure 1.3: Chemical formula of poly(ethylene oxide)-PEO

Polymer electrolytes are characterized by a number of material properties. Among these, ionic conductivity, transport number, and diffusion coefficient are of most importance due to their practical relevance. Early work shows a vast number of studies in this field using different techniques [14–17]. Motions of the polymer segments are part of the ionic transport mechanism. The motion of dissociated ions in the polymer matrix is correlated with this segmental motion. During the past few decades, research groups have studied various polymer systems and obtained results supporting this view [18]. Segmental motion of polymer chains is accompanied by ionic association or ionic diffusion. When a salt is added, lone electron pairs on ether oxygens of the polymer interact with the cations forming a coordinative bond. Cations can form transient cross-links between chain segments. Cations diffuse through the polymer system by breaking and forming new coordination bonds with the heteroatoms of the polymer matrix [7]. The nature of ion transport at the molecular level in polymer electrolytes is poorly understood. It is essential to study the chemical properties which are correlated with ion transport mechanism.

1.3 Liquid Electrolytes

Liquid electrolytes are made by dissolving salts in organic solvents. In the Li ion battery industry, different liquid electrolytes are utilized. Generally two or more organic liquids are mixed to make the electrolyte, i.e. carbonates, acetates, etc. Organic solvent molecules that can donate protons (H^+) are known as protic solvents. These solvents show hydrogen bonding; alcohols, formic acid, and water are examples of protic solvents. Solvents that cannot donate protons are called aprotic solvents, e.g. acetates, ketones, nitriles, and carbonates. All the data reported in this thesis were obtained for aprotic solvents. Similar to the polymer electrolytes, understanding the ion and mass transport of the liquid electrolytes is an interesting field. Studying ionic conductivities, diffusion coefficients, dielectric constants, ionic associations, and ion solvation provides important information about ion transport [19].

The work reported here is based on aprotic solvents that are used to make liquid electrolytes. N-acetates and 2-ketones were utilized to study the fundamental properties of liquid electrolytes. N-acetate has a low dielectric constant and 2-ketone has a high dielectric constant. Solvents with dielectric constants lower than 10 are characterized here as low dielectric electrolytes. For instance, Table 1.1 shows dielectric constants of several solvents. The temperature dependence of ionic conductivity and diffusion were studied for liquid electrolytes and pure liquids, respectively. Dilute electrolytes were prepared with 0.0055 mol/L concentration. Concentrated electrolytes were made at 0.3 and 0.8 mol/kg molal concentrations.

Table 1.1: Dielectric constants and dipole moments of several aprotic solvents. D* is the gas phase diploe moment

Solvent	Dielectric constant	Dipole moment (D)*
Ethyl acetate	6.0	1.78 D
Tetrahydrofuran	7.5	1.75 D
Acetone	21	2.88 D
acetonitrile	37	3.92 D

Studying the concentration-dependent molar conductivities of liquid electrolytes that are made from low dielectric constant solvents is quite interesting. Fig. 1.4 shows a schematic diagram of the variation of molar conductivities with salt concentration. In region I, the molar conductivity decreases with the increasing salt concentration. At the starting point of region II, molar conductivity has a minimum value and then it increases to a maximum value. In region III, molar conductivity decreases. Different groups have given explanations based on their observations. Primarily, they point out that the ionic association gives rise to region I and II behavior. A low dielectric constant medium is favorable to ion-ion interactions. As a result, more uncharged ion pairs form from free ions, which decreases the molar conductivity. The increase of the molar conductivity in region II has been described using different postulates. Fuoss and Kraus interpreted this behavior as being due to triple ion formation [20]. These triple ions are formed by combining ion pairs and free ions in the solution. Cavell and Knight introduced a different concept about the increasing molar conductivity in region II. According

to them, ion pairs can dissociate or redissociate to "free" ions [21]. However, molar conductivity variation in region I and II is seen in many tetrabutylammonium trifluoromethanesulfonate (TbaTf) systems, where ionic association does not occur. Therefore, above interpretation is not valid for all liquid electrolyte systems. The ionic association may play a some role in LiTf systems.

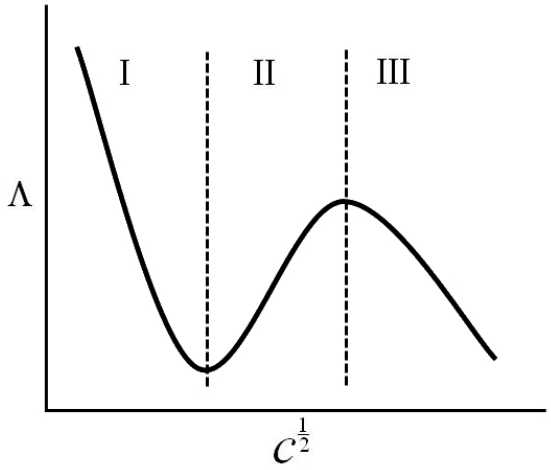

Figure 1.4: Schematic diagram of molar conductivity versus (salt concentration)$^{1/2}$ for liquid electrolytes.

1.4 Ion and Mass Transport

Ionic transport is the conduction of charged ion species in solid or liquid electrolytes. Fundamental understanding of the ion transport mechanism provides insights into complex system dynamics. Ionic transport can be characterized using several key factors: conductivity, molar conductivity, mobility, and ionic association. The ionic

conductivity (σ) of a homogeneous electrolyte can be expressed by the relation

$$\sigma = \sum_i c_i q_i \mu_i. \tag{1.1}$$

Here, the summation runs over all charged species in the system. c_i is the concentration of charge carriers of type i that have charge q_i and ionic mobility μ_i [11]. The unit of the conductivity is Siemens per cm (S cm^{-1}) where S=Ohm^{-1} The molar conductivity (Λ) at a particular concentration (c) is

$$\Lambda = \frac{\sigma}{c}. \tag{1.2}$$

The molar conductivity unit is S cm^2 mol^{-1}.

Ionic transport of liquid electrolytes is conventionally described with viscosity-related models that often predict results that do not agree with experimental data [12, 13, 22, 23]. Consider an ion or particle moving in a viscous solution. According to the Stokes law , the ion experiences a frictional or a drag force that opposes its motion. This drag force (F) is given by $F=6\pi r\eta v$. Here, r is the radius of the moving ion, η is the solvent viscosity, and v is the velocity of ion. From this point of view, ionic conductivity is given by the relation:

$$\Lambda = \frac{q}{6\pi\eta r}, \tag{1.3}$$

where q is the charge on an ion. However, hydrodynamic models do not provide an explanation for the transport at the microscopic level.

The simple Arrhenius equation shown in Eq. 1.4 describes the temperature dependence of ionic conductivity below the glass transition temperature, T_g, for

PEs [24].

$$\sigma = \sigma_0 \mathrm{e}^{-\frac{E_a}{RT}} \tag{1.4}$$

Here, σ denotes the ionic conductivity, σ_0 is the temperature independent prefactor, T is the temperature, and E_a is the activation energy. It has been found that liquid electrolytes and PEs above T_g often show non-Arrhenius temperature-dependent conductivity, commonly described using the Vogel-Tammann-Fulcher (VTF) or the Williams-Landel-Ferry (WLF) empirical equations [25–28]. Because these are all empirical relations, the resulting fitting parameters do not have any physical significance and do not provide information about the underlying mechanism of ion transport. The WLF equation is

$$\log \frac{\sigma(T)}{\sigma(T_s)} = \frac{C_1(T - T_s)}{C_2 + (T - T_s)} \tag{1.5}$$

where $\sigma(T)$ is the temperature-dependent conductivity, $\sigma(T_s)$ is the conductivity at reference temperature(T_s), and C_1 and C_2 are constants that are obtained from experimental data along with T_s. The VTF empirical equation is used to describe the properties of supercooled liquids and to study the temperature dependence of solid and liquid electrolytes.

$$\sigma = \sigma_0 T^{-1/2} Exp\Big[- \frac{B}{R(T - T_0)}\Big] \tag{1.6}$$

Here, $\sigma(T)$ is the temperature dependent conductivity, and σ_0, B, and T_0 are constants.

Similar to ion transport, mass transport of solid and liquid electrolytes have been studied. The mass transport is directly related to diffusion phenomena. Diffusion

describes the transport of materials driven by a gradient of concentration. In a pure liquid system where there is no concentration gradient, individual molecules (or ions) exhibit a random translational motion, which is known as self-diffusion. According to Abu et al., self-diffusion is a measure of the translational mobility of individual particles driven by an internal kinetic energy [29]. Self-diffusion coefficients are measured by the pulsed field gradient NMR technique. Temperature-dependent self-diffusion coefficients also fitted with the VTF and the WLF equations [30]. Further, diffusion coefficients can be expressed using hydrodynamic expressions.

$$D = \frac{k_B T}{6\pi\eta r}, \tag{1.7}$$

where k_B is the Boltzmann constant.

Recently, a new approach has been proposed to describe charge and mass transport in pure liquids and liquid electrolytes [31–34]. The temperature-dependent conductivity and diffusion coefficients are formally written as Arrhenius-like expressions; however, in contrast to Eq. 1.4, there exists a temperature dependence in the exponential prefactor that is due to the temperature dependence of the solvent/solution static dielectric constant (ε_s). Therefore, the ionic conductivity is written as:

$$\sigma(T, \varepsilon_s) = \sigma_0(\varepsilon_s(T))\mathrm{e}^{-\frac{E_a}{RT}}. \tag{1.8}$$

This dielectric constant dependence in the prefactor can be removed by using a scaling procedure. The theory of this new approach will be discussed in chapter 5 and 6. This study allows us to examine fundamental properties of liquid systems.

1.5 Ionic Association

When a salt is added to a pure solvent, it dissociates into positive and negative ions. Those ions can interact with solvent molecules or other ions in the solution. As a result, we can experimentally observe ion-ion interactions, as well as ion-solvent interactions. These ion-ion interactions are referred to as ionic association. In a complex system, such as a polymer-salt or an organic solvent-salt compound, ionic association gives rise to different ionic species. As a consequence, "free" ions, contact-ion pairs, triple ions, and higher ion aggregates can be observed in electrolyte solutions. "Free" ions are either positive or negative ions (M^+ or X^-) which are well-separated in the sample. A single positive ion and a negative ion, which are separated by solvent molecules, are referred to a solvent-separated ion pair. There is no net charge for such an ion-pair. The ionic species formed by the direct, coordinative interaction of cations and anions is called a contact ion-pair. Triple ions ($[M_2X]^+$,$[MX_2]^-$) and larger clusters, which carry charges described as higher ion aggregates are also examples of contact ion species [11]. If a system has a high salt concentration and a low dielectric constant medium, there is a greater probability of forming contact ion pairs and more highly associated species. The formation of ion aggregates increases with the temperature. "Free" ions and solvent separated ion pairs are not spectroscopically distinguishable. Therefore, when we present spectroscopic data, both ion species are described as free or spectroscopically "free" ions.

Fig. 1.5 shows the SO_3 stretching mode of the triflate ion in 2-pentanone. Here,

three overlapped bands are attributed to different ionic species. Bands at 1032, 1042 and 1052 cm^{-1} are assigned to "free" ($CF_3SO_3^-$), ion pair ($Li^+CF_3SO_3^-$) and higher aggregates $(Li_2Tf)^+$, respectively. These band intensities and frequencies are highly dependent on the nature of interaction between cations and anions. These ionically associated species play a major role in ion transport for both polymer and liquid electrolytes. Therefore, my research is focused primarily on ionic association in these electrolytes. Vibrational spectroscopy is a powerful tool to probe ionic association of both polymer and liquid electrolytes [35–37]. Ionic association depends on the sample temperature, the concentration, and the dielectric constant of the solvent.

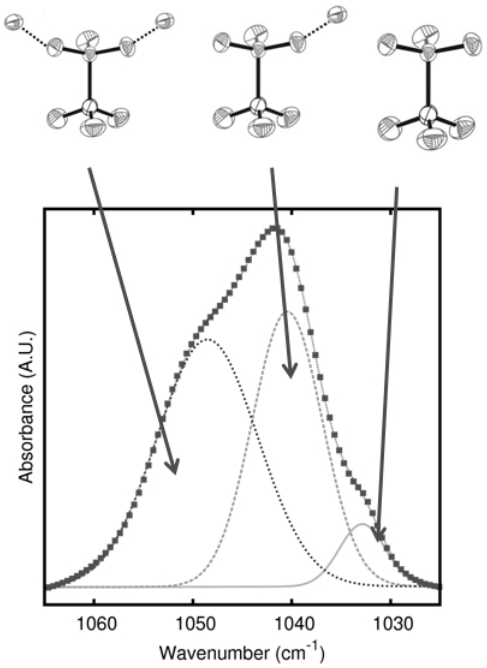

Figure 1.5: Ionic association of the $\nu_s(SO_3)$ mode for a 0.3 m LiTf:2-heptanone solution.(squares = experimental data, solid and dotted lines = fit from deconvolution analysis.)

1.6 Why Study Model Compounds?

Understanding solid polymer electrolyte systems is not easy because they have complex structures. Because they have a large number of repeat monomer units and high molecular weights, polymers have many simultaneous interactions with salt ions. Therefore, local structures and the associated ion transport mechanisms are difficult to study. A model compound represents a part of large polymer molecules. Simply, they are small molecules, which have a structure identical to a polymer segment. Model compounds provide essential insight into the structure and chemical environment of polymer complexes. Previously, researchers have studied model compounds, successfully explaining several polymeric systems. For an example, glycol dimethyl ethers (glymes) have been used as model compounds for PEO and other polymer systems with ether oxygen monomers [38]. Among these studies, a number of glyme-salt crystalline structures were reported. Obtaining a crystal structure from a model compound is the best way to understand the local structure and the chemical interaction in polymer systems. Further, model compounds were found for branched and linear polyethylenimene (PEI) based electrolytes. Most of these compounds were primary or secondary amines: DPA (dipropylamine), hexylamine, NN-DMEDA (N,N dimethylethylenediamine), NN'-DMEDA (N,N' dimethylethylenediamine), TMEDA (tetramethylethylenediamine), and PMDETA (N,N,N',N",N"-pentamethyldiethylenetriamine) [39–42]. These compounds have ability to conduct protons (H^+) and are known as proton conductors. Different types of polymer electrolytes have been studied to date: PEO/ H_3PO_4 and LPEI

or BPEI/ H_3PO_4 or H_2SO_4 [43–45]. We examined several model compounds for different polymer systems. First, we reported crystal structures for some amine-salt systems [46]. Second, we studied crystal structures for amine-phosphoric acid systems, which are used as model compounds for LPEI or BPEI/ H_3PO_4 systems. Fig. 1.6 shows the chemical structural formulae of PEI and NN'-DMEDA. Further, acetates and ketone-salt systems were studied to gain a better understanding of local structures in poly methylmethacrylate (PMMA)-salt systems.

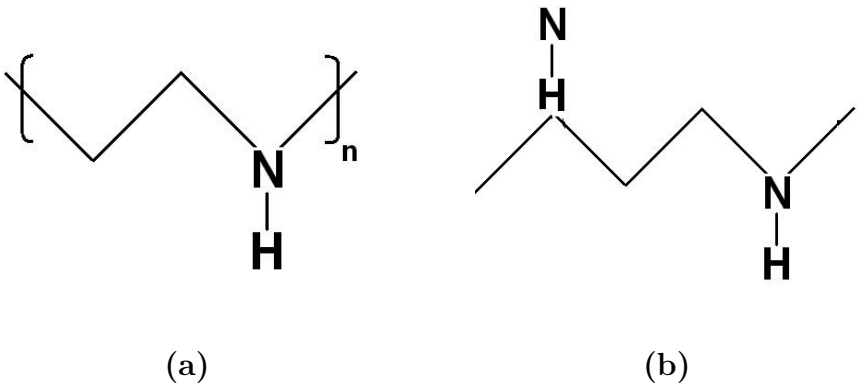

Figure 1.6: Chemical formulae (a) Linear poly(ethylenimine) (b) N, N' dimethylethylenediamine (DMEDA)

1.7 Experimental Methods

1.7.1 Fourier Transform Infrared Spectroscopy (FTIR)

Fourier Transform Infrared Spectroscopy(FTIR) is used to study the interaction of matter with infrared radiation by measuring the absorption of the radiation. When a molecule absorbs radiation that excites a vibrational mode, the process is visible as an absorption line in the spectrum. The absorbance (A) of IR spectrum is given by

$$A = log_{10}(\frac{1}{T}) \tag{1.9}$$

where T is the transmittance. Generally, an IR spectrum represents either absorption or transmission by the functional groups in molecules. Also, because the intensity of an IR absorption band is directly proportional to the amount of material present in a sample, one can estimate the relative concentration of molecular species. Therefore, FTIR is a powerful tool that can be utilized in both qualitative and quantitative analysis.

The FTIR spectrometer consists of an interferometer, fixed and moving mirrors, a detector, and a computer. The interferometer has a beamsplitter, which divides the incoming beam into two optical beams. One beam reflects off the fixed mirror and the other beam reflects from the moving mirror. The beams are re-combined at the beamsplitter, creating an interference signal, the interferogram. This signal contains information about frequencies encoded in it. As the interferogram signal passes through the sample, some frequencies are absorbed by molecules. The position of the moving mirror is a function of time and hence the output energy of

the signal varies with time as well. This signal is then Fourier transformed to the frequency domain to form the infrared spectrum.

Generally, IR radiation is divided into three sub regions:near-infrared from 770 nm to 2.5 μm (12900 to 4000 cm^{-1}), the mid-infrared from 2.5 μm to 50 μm (4000 to 200 cm^{-1}), and the far-infrared from 50 μm to 1000 μm (200 to 10 cm^{-1}). All of the spectral data reported here were measured in mid-IR region and therefore probe vibrational modes of polyatomic species. An interesting property of these vibrational modes is that only some are IR active; not all modes are visible in the IR spectra. A vibration that does not involve a change in the dipole moment of the molecule will not be IR active.

1.7.2 Raman Spectroscopy

Raman spectroscopy is a powerful tool for studying vibrational modes and therefore molecular interactions in solid and liquid samples. This technique is based on the inelastic scattering of a monochromatic excitation source. An inelastic collision between incident photons and the molecules will result in a shift in the frequency of the scattered beam, which is known as Raman scattering. Incident electromagnetic waves excite vibrational modes in the sample which depends on the polarizability of these molecules. The molecular structure and the nature of bonds define the polarizability. The most important aspect of Raman scattering is that only vibrational modes that change the polarizability of the molecule are Raman active. Vibrational modes are excited by absorbing the energy of photons, giving rise to Stokes lines in the spectra. These lines always have a frequency lower than the

incident radiation. The anti-Stokes lines are formed due to collisions of vibrationally excited molecules and photons. In this case, photons gain energy resulting in higher frequency spectral lines. Energy differences between the incoming and outgoing photons give information about molecular vibrational modes. In a molecule with an inversion center of symmetry, only totally symmetric vibrations are Raman active as anti-asymmetric vibrations do not cause a polarizability change. On the other hand, any mode can be Raman active or inactive for a molecule without a center of symmetry.

A Bruker Equinox 55 FRA 106/S Raman spectrometer was used to collect Raman spectra. A coherent Nd: YAG laser was used for excitation at a power level of 300 mW at 1064 nm. Thin NMR tubes and capillary tubes were used to pack liquid and solid samples, respectively. All Raman spectra were taken at the spectral resolution 2 cm^{-1} and 1000 scans for 50-3500 cm^{-1} range with a CCD detector.

1.7.3 Nuclear Magnetic Resonance Spectroscopy (NMR)

Nuclear Magnetic Resonance spectroscopy(NMR) is a unique tool to probe the physical and chemical properties of the atoms and molecules. NMR exploits the fact that spin states of nuclei split into separate energy levels in the presence of a strong magnetic field. These states are excited with a radio frequency pulse and the emitted radio signal when these nuclei are deexcited is measured and called the NMR spectra. The self-diffusion, which is the translational motion of molecules, can be measured by the pulsed field gradient NMR method. This technique uses a magnetic pulse with a spatial gradient which changes the amount of shift in

energy levels depending on the position. Therefore, emitted radiation serves as an indicator of atomic positions. As described in the Fig. 1.7, a gradient pulse is applied after every radio frequency (RF) signal which should cancel the effect of the second field if atoms do not have any translational motion [47]. However, diffusion of atoms gives rise to a measurable shift in the resulting signal.

Pulsed field gradient (PFG) measurements were performed using a Varian VNMRS 400 MHz NMR spectrometer that was operated with an Auto-X-Dual broad band 5 mm probe tuned to 399.870 MHz for protons. Temperature was controlled using an FTS XR401 air-jet regulator. The standard Stejskal-Tanner pulsed gradient sequence (See Fig. 1.7) was performed at each temperature by arraying the gradient field strength from 6 to 62 G/cm [47–50]. The integrated intensity of each attenuated signal was calculated. The attenuated signal intensity is given by

$$S = S_0 exp[-\gamma^2 g^2 D\delta^2(\Delta - \frac{\delta}{3})]. \tag{1.10}$$

Here γ is the gyromagnetic ratio of the observed nucleus, g is the pulsed-gradient strength, δ is the duration of the gradient pulses, and Δ is the separation between gradients pulses. The self-diffusion coefficient was calculated from the slope of the plot Ln(intensity) versus square of the gradient strength. The average self-diffusion coefficients of ions and their associated species are examined as they are indistinguishable.

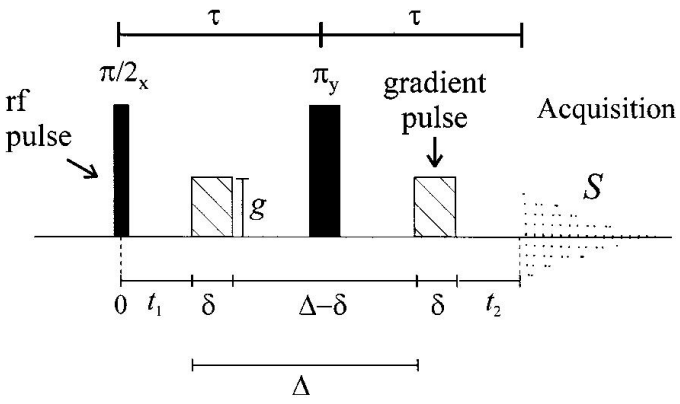

Figure 1.7: The Stejskal-Tanner pulsed field gradient NMR sequence [47]

1.7.4 Impedance Spectroscopy

An impedance analyzer was used to probe the change of capacitance and conductance of samples with temperature. For the conductivity and dielectric constant measurements, a liquid sample was contained in a liquid cell (Agilent 16452A with 2 mm spacer), which was immersed in an oil bath [51]. All measurements were carried out over a temperature range from 0 to 85°C using a Huber ministat 125 with an accuracy ±0.1°C. The capacitance and conductance were measured at each temperature with an impedance analyzer (HP 4192A) scanning the frequency range from 1 kHz to 13 MHz. The measured conductance, in conjunction with the known cell geometry, was used to determine the solution conductivity at each temperature. Conductivity (σ) can be calculated using the measured conductance (G) of the electrolyte as follows.

$$\sigma = \frac{L \times G}{A} \tag{1.11}$$

Here L is the electrode gap and A is the electrode area. The solution and pure solvent static dielectric constants were calculated using the relation $\varepsilon_s = \alpha\, C/C_0$,

where C is the sample capacitance and C_0 is the atmospheric capacitance. The parameter α, which is close to unity, accounts for stray capacitance [51]. A parallel plate capacitor is formed when two conducting plates are separated by a non-conducting media called the dielectric. The value of the capacitance depends on the size of the plates, the distance between the plates, and the properties of the dielectric.

1.8 Research Overview

This thesis consists of six interrelated individual projects. The aim of this series of projects is to understand the fundamental properties of liquid and polymer electrolytes. Properties, such as conductivity, molar conductivity, diffusion coefficient, and ionic association provide deep insight into ion and mass transport mechanisms at the molecular level. Particularly, we are focusing on quantitative studies using different data analysis methods. Further, conductivity data are correlated with ionic association as chemical interactions play a key role in ion conduction. With this objective, temperature-dependent ionic association studies were carried out for both liquid and polymer electrolytes using vibrational spectroscopy. However, ionic association studies are not enough to understand the bond network in complex systems like polymers. Therefore, crystal structures of some model compounds were examined and those five different crystal structures are reported. In sum, all projects are focused on the fundamental energy research which is useful for lithium rechargeable battery and fuel cell technology.

Chapter 1 provides a brief description of battery and fuel cell basics, polymer and liquid electrolytes, ion and mass transport, ionic association, and model compounds. Also it provides a basic description of experimental techniques used in data collection. Chapter 2 examines the molar absorptivities of three vibrational modes of LiTf:2-pentanone solution using the Beer-Lambert law. Quantitative analysis of data is fundamentally based on the Beer-Lambert law. It is a valid method to determine concentrations of sample constituents if the path length and molar absorptivity of various vibrational bands are known. These parameters are necessary to quantitatively compare different samples and extract reliable concentrations from absorption data. We chose LiTf:2-pentanone solution for the experiment for several reasons. Pentanone is a simple ketone and LiTf has a high solubility in this solvent. Also, LiTf:2-pentanone solution does not show complex ion-solvent interactions. Accordingly, experiments were carried out for a range of concentrations of LiTf:2-pentanone at room temperature using FTIR spectroscopy. From this study, the validity of the Beer-Lambert law for liquid electrolytes was verified and used to evaluate molar absorption coefficients. In addition, ion-ion and ion-solvent interactions of the systems were studied. This chapter mainly focuses on three vibrational modes: the SO_3 symmetric stretching mode and SO_3 and CF_3 symmetric bending modes. Our results indicate that molar absorptivity of these modes does not depend on ionic association of cation even though the relative concentration of ionically associated species changes significantly.

Chapter 3 discusses the crystalline phase of ketone-salt systems. As a salt-ketone crystalline phase has not been studied before, we focused on growing crystal

structures using different ketones and salts. Here we report two crystal structures of the LiTf:2-pentanone and NaTf:2 hexanone systems. The LiTf:2-pentanone crystal structure provides strong evidence for ion-solvent interactions reported in chapter 2. Several absorption bands are analyzed and the bond coordination of the carbonyl group and the vibrational modes of triflate anion are explained using vibrational spectroscopy data.

Chapter 4 focuses on the polyethylene oxide LiTf system. The main objective was to study the temperature and concentration dependence of this system quantitatively. The complexity steming from a number of simultaneous interactions in polymer systems creates difficulties when carrying out a quantitative study. Furneaux *et al.* reported the validity of extended Beer-Lambert law for the PEO:LiTf system using temperature-dependent data [52]. This study was extended to (1) evaluate the amount of materials in different polymer phases (such as crystalline, amorphous phases) and (2) study phase changes and polymer configurations in the PEO. During this study, the AsF_6^- band located at 700 cm^{-1} was used as a standard marker. As the noise in the FTIR spectrum was a major problem in data analysis, smoothing techniques were used. After the proper baseline correction, the relative intensity of AsF_6^- band remained constant as expected. When the same procedure is applied to the polymer region, the area was observed to change across the melting point of PEO. This was explained as a result of the phase change of the PEO. However, a similar behavior observed in LiTf vibrational modes was unexpected and could not be explained from this work.

Both Chapter 5 and 6 discuss the temperature-dependent mass and charge

transport in various electrolyte systems. The ion transport process is conventionally explained with viscosity-related models. The temperature dependent ionic conductivity and self-diffusion coefficients of polymer electrolytes and organic liquid electrolytes above glass transition temperature do not exhibit simple Arrhenius behavior. Generally, empirical equations are used to describe this data and the fitting parameters do not provide any physical insight into the transport process. Recently, mass and charge transport of liquid electrolytes has been viewed from an entirely different perspective by postulating that the conductivity and diffusion coefficients assuming an Arrhenius-like expression with static dielectric constant dependence in the exponential prefactor. Here the prefactor is temperature dependent due to the inherent temperature dependence of the dielectric constant. The dielectric constant dependence can be canceled by using a scaling procedure, and the end result is the compensated Arrhenius equation, CAE. The CAE implies that ion transport is governed by a single activated process. The activation energies can be calculated from either the slope or intercept of CAE. In chapter 5, 0.0055 M TbaTf-acetate, ketone solutions, and pure solvents were studied. The TbaTf salt does not show a significant ionic association with either solvent because the anion is a large bulky butyl group. The n-acetates provide an interesting analogy to 2-ketones since they are structurally very similar, with each having a carbonyl group(C=O). Conductivities and static dielectric constants for 0.0055 M TbaTf in acetates (butyl acetate, pentyl acetate, hexyl acetate, octyl acetate, decyl acetate) and ketones (2-pentanone, 2-hexanone, 2-heptanone, 2-octanone, 2-nonanone, and 2-decanone) have been collected over the temperature range 0 to 80°C and 5 to

80°C respectively. All measurements were performed using impedance spectroscopy. Diffusion measurements were carried out for both pure solvents using the pulsed field gradient NMR spin-echo technique. Self-diffusion coefficients and static dielectric constants of pure acetates were obtained over the same temperature range. Both temperature-dependent diffusion coefficients and ionic conductivities of these systems can be accurately described by the compensated Arrhenius formalism. Activation energies were calculated from compensated Arrhenius plots for both conductivity and diffusion data. Activation energies are higher for the ionic conductivity of 0.0055 M TbaTf-acetates compared to diffusion data of pure acetates. The plot of exponential prefactor versus dielectric constant yields a single master curve for conductivity and a similar master curve for diffusion data.

Chapter 6 examines the ionic conductivities and dielectric constants of LiTf dissolved in a series of acetates and ketones. LiTf salt shows significant ionic association with acetates and ketones from 5 to 85°C. The average activation energy of 0.80 mol kg^{-1} LiTf-acetate solutions is lower than that of 0.30 mol kg^{-1} LiTf-acetate solutions. Ketone solutions similarly exhibit higher conductivities than those of acetates at comparable concentrations. Calculated exponential prefactors for all three systems produce a single master curve when plotted against the static dielectric constant. Further, these results verify the validity of fundamental postulates made during this work. FTIR spectroscopy was used to examine the nature of the ion-ion and ion-solvent interactions in LiTf acetate/ketone solutions as a function of temperature and concentration. LiTf-acetate solutions exhibited a higher degree of ionic association than the LiTf-ketone solutions. Here, we observed

two types of ion aggregates. These results in both chapters support the argument that mass and charge transport is a thermally activated process in the acetate and ketone based systems.

Chapter 7 provides some crystallographic and vibrational spectroscopy studies of amine-phosphoric acid systems. We studied N,N'-dimethylethylenediamine, diethylene amine, and piparazine complexed with phosphoric acid. Amine-phosphoric acid systems are used as model compounds for linear and branched poly(ethyleneimine) (PEI)-acid compounds. The purpose of this work was to study the hydrogen-bonding network and investigate the local structures of amine-phosphoric systems.

References

[1] P. G. Bruce, Dalton Trans. **11**, 1365 (2006).

[2] D. MacArthur and P. Powers, in *Battery Conference on Applications and Advances* (Jan 1996), pp. 307–310.

[3] M. Wakihara, Material Science and Engineering **R33**, 109 (2001).

[4] T. B. Reddy and D. Linden, *Linden's Handbook of Batteries* (McGraw-Hill, 2011), 4th ed.

[5] *Hydrogen and Our Energy Future* (2007), Department of Energy: Washington, D. C.

[6] http://biodiesel.environmentalactiongroup.org/hydrogen.html.

[7] F. M. Gray, *Polymer Electrolytes* (Royal Soc. Chem. Cambridge, 1997), 1st ed.

[8] D. E. Fenton, J. M. Parker, and P. V. Wright, Polymer **14**, 589 (1973).

[9] P. Wright, British Polymer Journal **7**(5), 319 (1975).

[10] M. B. Armand, J. M. Chabagno, M. Duclot, ed. P. Vashista, J. N. Mundy, and G. Shenoy, *Fast Ion Transport in Solids* (New York: North Holland, 1979).

[11] P. G. Bruce, *Solid State Electrochemistry* (Cambridge University Press, 1995), 1st ed.

[12] J. R. MacCallum and C. A. Vincent, *Polymer Electrolyte Reviews 1* (Elsevier Applied Science Publishers Ltd., 1987), 1st ed.

[13] J. R. MacCallum and C. A. Vincent, *Polymer Electrolyte Reviews 2* (Elsevier Applied Science Publishers Ltd., 1989), 1st ed.

[14] J. R. Wickham, S. York, N. M. Rocher, and C. V. Rice, J. Phys. Chem. B **110**(10), 4538 (2006).

[15] N. Boden, S. Leng, and I. Ward, Solid State Ionics **45**(3-4), 261 (1991).

[16] A. Johansson, A. Gogoll, and J. Tegenfeldt, Polymer **37**(8), 1387 (1996).

[17] A. M. Christie, S. J. Lilley, E. Staunton, Y. G. Andreev, and P. G. Bruce, Nature **433**, 50 (2005).

[18] C. Svanberg, R. Bergman, L. Borjesson, and P. Jacobsson, Electrochim. Acta **46**(10-11), 1447 (2001).

[19] C. M. Burba and R. Frech, J. Phys. Chem. B **109**(31), 15161 (2005).

[20] R. M. Fuoss and C. Kraus, J. Am. Chem. Soc. **55**(3), 1019 (1933).

[21] E. A. S. Cavell and P. C. Knight, Z. Phys. Chem.(Neue Folge) **57**, 331 (1968).

[22] J. Bockris and A. Reddy, *Modern Electrochemistry*, vol. 1 (Plenum press, 1998), 2nd ed.

[23] I. N. Levine, *Physical Chemistry* (McGraw-Hill:New York, 2009), sixth ed.

[24] S. Arrhenius, Z. Phys. Chem. **4**, 226 (1889).

[25] M. L. Williams, R. F. Landel, and J. Ferry, J. Am. Chem. Soc. **77**, 3701 (1955).

[26] H. Vogel, Physik **22**, 645 (1921).

[27] G. S. Fulcher, J. Am. Ceram. Soc. **8**, 339 (1925).

[28] G. Tammann and W. Hesse, Z. Anorg. Allg. Chem. **156**, 245 (1926).

[29] M. A. Bin, H. Susan, A. Noda, and M. Watanabe, *Diffusion in Ionic Liquids and Correlation with Ionic Transport Behavior, in Electrochemical Aspects of Ionic Liquids* (John Wiley and Sons. Inc., 2011), 2nd ed.

[30] C. A. Vincent, Electrochim. Acta **40**(13-14), 2035 (1995).

[31] M. Petrowsky and R. Frech, J. Phys. Chem. B **114**(26), 8600 (2010).

[32] M. Petrowsky and R. Frech, J. Phys. Chem. B **113**(17), 5996 (2009).

[33] M. Petrowsky and R. Frech, Electrochim. Acta **55**(17), 1285 (2010).

[34] M. Petrowsky and R. Frech, J. Phys. Chem. B **113**(17), 16118 (2009).

[35] W. Huang, R. Frech, P. Johansson, and J. Lindgren, Electrochim. Acta **40**(13), 2147 (1995).

[36] R. Frech and W. Huang, Solid State Ionics **72**(2), 103 (1994).

[37] G. Petersen, P. Jacobsson, and L. Torell, Electrochim. Acta **37**(9), 1495 (1992).

[38] V. A. Seneviratne, R. Frech, J. E. Furneaux, and M. Khan, J. Phys. Chem. B **108**(24), 8124 (2004).

[39] S. S. York, S. E. Boesch, R. A. Wheeler, and R. Frech, Macromolecules **36**(19), 7348 (2003).

[40] R. A. Sanders, R. Frech, and M. A. Khan, J. Phys. Chem. B **108**(34), 12729 (2004).

[41] N. M. Rocher, R. Frech, and D. R.Powell, J. Phys. Chem. B **110**(31), 15117 (2006).

[42] R. A. Sanders, R. Frech, and M. A. Khan, J. Phys. Chem. B **108**(7), 2186 (2004).

[43] R. Tanaka, H. Yamamoto, A. Shono, K. Kubo, and M. Sakurai, Electrochim. Acta **40**(13-14), 2421 (2000).

[44] D. Glatzhofer, M. Erickson, R. Frech, F. Yepez, and J. Furneaux, Solid state ionics **176**, 2861 (2005).

[45] R. Tanaka, H. Yamamoto, A. Shono, K. Kubo, and M. Sakurai, Electrochim. Acta **45**(8), 1385 (2000).

[46] G. A. Giffin, S. Boesch, D. N. Bopege, D. R. Powell, R. A. Wheeler, and R. Frech, J. Phys. Chem. **113**, 15914 (2009).

[47] W. S. Price, Concepts Magn. Reson. **9**, 299 (1997).

[48] E. O. Stejskal and J. Tanner, J. Chem. Phys. **42**(8), 288 (1965).

[49] X. X. Zhu and P. M. Macdonald, Macromolecules **25**(17), 4345 (1992).

[50] W. S. Price, Concepts Magn. Reson. **10**(4), 197 (1998).

[51] *Agilent 16452A Liquid Test Fixture Operation and Service Manual* (2000).

[52] J. E. Furneaux, A. M. McCoy, V. Seneviratne, and R. Frech, in *Proceedings of the 10th Asian Conference on Solid State Ionics Advanced Materials for Emerging Technologies* (World Scientific, 2006), p. 469.

Chapter 2

Quantitative Analysis of Molar Absorptivity for LiTf:2-pentanone Solution Using Beer-Lambert Law

2.1 Introduction

Alkali salts dissolved in aprotic solvents are of interest because they are used in secondary lithium ion batteries. It is particularly important to understand the ionic association in these systems both qualitatively and quantitatively since the degree of association greatly impacts the ionic conductivity. During the last few decades, research groups have studied ionic association in polymer and liquid electrolytes using a variety of spectroscopically sensitive salts [1–6]. These investigations were mainly based on Fourier Transform Infrared (FTIR) and Raman spectroscopy [1, 2, 7, 8]. Due to the complex environments of polymer systems, most studies are qualitative in nature.

Quantitative analysis of FTIR data is fundamentally based on the Beer-Lambert law: the absorbance of a sample is directly proportional to the concentration of the absorbing molecule. Beer-Lambert law is given by

$$A(\lambda) = \epsilon(\lambda)bc \tag{2.1}$$

Here, A is the absorbance of ionic species at a particular wavelength(λ), ϵ is the molar absorptivity of ion species at a particular wavelength in kg mol^{-1} cm^{-1}, b is the path length of the sample in cm, and c is the molal concentration of the

sample in kg mol^{-1}. For a given spectral region, the integrated absorption is the area under the spectral band. It is a measure of the intensity of a spectroscopic transition. In other words, the integrated absorption coefficients are proportional to the oscillator strength. Beer's law is a valid method to determine concentration of sample constituents if the path length and molar absorptivity of the various vibrational bands are known [9]. These parameters are necessary to quantitatively compare different samples and extract reliable concentrations from absorption data.

Ionic association and solvation of LiTf in different aprotic solvents have been studied extensively using vibrational spectroscopy. Several groups have made assignments for IR and Raman active bands of LiTf-acetone systems [1, 3, 8]. They reported quantitative analysis for different spectral bands (symmetric, asymmetric stretching SO_3, and asymmetric stretching CF_3 modes) using deconvolution and band fitting. This study shows the presence of ion paring and higher aggregates in LiTf-acetone solutions [1, 3, 8]. In addition, ionic association and solvation of different alkali salts ($LiClO_4$, $NaClO_4$, $AgClO_4$, NaI) in acetone have been examined in the past years [10, 11]. However systematic quantitative studies are rare for alkali salts in ketone solvents.

The study reported in this chapter quantitatively calculates ionic association using FTIR data for LiTf in 2-pentanone. The triflate ion is spectroscopically sensitive to ionic association [2, 4, 12]. Three spectral bands were studied at different molar concentrations (0.6-1.2 mol kg^{-1}): SO_3 symmetric stretch (ν_s) band, SO_3 and CF_3 symmetric bend (δ_s) bands in the range 600-1100 cm^{-1}. The total intensity (area under the peak, A) of each band was calculated by integration. The

path length (l) was evaluated for each concentration by studying interference fringes. These data were then combined to obtain normalized absorption (A/b) and when plotted against the salt concentration follows a straight line as predicted by the Beer-Lambert law. Molar absorptivities were determined for three spectral bands from the slope of each graph. The experimental uncertainty of molar absorptivity was 1%. Based on these results, the overall molar absorptivity of the spectral band does not depend on ionic association.

2.2 Experimental Methods

The compounds (2-pentanone (99%) and LiTf (99.995%)) were obtained from Aldrich. The samples were prepared in a glove box under a nitrogen atmosphere ($\leq$ 1 ppm H_2O and approximate temperature 25°C). LiTf was dissolved in the appropriate amount of 2-pentanone to make the concentrated solution (0.6-1.2 mol kg^{-1}), and then stirred for 24 hours before use. The sample filled the semi-permanent KBr rectangular liquid cell equipped with 0.025 mm teflon spacer.

Nine spectra were recorded using a Bruker IFS66V FTIR spectrometer under purge air for each salt concentrations at room temperature. All spectra were collected at a spectral resolution 1 cm^{-1}, 400-4000 cm^{-1}, spectral range for 64 scans. Three different spectral bands were investigated between 600-1100 cm^{-1}. The Savitzky-Golay algorithm was applied to smooth the spectra for both solution and neat samples. The neat spectrum of pure 2-pentanone was subtracted from each sample spectrum, prior to integration. The integrated area under the each

spectral band is calculated and equated to the absorption. Spectral band areas were calculated by both direct integration and curve fitting using OriginPro 7.5 software. For the curve fitting process, each band was deconvoluted into multiple gaussian components. The total integrated absorption was the sum of areas of all bands. Both peak integration and curve fitting were performed by defining the best base line for required spectral region. The multiple components originate in different ionic species of the sample. The normalized absorption (A/b) was obtained by dividing total integrated absorption (A) by path length (b) for each concentration. The uncertainty of each data point was calculated based on the standard deviation of nine IR measurements.

A sample single spectrum was collected for the empty demountable KBr liquid cell and is illustrated in Fig. 2.1. The fringing effect in this spectrum is a result of constructive and destructive interferences of the IR light beam from the parallel and smooth surfaces of the optical windows. These interference fringes are used to determine the correct thickness or the path length of the sample liquid cell. The spectrum in Fig. 2.1 was smoothed using a Fast Fourier Transform (FFT) filter in Origin software. The path length of the liquid cell can be obtained using the equation, [13, 14]:

$$b = \frac{10N}{2(\nu_1 - \nu_2)} \tag{2.2}$$

where N is the number of fringes within a given spectral region, b is the path length of the liquid cell in mm and, ν_1, ν_2 are the initial and final wave numbers of extrema in the spectral region in cm^{-1}, respectively. The factor 10 is due to the conversion from centimeters to millimeters. Before collecting the spectra for each

concentration, the path length of the liquid cell was calculated using this procedure.

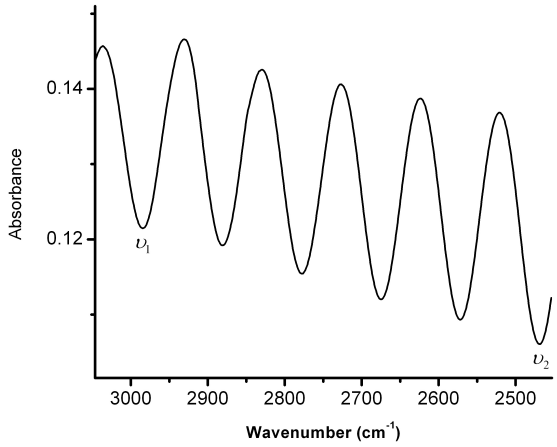

Figure 2.1: "Fringing effect" of the FTIR spectrum of the empty liquid cell with KBr windows.

2.3 Results and Discussion

FTIR spectra were collected for different concentrations of LiTf:2-pentanone solutions. Three triflate bands were observed between 600 and 1100 cm^{-1} as illustrated in Fig. 2.2. These bands are attributed to the symmetric SO_3 stretching, symmetric SO_3 bending, and symmetric CF_3 bending modes. In this figure, the inset presents the expanded CF_3 vibrational mode.

Figure 2.3 shows the symmetric SO_3 stretching band, $\nu(SO_3)$ of lithium triflate in 2-pentanone solution in the concentrations range (0.2-1.2 mol kg^{-1}). The multiple bands were identified in this non-degenerate $\nu(SO_3)$ spectral region (1020-1070 cm^{-1}). These bands are attributed to the distinct ion species in the solution:

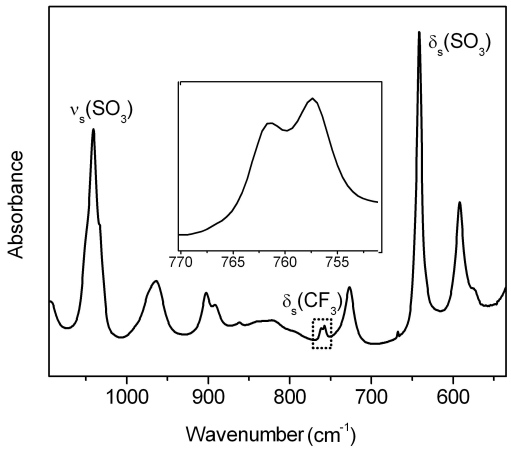

Figure 2.2: Infrared spectrum of LiTf:2-pentanone solution in the range from 600 to 1080 cm^{-1} . Inset shows the expanded region of the CF_3 bending band.

"free" ions, ion pairs and higher ion aggregates. The band at 1032 cm^{-1} is assigned to "free" triflate ions. The band at 1041 cm^{-1} is assigned to contact ion pairs and band at 1050 cm^{-1} represents the higher ion aggregates [4, 12, 15, 16].

In agreement with the literature, three spectral bands were observed in the same frequencies. Due to base line errors discussed in the experimental section, it is hard to define the weight of error bars for low concentrations. Hence we restricted our results to the concentration range (0.6-1.2 mol kg^{-1}) for the symmetric SO_3 stretching mode. The absorptivities of all ionic species ("free" ion, ion pairs and ion aggregates) contribute to the total molar absorptivity of the spectral band. As a result of ionic association, the overall molar absorptivity is given by,

$$\epsilon(\lambda)c = \epsilon_{free}c_{free} + \epsilon_{pair}c_{pair} + \epsilon_{agg}c_{agg}. \tag{2.3}$$

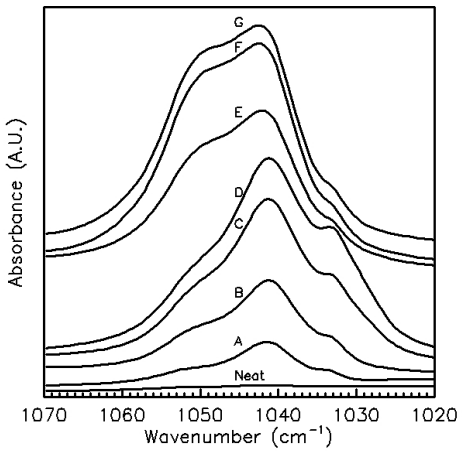

Figure 2.3: Infrared spectrum of LiTf:2-pentanone solution in the range from 1020 to 1070 cm^{-1}. The letters are designated as follows: (a) 0.2 (b) 0.4 (c) 0.6 (d) 0.8 (e) 1.0 (f) 1.2 (g) 1.4. All concentrations in mol kg^{-1}.

Here, c_{free}, c_{pair}, and c_{agg} are the concentrations of each species.

Fig. 2.4 shows the non-degenerate $\delta(CF_3)$ bending mode within the concentration range 0.6-1.2 mol kg^{-1}. Two bands appear for LiTf:2-pentanone solution in the range between 750 to 770 cm^{-1}. The band at 758 cm^{-1} is due to contact ion pairs and 762 cm^{-1} band is attributed to the ion aggregates. There is no band clearly visible for the "free" ions as seen in LiTf-polymer complexes in early studies [17]. Further, the absorbance associated with CF_3 bending band is relatively small and hence it is less likely to be overabsorbed.

Similarly, three bands were observed in the $\delta(SO_3)$ spectral region from 610 to 670 cm^{-1} which are assigned to "free" ions, contact ion pairs and ion aggregates. Absorption intensities of each band, which were calculated from direct integration,

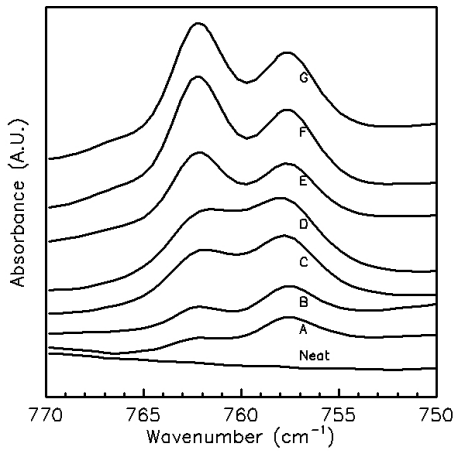

Figure 2.4: Infrared spectrum of LiTf:2-pentanone solution in the range from 750 to 770 cm^{-1}. (a) 0.2 (b) 0.4 (c) 0.6 (d) 0.8 (e) 1.0 (f) 1.2 (g) 1.4. All concentrations in mol kg^{-1}.

were used to produce results described in this chapter.

Figure 2.5 is the plot of normalized absorption versus salt concentration for the symmetric SO_3 stretching, symmetric SO_3 bending, and the symmetric CF_3 bending modes. Data points for each vibrational mode are represented well by straight lines with different slopes. The slope of each line gives the molar absorptivity (or molar extinction coefficient) of the spectral band. The error bars of the graph are uncertainties of the integrated intensities and are used to estimate the uncertainty of molar absorptivity.

The ionic association of the three distinct ionic species of symmetric SO_3 stretch band is illustrated in Fig. 2.6. In this figure, the normalized intensity of higher ion aggregate is gradually increased with salt concentration. However, the overall normalized intensity grows linearly when the salt concentration increases. These

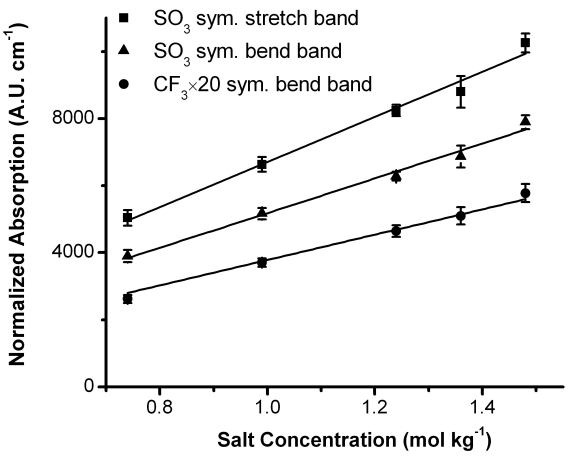

Figure 2.5: Normalized integrated intensity versus molar concentration for symmetric SO_3, symmetric SO_3 bend, symmetric CF_3 bend spectral modes.

results clearly show there is no significant variation in the oscillator strength due to ionic association of the spectral band. Table 2.1 summarizes the estimated molar absorptivities of the symmetric SO_3 stretching, symmetric SO_3 bending and symmetric CF_3 bending bands.

Table 2.1: Molar absoptivities of three vibrational bands in LiTf:2-pentanone solutions.

Spectral and	Molar Absorptivity ($kg\ mol^{-1}\ cm^{-1}$)	standard error ($kg\ mol^{-1}\ cm^{-1}$)
SO_3 symmetric stretch	6708	89
SO_3 symmetric bend	5182	62
CF_3 symmetric bend	189	2

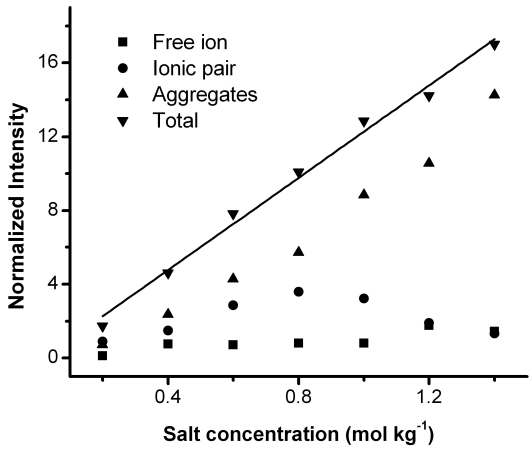

Figure 2.6: Ionic association of the three ionic species of symmetric SO_3 mode in LiTf:2 pentanone solution

2.4 Conclusions

Three different vibrational modes were studied to obtain molar absorptivities for each band using the Beer-Lambert law. According to our results, the normalized absorption plotted as a function of salt concentration follows a straight line as predicted by the Beer-Lambert law even though the relative concentrations of ionically associated species change significantly. Calculated molar absorptivities are within 1 % experimental uncertainty. The integrated absorption coefficients are proportional to the oscillator strength which is a measure of the intensity of a spectroscopic transition. Our results indicate that the oscillator strength of each band does not vary significantly when the absorbing triflate ions are associated with different numbers of Li ions. Strong absorption is observed for both symmetric SO_3 stretching and symmetric SO_3 bending bands. The CF_3 bending band shows

a weak absorption.

This method can be applied to determine accurate sample concentrations using known molar absorptivity for a spectral band of interest under the same experimental conditions. In this case, the integrated absorption of IR band needs to be determined using an integration method. However, errors need to be minimized to achieve best results. Similarly, sample thickness can be calculated using this procedure for a known integrated intensity and sample concentration. Due to the experimental difficulties, Beer's law can not be used to calculate the molar absoptivity for distinct species in the spectral band. In the future, it is interesting to measure the molar absorptivities of other alkali salt such as $LiPF_6$, $LiAsF_6$, and $LiClO_4$ using this method. Further, it is necessary to understand the ionic association and ion transport mechanism of polymer electrolytes quantitatively using these results.

References

[1] J. R. Stevens and P. Jacobsson, Can. J. Chem. **69**, 1980 (1991).

[2] W. Huang, R. Frech, P. Johansson, and J. Lindgren, Electrochim. Acta **40**, 2147 (1995).

[3] J. Alia and H. Edwards, Vib. Spectrosc. **24**, 185 (2000).

[4] W. Huang and R. Frech, Polymer **35**(2), 235 (1994).

[5] J. R. MacCallum and C. A. Vincent, *Polymer Electrolyte Reviews 1* (Elsevier Applied Science Publishers Ltd., 1987), 1st ed.

[6] J. R. MacCallum and C. A. Vincent, *Polymer Electrolyte Reviews 2* (Elsevier Applied Science Publishers Ltd., 1989), 1st ed.

[7] G. Petersen, P. Jacobsson, and L. Torell, Electrochim. Acta **37**, 1495 (1992).

[8] J. M. Alia, Y. D. Mera, H. G. M. Edwards, F. J. Garca, and E. E. Lawson, J. Mol. Struct. **408-409**, 439 (1997).

[9] X. Wang, H. Harris, H. Temkin, S. Gangopadhyay, M. D. Strathman, and M. West, App. Phys. Lett. **78**(20), 3079 (2001).

[10] A. Pullin and J. Pollock, Trans. Faraday Soc **54**, 11 (1958).

[11] H. Yamada, Bull. Chem. Soc. Japan **33**(5), 666 (1960).

[12] R. Frech and W. Huang, J. Sol. Chem. **23**(4), 469 (1994).

[13] J. A. d. H. P.R. Griffiths, *Fourier Transform Infrared Spectroscopy* (John Wiley & Sons Ltd., 1986), 2nd ed.

[14] P. M. B. Stuart, B. George, *Modern Infrared Spectroscopy* (John Wiley & Sons Ltd., 1998).

[15] S. P. Gejji, K. Hermansson, J. Tegenfeldt, and J. Lindgren, J. Phys. Chem. **97**(44), 1140211407 (1993).

[16] A. G. Bishop, D. R. MacFarlane, D. McNaughton, and M. Forsyth, J. Phys. Chem. **100**(6), 2237 (1996).

[17] W. Huang, R. Frech, and R. A. Wheeler, J. Phys. Chem. **98**, 100 (1994).

Chapter 3

Crystal Structures and Vibrational Spectroscopic Analysis of Ketone-Salt Complexes

3.1 Introduction

It is well known that salts can be dissolved in polar, aprotic organic liquids. Alkali metal salts, particularly lithium salts, are of great interest because of their use in electrolytes for lithium ion batteries. In order to optimize electrochemical performance it is important to understand factors that control ionic conductivity such as ion-ion interactions and ion-solvent interactions. Lithium salts dissolved in organic carbonates, e.g., propylene carbonate and ethylene carbonate, are currently utilized in commercial lithium ion batteries [1–3]. In these systems, the lithium ion appears to coordinate with the solvent molecules through the carbonyl oxygen atom. The search for polymer electrolytes as a replacement for organic liquid-based electrolytes has considered polymer hosts with a carbonyl oxygen atom as the coordinating heteroatom, e.g., poly(methyl methacrylate)-PMMA [4, 5].

One of the important factors that directly affects the ionic conductivity is the immediate environment of the mobile cation, specifically the nature of cation-anion and cation-matrix interactions. Vibrational spectroscopy is an important technique to study these interactions in a variety of systems. Several of the vibrational modes of the anion are particularly sensitive to ionic association; consequently triflate-containing salts have been used to study ionic association and solvation in

organic liquid and polymer electrolyte systems. Detailed vibrational assignments for several ionically associated lithium-triflate species have been given by Huang *et al.* [6]. Various salts in acetone were studied in the 1950s and 1960s, with particular attention to molecular complexes formed by addition of salts to acetone [7–13]. Pullin *et al.* reported infrared studies for lithium and silver perchlorate in acetone, noting that two complexes were present based on analysis of the absorption bands [10]. The formations of these complexes were explained by electron donor-acceptor interactions between the cation and the CO group. To study the intermolecular bonding of these complexes, it is necessary to clarify the charge transfer forces involved in these interactions. The authors surmised that the carbonyl stretching frequency is dependent on the relative weights of the ketone resonance structures.

In 1959, Yamada obtained needle-like crystals for the NaI-acetone system. Her studies suggested that the formation of those complexes is due to the coordination of lone pair electrons of oxygen atoms to the metal ion [13]. She argued that there is no evidence for enolization of acetone proposed by N. A. Slovokhotova [11]. Further, Yamada estimated the covalent contribution to the intermolecular bond formation in addition to ion-dipole, dipole-dipole, and London forces [12]. She computed the n-π^* transition energies of the acetone-salt complexes and compared the results with observed data. J. R. Stevens *et al.* examined ionic association of LiTf in acetone and poly (propylene glycol, PPG) [7]. The authors concluded that "free" and triple ions are present in both complexes.

Previous studies of lithium salts complexed with polar organic molecules show that the lithium ion is generally coordinated with one or more oxygen atoms of the

triflate ion and the heteroatom of the solvent. It would be desirable to study the vibrations of a crystalline ketone-lithium salt complex in parallel with a solution of the corresponding ketone-salt complex in order to assign bands in both systems with a high degree of confidence. With this objective in mind, we prepared ketone-salt complexes using LiTf and NaTf salts. We obtained two crystal structures: LiTf:2-pentanone and NaTf:2-hexanone. Crystalline complexes were solved using x-ray crystallography. A comparative vibrational study of the crystalline complex and its solution provides insight into the interaction of the lithium ion with the host ketone and the accompanying cation-anion interactions.

3.2 Experimental Methods

All chemicals were used as received from Aldrich (99% pure). They were stored in a glove box (VAC $\leq$ 1 ppm H_2O) in a dry nitrogen atmosphere. Solutions were prepared by mixing weighed amounts of salt with weighed amounts of 2-ketones and stirring for 24 hours at room temperature(RT) to ensure complete dissociation of the salt. All solution samples were reported as a ketone oxygen to salt (O:Li or Na) molar ratio. Crystals appeared in concentrated solutions after 5-6 weeks in the glove box. A colorless block-shaped LiTf:2-pentanone crystal of dimensions $0.34\times0.28\times0.16$ mm^3 was used for structural analysis. Also, a white block-shaped crystal of dimensions $0.58\times0.36\times0.14$ mm^3 was selected for NaTf:2-hexanone structural analysis.

X-ray crystallographic intensity data for the crystal compounds were collected

at 100(2) K using a diffractometer with a Bruker APEX CCD area detector and graphite-monochromated MoKα radiation ($\lambda = 0.71073$ Å) [14, 15]. The structure was solved by direct methods and refined by full-matrix least-squares methods on F^2 [16–18]. Positions of hydrogen atoms bonded to the carbons were initially determined by geometry and refined by a riding model. Non-hydrogen atoms were refined with anisotropic displacement parameters. Hydrogen atom displacement parameters were set to 1.2 (1.5 for methyl) times the displacement parameters of the bonded atoms. For the LiTf:2-pentanone crystal, the final R1 was found to be 0.0664, based on 1302 observed reflections, [I > 2s(I)], and wR2 was 0.1707, based on 1784 unique reflections. For the NaTf:2-hexanone crystal, the final R1 was found to be 0.1055, based on 5083 observed reflections, [I > 2σ(I)], and wR2 was 0.2979, based on 6883 unique reflections.

Infrared spectra were obtained from neat solvent, liquid, and crystal samples (LiTf:2-pentanone and NaTf:2-hexanone) using a Bruker IFS66V FT-IR spectrometer. IR spectra for liquids were collected using a liquid cell equipped with potassium bromide windows and a 0.025 mm spacer. These samples were run under a dry air purge. IR data of crystal samples were measured using KBr pellets under a vacuum (12 mbar). Data were collected for both classes of samples from 400 to 4000 cm^{-1} at a spectral resolution of 1 cm^{-1}, using a Bruker IFS66V equipped with a KBr beam splitter, and a DTGS detector. A thin sample layer sandwiched between two ZnSe windows was used to observe the IR spectrum of neat ketones. Raman spectra of all samples were recorded using a Bruker Equinox 55 FRA 106/S with a Nd:YAG laser and a CCD detector. Thin NMR tubes and capillary tubes

were used to pack liquid and solid samples, respectively. Data were taken for 2000 scans at a spectral resolution of 2 cm^{-1}.

3.3 Results and Discussion

3.3.1 LiTf:2-pentanone crystal structure

The asymmetric unit of a LiTf:2-pentanone crystal ($C_6H_{10}F_3LiO_4S$) is illustrated in Fig. 3.1. The lithium ions are four-fold coordinated with one carbonyl oxygen atom and three triflate ion oxygen atoms (one oxygen atom from each of three triflate ions).

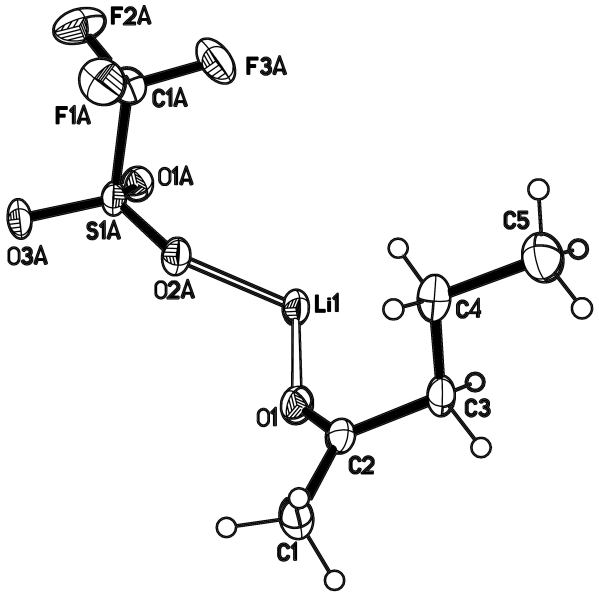

Figure 3.1: Asymmetric unit of LiTf:2-pentanone crystal.

NaTf:2-hexanone crystal structure

The asymmetric unit of NaTf:2-hexanone is illustrated in Fig. 3.2. The Na ion is coordinated with the carbonyl oxygen atom, and it interacts with four triflate ion oxygen atoms. The crystal structure data for both crystals are summarized in Table 3.1.

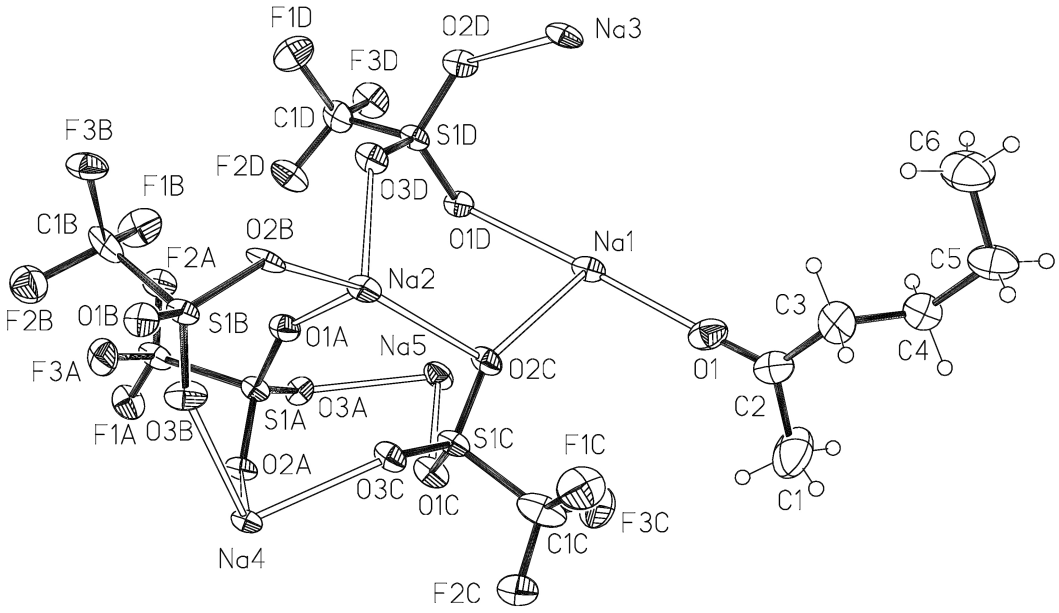

Figure 3.2: Asymmetric unit of NaTf:2-hexanone crystal.

3.4 Vibrational Spectroscopy of LiTf:2-pentanone Crystal Structure

3.4.1 Carbonyl stretching vibrations, ν(CO)

As seen in the packing diagram illustrated in Fig 3.3, each Li ion is coordinated with one carbonyl oxygen atom of 2-pentanone. The effects of this interaction are

Table 3.1: Structural data for crystal structures: LiTf:2-pentanone and NaTf:2-hexanone

Parameters	LiTf:2-pentanone	NaTf:2-hexanone
Crystal system	Monoclinic	Triclinic
Space group	$P2_1/n$	$P\bar{1}$
a	13.145(9)	9.659(8)
b	5.516(4)	11.276(9)
c	14.592(10)	14.031(12)
α	90	73.385(18)
β	99.658(9)	82.841(19)
γ	90	70.095(17)
Volume(A^3)	1043.0(13)	1376(2)
Z,Z$'$	4,1	2,1
Density(Mg/m^3)	1.542	1.902
R1	0.06	0.1055
crystal size(mm^3)	0.34×0.28× 0.16	0.58×0.36× 0.14

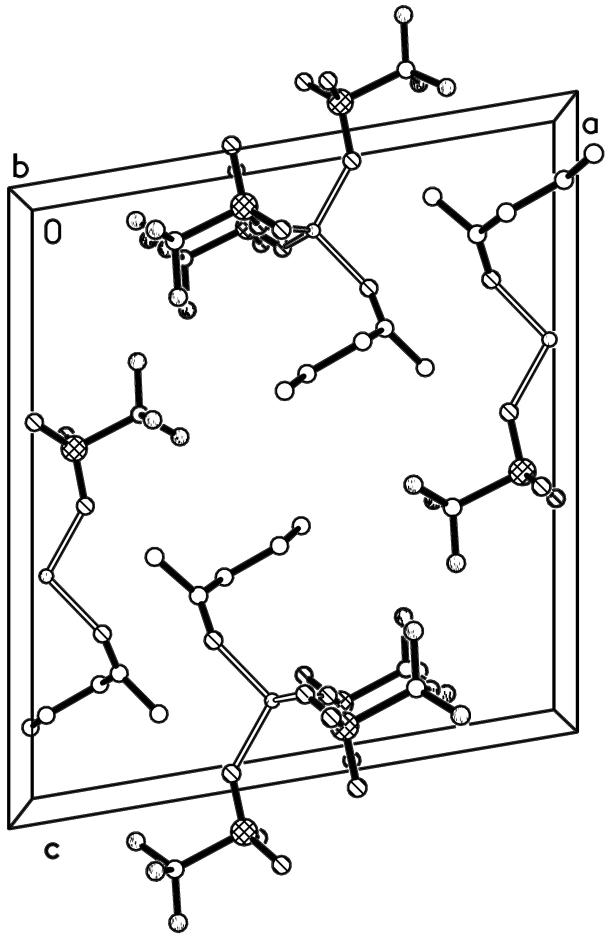

Figure 3.3: Packing diagram of the LiTf:2-pentanone crystal projected down the crystallgraphic b axis.

readily observed in the FTIR and Raman spectra of the LiTf:2-pentanone system. The CO stretching mode, (CO), of pure 2-pentanone occurs at about 1718 cm^{-1} in the IR transmission spectrum. There is a barely discernible shift to 1717 cm^{-1} in a solution of O:Li = 10:1 molar composition, as shown in Fig. 3.4. However, there is a broad, lower feature under the band envelope, giving a very asymmetric appearance to the band.

The CO frequencies in the Raman spectra of the pure ketone and the solution

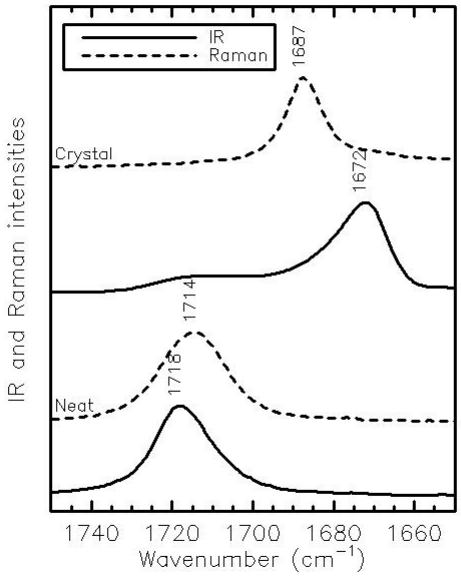

Figure 3.4: Infrared and Raman spectra of CO stretching region (from 1650 to 1750 cm^{-1}) for LiTf:2-pentanone crystal and pure 2-pentanone

are similar, however the Raman intensity is very weak in the pure liquid and increases markedly in the 10:1 solution. In the IR spectrum of the crystalline compound, there is a well-defined, asymmetric band at 1672 cm^{-1}, with a very weak, broad feature in the vicinity of 1717 cm^{-1}. This large shift to lower frequency compared with the pure ketone is not surprising, given that the Li-O distance (carbonyl oxygen) is 1.954(9) Å. There is only a single band at 1687 cm^{-1} in the Raman spectrum. This 15 cm^{-1} difference between the CO band frequencies in the IR and Raman spectra originates in the structure of the unit cell. The four asymmetric units in the monoclinic unit cell form two dimers with two asymmetric units in each dimer related by a crystallographic center of symmetry. Therefore the CO vibrations of the cell can be written in terms of the $C_{2h}{}^5$ symmetry of the crystal as:

$$\Gamma(\nu(\mathrm{CO})) = \mathrm{A}_g + \mathrm{B}_g + \mathrm{A}_u + \mathrm{B}_u$$

Here the A_g and B_g components are only Raman active, while the A_u and B_u components are only IR active. The two bands observed in the IR are the $\mathrm{A}_u + \mathrm{B}_u$ modes, while the single Raman active band is probably the A_g mode; B_g modes often have a small polarizability derivative and are weakly observed, if at all. Although there appear to be no reports of lithium salts in 2-pentanone or other simple linear ketones, there are a number of studies of acetone-salt systems [7, 10, 12, 13, 19–22]. In each of those systems, the pure acetone band, ν(CO), is divided into two components at high salt concentrations. According to Pullin *et al.* (1958), The band at high frequency is close to, but slightly lower than the pure acetone band [10]. Further, they determined that the lower frequency band intensity increases with the high salt concentration while the higher frequency band decreases by studying infrared spectra. Table 3.2 presents a comparison of C=O stretching frequency data reported by several groups for various salts dissolved in acetone.

The 46 cm^{-1} shift (pure 2-pentanone $\rightarrow$ crystalline complex) that is observed in this study is larger than any shift reported in Table 3.2, although that is not surprising since it is expected that the shift upon formation of a crystalline complex would be larger compared to a salt solution.

Table 3.2: Comparison of CO stretching frequencies for pure acetone and acetone-salt systems [10, 12, 13].

Salt type	Mole fraction	ν(CO)-pure acetone	ν(CO)-acetone complex	References
$AgClO_4$	0.08-0.29 mole fraction	1715	1685	[10]
$LiClO_4$	of ClO_4	1715	-	
NaI	I:acetone = 1:5	1717	1709	[12]
$ZnBr_2$	Br:acetone = 1:5	1717	1697	
$NaClO_4$	Na:acetone = 1:4	1717	1710	[13]
$LiClO_4$	Li:acetone = 1:4	1717	1702	

3.4.2 Lithium ion-pentanone interactions

Figure 3.5(a) shows IR spectra in the range 750-790 cm^{-1}, which contains the CF_3 symmetric deformation mode, $\delta_s(CF_3)$. In the 10:1 solution, there are two components at 758 and 762 cm^{-1}. These frequencies have been assigned to Li^+-Tf^- contact ion pairs and the triple ion $(Li_2Tf)^+$, respectively [6, 23–26]. The Raman spectrum of the solution also shows two bands in this region that are coincident in frequency with the IR bands. There is no absorption of the neat pentanone (data not shown). The IR spectrum of the crystal has two bands at 776 and 771 cm^{-1}, whereas the Raman spectrum in this region has a single band at 771 cm^{-1}. The relatively high frequencies of the $\delta_s(CF_3)$ bands in the crystal are consistent with a triflate ion in which each oxygen atom is coordinated by a lithium ion, i.e. the

triflate ion vibrates as if it were an $[Li_3Tf]^{2+}$ entity.

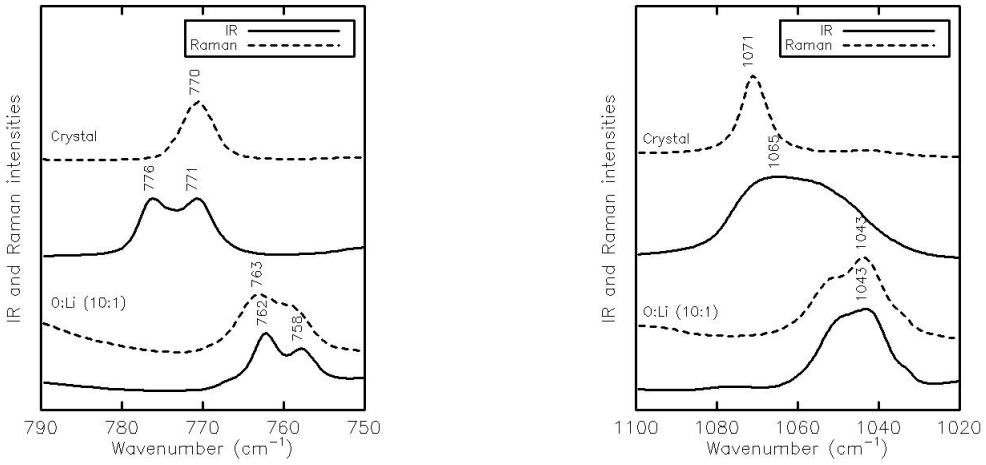

(a) **(b)**

Figure 3.5: (a) Infrared and Raman spectra of $\delta_s(CF_3)$ deformation region (from 750 to 790 cm^{-1}) for 2-pentanone:LiTf crystal and 10:1 solution.(b) Infrared and Raman spectra of $\nu_s(SO_3)$ stretching region (from 1020 to 1100 cm^{-1}) for LiTf:2-pentanone crystal and 10:1 solution.

The two bands in the IR spectrum of the crystal arise from factor group splitting, and the vibrations of $\delta_s(CF_3)$ in the unit cell are predicted to have the same pattern as the CO stretching normal modes, i.e. $\Gamma(\delta_s(CF_3)) = A_g + B_g + A_u + B_u$
It is interesting to note that the Raman active $\delta_s(CF_3)$ mode at 771 cm^{-1} is coincident with one of the IR active modes.

The SO_3 symmetric stretching modes, $\nu_s(SO_3)$, are illustrated in Fig. 3.5(b). The spectrum of the solution appears to consist of three overlapping bands, 1032, 1040, and 1048 cm^{-1}, assigned to "free" ions, contact ion pairs, and the triple ion

$[Li_2Tf]^+$, respectively [7, 24, 25, 27]. The corresponding Raman spectrum also has three overlapping bands at 1033, 1042, and 1051 cm^{-1}. The IR spectrum of the crystal consists of a very broad feature from about 1045 to 1075 cm^{-1} and resembles an infrared reflectivity spectrum. This is not surprising, given the large dipole moment of the $\nu_s(SO_3)$ normal mode as evidenced by its strong IR intensity. The Raman spectrum shows a band at 1071 cm^{-1} with a very weak band at 1042 cm^{-1}. The relatively high frequency of the Raman band, presumably an A_g mode, is again consistent with a triflate ion in which each oxygen atom is coordinated by a lithium ion as demonstrated by the crystal structure.

The concentration dependence of the $\nu_s(SO_3)$ symmetric mode in solutions of LiTf in 2-pentanone is illustrated in Fig 3.6(a). The three bands that are clearly present in the IR intensity data were curve-fitted to three Gaussian peaks and a baseline. Fig. 3.6(b) shows integrated intensity of each band as a function of salt concentration. Here, concentration is the molal concentration (mol/kg of solvent) of salt. The relative amount of triple ions present (triangles) increases with increasing salt composition, while the relative amount of contact ion pair increases to a maximum at a composition of 1.25:1 (O:Li molar ratio) and then decreases with further increase in salt composition. The amount of "free" triflate ions appear to increase slowly with salt concentration. Triple ion species are dominant in the sample and increase with increasing concentration.

The symmetric SO_3 bending modes appearing between 620 and 680 cm^{-1} are shown in Fig. 3.7(a). There is a narrow band at 642 cm^{-1} for the 10:1 solution and a broad band at 654 cm^{-1} represents the crystal sample. Peaks at 668 cm^{-1} for

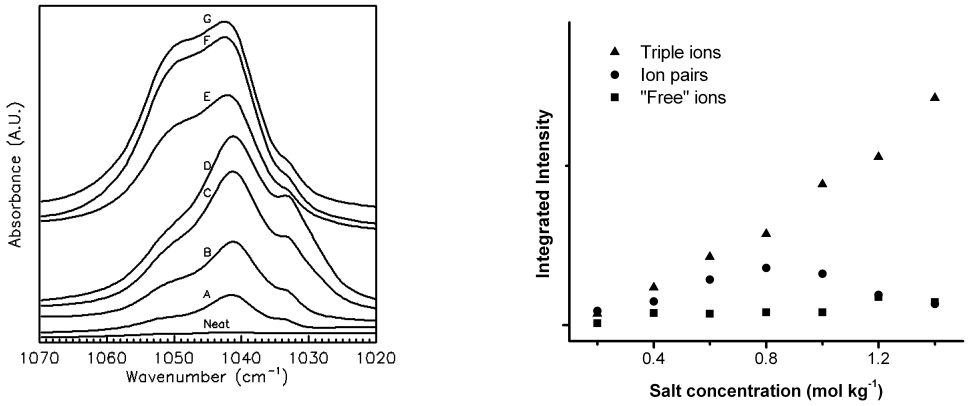

(a) **(b)**

Figure 3.6: (a) Concentration dependence of $\nu_s(SO_3)$ for LiTf:2-pentanone solution. The letters are designated as follows: (a) 0.2 (b) 0.4 (c) 0.6 (d) 0.8 (e) 1.0 (f) 1.2 (g) 1.4 mol/kg. (b) The plot of integrated intensity versus salt molal concentration.

both neat and solution samples have very weak intensity. Additional triflate ion modes appear in the IR spectral region 1100-1500 cm^{-1}, shown in Fig. 3.7(b). The bands at 1171 (solution) and 1195 cm^{-1} (crystal) are due to the triflate ion CF_3 antisymmetric stretching mode, $\nu_{as}(CF_3)$, while the bands at 1233 (solution) and 1227 cm^{-1} (crystal) are the triflate ion CF_3 symmetric stretching mode, $\nu_s(CF_3)$. The Raman spectrum (data not shown) has a weak band at 1232 cm^{-1} (solution) and a strong, sharp band at 1241 cm^{-1} (crystal). The IR spectrum of the triflate ion SO_3 asymmetric stretching mode, $\nu_{as}(SO_3)$, has bands at 1256, 1272, and 1303 cm^{-1} in the solution, whereas the crystal has a very broad, highly asymmetric feature with a maximum at 1259 cm^{-1}. The two-fold degeneracy of the $\nu_{as}(SO_3)$

mode in the isolated triflate ion is broken by any interaction with the potential energy environment that does not preserve the three-fold axis of symmetry of the anion. In the 10:1 solution, it is easy to visualize how coordination with one or two lithium ions would break down the symmetry. Thus, the two components at 1303 and 1256 cm^{-1} are assigned as symmetry-broken components of $\nu_{as}(SO_3)$, while the band at 1272 cm^{-1} can be assigned as a "free" triflate ion in a solution [6, 25]. An examination of the crystal structure shows that the triflate ion is three-fold coordinated by lithium ions, with one lithium ion to each oxygen atom. This might suggest an arrangement in which the three-fold axis of the isolated triflate ion is preserved in the crystal. However, a closer examination of the crystal structure shows that the lithium-triflate oxygen distances are slightly different: i.e. 1.932, 1.939, and 1.943 Å. Therefore these small differences are apparently sufficient to break the three-fold degeneracy and lead to the broad, structured feature in the spectrum of the crystal. The Raman spectrum of $\nu_{as}(SO_3)$ has two features at 1297 and 1274 cm^{-1} in the solution, with corresponding bands at 1308 and 1284 cm^{-1} in the crystal. Two peaks at 1368 and 1367 cm^{-1} for liquid and neat pentanone (data is not shown) samples, respectively, can be explained as methyl deformation modes or CH_2 wagging.

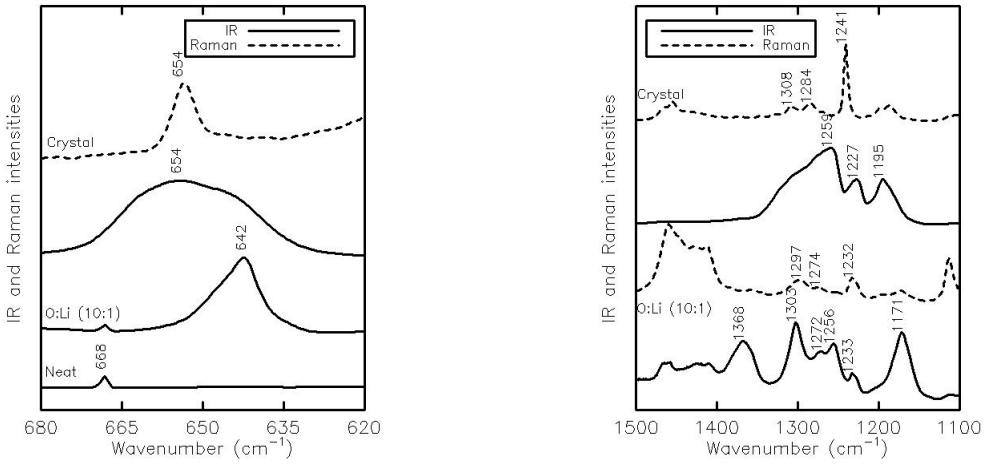

Figure 3.7: (a) Infrared and Raman spectra of $\delta_s(SO_3)$ symmetric bending mode (from 620 to 680 cm^{-1}) (b) Infrared and Raman spectra in the region of 1000-1500 cm^{-1}.

3.5 Vibrational Spectroscopy of NaTf:2-hexanone Crystal Structure

The packing diagram for crystalline NaTf:2-hexanone is shown in Fig 3.8. Na atoms are bonded to both triflate oxygen atoms and solvent oxygen atoms. The interaction between the solvent CO group and an Na atom was examined using vibrational spectroscopy.

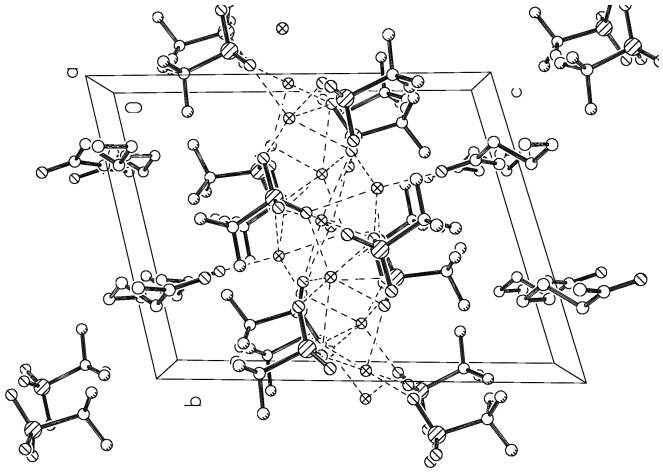

Figure 3.8: Packing diagram of the NaTf:2-hexanone crystal structure.

3.5.1 Carbonyl stretching vibrations, ν(CO)

Figure 3.9 illustrates the infrared and Raman spectra of the CO stretching mode of NaTf:2-hexanone crystal structure. In addition, it shows the IR spectra for the 10:1 solution and neat hexanone in the region of 1550-1750 cm^{-1}. Similar to pure-pentanone, the CO stretching mode of pure 2-hexanone is located at 1718 cm^{-1}. Further, this mode is slightly shifted to 1717 cm^{-1} in the O:Li = 10:1 solution. In the IR crystal spectrum, two bands are visible. A less intense band at 1721 cm^{-1} has a small shift ($\Delta\nu$ = 3 cm^{-1}) compared to pure hexanone frequency. These results show that solid state environment is significantly different than the liquid state. There is another broad asymmetric band feature at 1618 cm^{-1}. This band primarily originates from the Na ion coordination with the CO group; the Na-O distance in crystal is 2.274(11) Å. Therefore, a large frequency shift is expected compared to the pure ν(CO). It is also noted that there are two shoulders under this band envelope at 1618 and 1610 cm^{-1}. This may be due to the complexity of

NaTf:2-hexanone crystal structure.

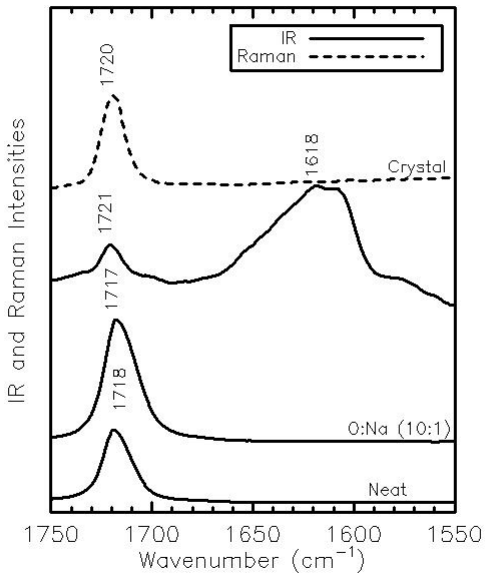

Figure 3.9: Infrared and Raman spectra of CO stretching region (from 1550 to 1750 cm^{-1}) for NaTf:2-hexanone crystal and pure pentanone

The CF_3 symmetric bending mode is shown in the Fig. 3.10(a). There are two bands at 760 and 772 cm^{-1} in the 10:1 solution IR spectrum. These two bands can be assigned to the triple ion and higher ion aggregates [6]. One narrow band appears at 768 cm^{-1} in the IR spectrum, whereas the Raman spectrum has a single band at 776 cm^{-1}. In the crystal structure, four triflate oxygen atoms coordinate with a Na ion. Therefore, it is not surprising to have relatively high frequency $\delta_s(CF_3)$ bands in the crystal.

The SO_3 symmetric stretching mode (1000 and 1080 cm^{-1}) has a strong asymmetric band at 1041 cm^{-1} as shown in Fig. 3.10(b). A curve fitting analysis shows that the asymmetric band is composed of three peaks which are assigned to free ion, ion pairs and triple ions. The IR spectrum of crystal structure consists of a

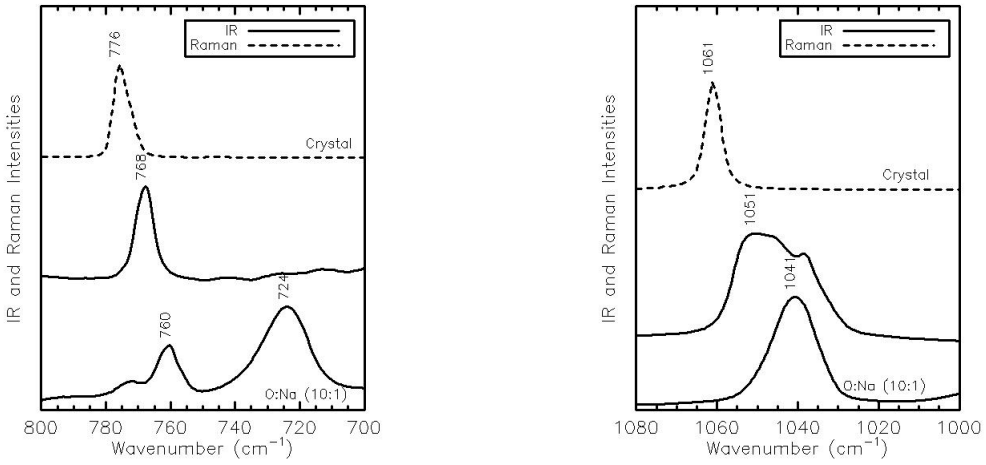

(a) **(b)**

Figure 3.10: (a) Infrared and Raman spectra of $\delta_s(CF_3)$ deformation region (from 700 to 800 cm^{-1}) for NaTf:2-hexanone crystal and 10:1 solution.(b) Infrared and Raman spectra of $\nu_s(SO_3)$ stretching region (from 1000 to 1080 cm^{-1}) for NaTf:2-hexanone crystal and 10:1 solution.

very broad band at 1051 cm^{-1} with a weak shoulder at a lower frequency. It is clearly shown that the Raman band shifts to higher frequencies when the crystal is formed.

3.6 Conclusions

In this chapter, we reported two crystal structures, LiTf:2-pentanone and NaTf:2-hexanone. Vibrational study reveals that cation ions (Li and Na) are coordinated with the carbonyl group of ketone in the both crystal structures. Further, these

data shows that CO stretching frequency shifts to the lower frequency side of the original mode due to cation coordination. The observed NaTf:2-hexanone crystal has a more complex environment than the LiTf:2-pentanone structure. Vibrational spectroscopic data shows that three ionically-associated species in the ketone-salt solutions are "free" ions, ion pairs, and ion aggregates. When the crystals form, broad band features are observed on the higher frequency side. This may be expected due to the cation coordination with the each oxygen atom of triflate ions, i.e. the triflate ion vibrates as if it were an $[Li_3Tf]^{2+}$ entity in LiTf:2-pentanone. These crystal structure data give supporting evidence to the molecular interactions we discussed in chapter 2.

References

[1] A. M. Christie and C. A. Vincent, J. Phys. Chem. **100**, 4618 (1996).

[2] Y. M. M. Ishikawa, S. Wen, J. Phys. Chem. **45**(2), 229 (1993).

[3] K. Xu, Chem. Rev. **104**, 4303 (2004).

[4] N. Choi, Electrochim. Acta **46**(10-11), 1453 (2001).

[5] S. Ramesh and K. C. Wong, Ionics **15**, 249 (2009).

[6] W. Huang, R. Frech, and R. A. Wheeler, J. Phys. Chem. **98**, 100 (1994).

[7] J. R. Stevens and P. Jacobsson, Can. J. Chem. **69**, 1980 (1991).

[8] R. S. Mulliken, J. Am. Chem. Soc. **72**, 600 (1950).

[9] R. S. Mulliken, J. Chem. Phys. **56**, 801 (1952).

[10] A. Pullin and J. Pollock, Trans. Faraday Soc. **54**, 11 (1958).

[11] N. A. Slovokhotova, Zh. Fiz. Khim. **25**, 768 (1951).

[12] H. Yamada, Bull. Chem. Soc. Japan, **33**(6), 780 (1960).

[13] H. Yamada, Bull. Chem. Soc. Japan, **33**, 666 (1960).

[14] *Data Collection: SMART Software Reference Manual*, Bruker-AXS, 5465 E. Cheryl Parkway, Madison, WI 53711-5373, USA (1998).

[15] *Data Reduction: SAINT Software Reference Manual*, Bruker-AXS, 5465 E. Cheryl Parkway, Madison, WI 53711-5373, USA (1998).

[16] *G. M. Sheldrick SHELXTL Version 6.10 Reference Manual*, Bruker-AXS, 5465 E. Cheryl Parkway, Madison, WI 53711-5373, USA (2000).

[17] *International Tables for Crystallography*, vol. C (Tables 6.1.1.4, 4.2.6.8, and 4.2.4.2, Kluwer: Boston, 1995).

[18] G. M. Sheldrick, *SADABS. Program for Empirical absorption Correction of Area Detector Data.*, University of Göttingen, Germany (2007).

[19] J. M. Alia, Y. D. Mera, H. G. M. Edwards, F. J. Garca, and E. E. Lawson, J. Mol. Struct. **408-409**, 439 (1997).

[20] R. Frech and W. Huang, J. Sol. Chem **23**(4), 469 (1994).

[21] J. Alia and H. Edwards, Vib. Spectrosc. **24**, 185 (2000).

[22] H. Yamada and K. Kozima, J. Am. Chem. Soc. **82**, 1543 (1960).

[23] C. P. Rhodes and R. Frech, Macromolecules **34**, 2660 (2001).

[24] R. Frech, S. Chintapalli, P. G. Bruce, and C. A. Vincent, Chem. Commmun. p. 157 (1997).

[25] S. P. Gejji, K. Hermansson, J. Tegenfeldt, and J. Lindgren, J. Phys. Chem. **97**(44), 1140211407 (1993).

[26] M. Petrowsky, R. Frech, S. N. Suarez, J. R. P. Jayakody, and S.Greenbaum, J. Phys. Chem. B **110**(46), 23012 (2006).

[27] A. G. Bishop, D. R. MacFarlane, D.McNaughton, and M.Forsyth, J. Phys. Chem. **100**, 2237 (1996).

Chapter 4

Quantitative Analysis of Temperature-Dependent Vibrational Modes of Pure PEO and PEO-Lithium Triflate Complexes

4.1 Introduction

We have previously reported (see Chapter 2) that the intensities of $\nu_s(SO_3)$, $\delta_s(CF_3)$, and $\delta_s(SO_3)$ vibrational modes are independent of lithium ion association in LiTf:2-pentanone system using IR spectroscopy. As we explained in Chapter 2, absorption is proportional to the concentration of the sample species. The intensity of triflate ion vibrational modes appear to obey Beer's law, and molar absorptivities were calculated for $\nu_s(SO_3)$, $\delta_s(CF_3)$, and $\delta_s(SO_3)$ vibrational modes of CF_3SO_3 anion. Further, we concluded that those results can be used to find the sample thickness and the exact concentration of different samples.

In order to carry out quantitative studies of polymer electrolytes, several difficulties needed to be overcome. One such issue is preparing a sufficiently thin uniform sample. Another problem is controlling the sample thickness at higher temperatures. In addition, a number of interactions occur simultaneously due to the complex environment of the polymers, while varying the temperature and concentration. Therefore, great care is needed during sample preparation and vibrational spectroscopic measurements to obtain successful results. Generally, a polymer consists of crystalline and amorphous phases. The relative amount of the material in each phase changes with increasing temperature. Fourier transform

infrared spectroscopy is used to probe ion-polymer and ion-ion interactions of electrolytes both qualitatively and quantitatively.

A number of groups have studied polymer-salt phase diagrams using different techniques [1–3]. Fig. 4.1 shows the phase diagram of the PEO:LiTf system [2]. This diagram reveals the two phases for the PEO:LiTf complex below the melting temperature: crystalline PEO and the crystalline PEO:LiTf (3:1) compound. These crystalline PEO phases transform into an amorphous PEO:LiTf compound and an amorphous PEO above the melting temperature. According to the phase diagram, pure PEO starts to melt at around 60°C and the PEO:LiTf complex melts around 140°C [4–8]. Furneaux *et al.* showed the validity of an extended version of Beer's

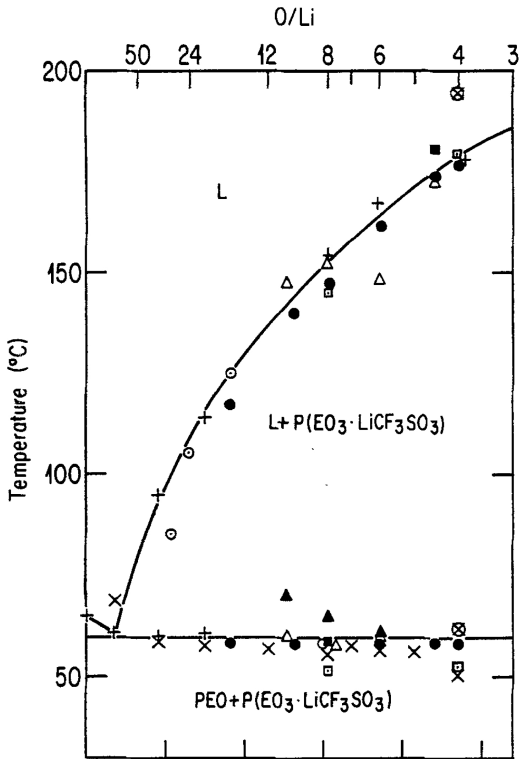

Figure 4.1: Phase diagram of the PEO:$LiCF_3SO_3$ system. L represents the amorphous phase [2].

law for the $\delta(CF_3)$ vibrational mode in PEO:LiTf complexes [9]. They showed that the intensity of $\delta(CF_3)$ mode is independent of Li^+ association. In this work, the AsF_6^- band located at 700 cm^{-1} has been used as a standard marker to scale other bands since the absorption of AsF_6^- does not change with temperature. To extend these studies, we measured the FTIR spectra of PEO:LiTf while varying the temperature and concentration. Our interest is to quantitatively study polymer electrolyte systems by finding the amount of polymer material in different phases. The relative areas of individual peaks of the spectrum is related to the relative amount of material. However, the data should be smoothed to yield satisfactory results. It is important to avoid unwanted noise in spectra. A number of techniques have been used to minimize noise in the FTIR spectra during past years. Among them, smoothing techniques are a powerful tool, e.g., Savitky-Golay (SG) algorithm, spline filtering, Fourier filtering, wavelet denoising, etc. [10].

Our major goal was to find a suitable method to minimize noise in the spectra and define a proper baseline for required spectral regions. Another objective was to study the changes of the vibrational modes of triflate ion, AsF_6^- band and the polymer configuration region with temperature and concentration. To investigate these, we used IDL programming and Origin Curve fitting software to analyze the data. The area was calculated by a direct integration method. However, there are certain problems associated with each method, and we report only successful results of this project.

4.2 Experimental Methods

Poly(ethylene oxide), PEO 2000 Da was purchased from Polysciences, Inc. Lithium hexafluroarsenate ($LiAsF_6$, 99%), $LiCF_3SO_3$, acetonitrile (CH_3CN) were obtained from Alrich or Alfa Aesar. PEO was heated for 48 hours in a vacuum oven at 10^{-2} mbar at 45-50°C; LiTF was heated in a vacuum oven at 105°C for several days. All materials were stored in an argon-filled glove box ($\leq$ 1 ppm H_2O). First, a large batch of PEO:$LiAsF_6$ with 500:1 solution was prepared. To prepare this solution, weighed amounts of dried PEO and $LiAsF_6$ were dissolved in CH_3CN and stirred at room temperature for at least 24 hours. Then the solution was poured into a teflon-lined petri dish and left in a dry box for several days for solvent evaporation. Finally, a white thick film was observed on the petri dish; this film was easily broken into flakes. This compound is called doped PEO (PEO:$LiAsF_6$=500:1) and it was the host polymer compound for all other sample preparations.

PEO-salt solutions were prepared with a particular ether oxygen (EO):Li ratios. This ratio was marked as x:1 hereafter; where x is the amount of doped PEO. PEO-salt solutions were made by dissolving measured amounts of doped PEO and LiTf into CH_3CN solvent. Five such solutions were made with different x:1 ratios (x = 10, 15, 20, 30, 40).

All IR spectra were recorded using IFS66V FTIR spectrometer under vacuum (11 mbar). The sample was mounted on the temperature controlled transmission cell (Harrick Inc.). All spectra were collected at a spectral resolution 1 cm^{-1}, 64 scans, and 400-4000 cm^{-1} mid IR spectral range. Before taking the sample

spectrum, a background spectrum was collected from the optical window without a sample. Then the optical window was transferred to the glove box. A few PEO-salt solution drops were cast onto the CdTe window and a thin film was obtained after 24 hours. This solvent-free thin film on the CdTe window was used as the sample for IR temperature measurements. A single window was used to reduce Fabry-Perot interference effects. Each sample was heated to 80°C and sat for 1 hour until temperature stabilization. The sample was then cooled back to room temperature and left to stabilize for 1 hour. This method was followed to obtain a moisture and morphological effect free sample. Furneaux *et al.* reported that sample thickness does not change substantially due to this heating and cooling process [9]. The sample temperature was varied from room temperature (25°C) to 140°C with 10 degree increments for PEO-salt samples and 5 degree increments for pure PEO sample. At each temperature, the sample was allowed to stabilize for 30 minutes. The sample temperature was monitored using an Omega temperature controller(model-CN9000A) and measured with a K-type thermocouple. The exported ASCII data files using OPUS software were imported into IDL to perform data smoothing and integration. All data sets were analyzed using IDL programming.

4.2.1 Data collection

Temperature-dependent IR spectra of pure PEO sample

A series of infrared spectra were taken for pure PEO over the temperature range of 25 to 125°C at 5 degree increments. Fig. 4.2 illustrates the IR spectrum of pure PEO in the range of 700 to 1500 cm^{-1}. It was noticed that the band frequencies

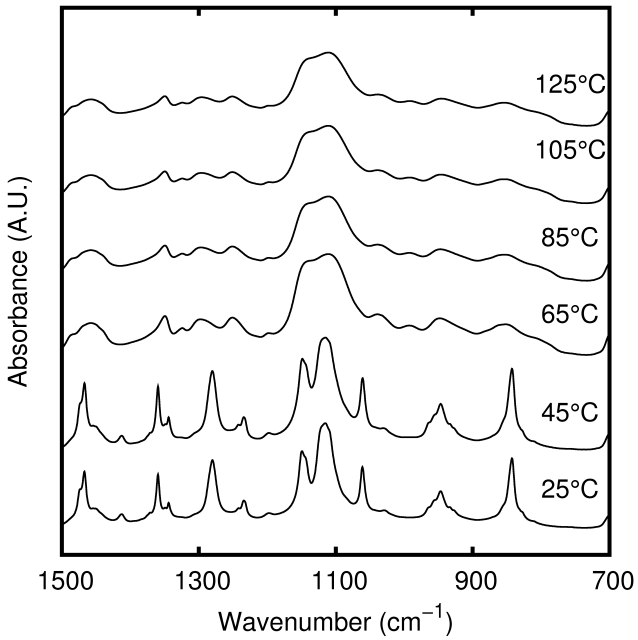

Figure 4.2: Temperature-dependent FTIR spectra of pure PEO in the region from 700 to 1500 cm^{-1}.

are constant even though their intensities changed with temperature. In a pure PEO IR spectrum, bands were observed at 827, 843, 857, 933, 947, 965, 947, 1061, 1050, 1235, 1243, 1280, 1344, 1360, 1467 and 1475 cm^{-1}. These bands disappear above 60 °C and hence, are assigned to the crystalline phase of PEO. On the other hand, broad bands located at 855, 948, 993, 1111, 1143, 1251,1294, 1324, 1350, 1456 and 1486 cm^{-1} are attributed to the amorphous phase of PEO. The frequencies of these spectral bands are consistent within ± 1 cm^{-1} with the band assignments published by Dissanayake *et al.* [6]. As the temperature increases, the crystalline amount decreases while the amount of amorphous compound is increased.

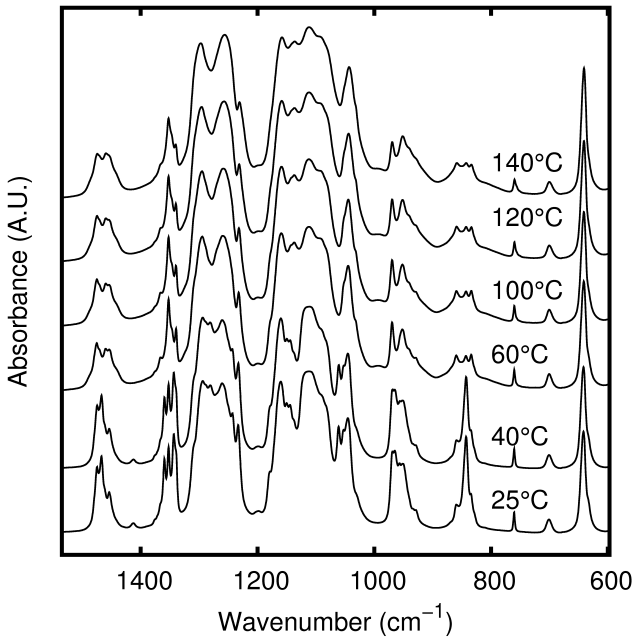

Figure 4.3: Temperature-dependent FTIR spectra of PEO:LiTf 10:1 in the region from 600 to 1500 cm^{-1}.

Temperature-dependent IR spectra of PEO$_x$LiTf complexes

In PEO:LiTf complexes, Li cations are coordinated by the ether oxygen atoms of the polymer backbone. It is expected that polymer conformational changes are due to the complexation with salts. The ion-ion and ion-polymer interactions of LiTf in polymers have been studied by a number of research groups during the last decade, and these studies have revealed that there exists different ionic species of the triflate anion, such as "free" ions, contact-ion pairs, triple ions, and higher ion aggregates [1, 8, 11–14]. Fig. 4.3 shows the FTIR spectra of a PEO:LiTf 10:1 sample in the range between room temperature (25°C) and 140°C. The shape of the spectral bands significantly changes with the temperature. It is noted that the

bands are broadened in the region between 60 and 140 °C due to the phase changes. Therefore, data between 25 to 80°C were used for quantitative analysis since it is difficult to define a proper baseline at higher temperatures.

The temperature-dependent spectra in the region 680 to 720 cm^{-1} are shown in Fig. 4.4. Bands that appear at 760 and 640 cm^{-1} are assigned to the symmetric CF_3 deformation mode, $\delta(CF_3)$, and the symmetric SO_3 deformation mode, $\delta(SO_3)$, of the CF_3SO_3 anion, respectively. The band at 700 cm^{-1} is due to the $\nu_3(AsF_6)$ mode. As mentioned earlier, this band is expected to have the same absorption intensities for each temperature [9]. Therefore, AsF_6^- was used as a standard to normalize the IR spectra in this work.

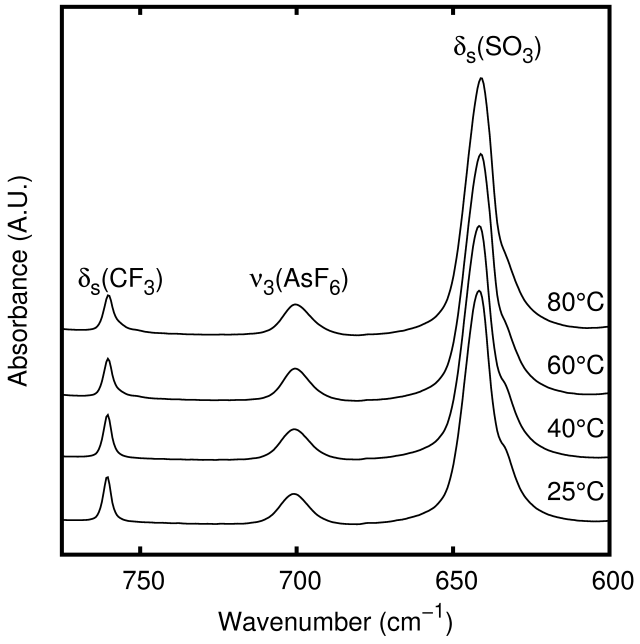

Figure 4.4: Temperature-dependent FTIR spectra of PEO:LiTf 10:1 in the region from 600 to 775 cm^{-1}.

Concentration-dependent IR spectra of PEO_xLiTf complexes

The spectral region 800-1000 cm^{-1} is the fingerprint region for the polymer compound. This region is useful to understand the changes of local conformation due to the complexation in PEO, and it is expected that PEO exhibits new conformers with increasing salt concentration. Fig. 4.5 shows the concentration dependent IR spectra of PEO_xLiTf complexes in this range. The bands that appear in 800-900 cm^{-1} are due to CH_2 rocking vibrations, while the bands at 900-1000 cm^{-1} are primarily attributed to CO stretching motion [5, 6]. Modes in the spectral region 800-1000 cm^{-1} consists of mixed CH_2 rocking and CO stretching motions.

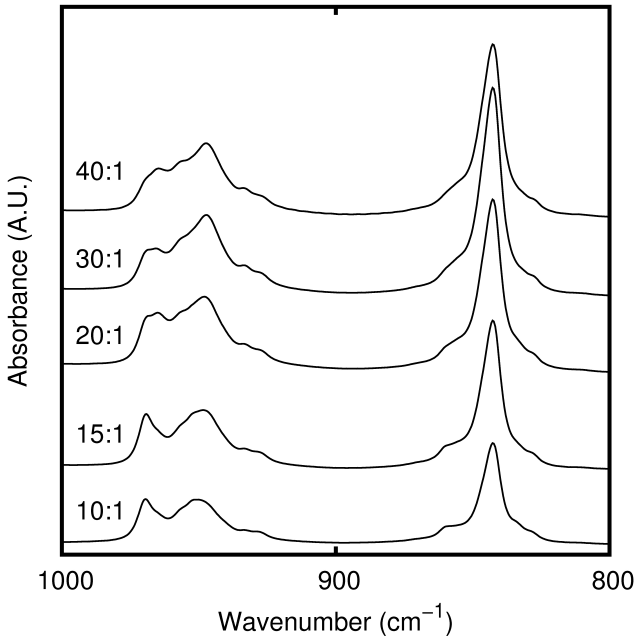

Figure 4.5: Concentration dependence FTIR spectra of PEO:LiTf complexes in the region from 800 to 1000 cm^{-1}.

4.2.2 Data analysis

Vibrational spectroscopy data were analyzed using several steps. First, the original data were normalized using an AsF_6^- marker. Then a baseline correction was applied for all required regions of this normalized data. Fourier filtering with low pass and band pass filtering and cubic spline fitting was initially used with limited success. Accordingly, third order Savitzky-Golay filtering was chosen to smooth all spectra used. Since this is a quantitative study, the area under spectral band is of utmost importance. The integrations were carried out with the five point Newton-Cotes formula (IDL's INT_TABULATED routine).

The first step was to isolate the AsF_6^- peak. We chose an extended region around this peak and then found an optimum frequency interval by minimizing the area due to noise in the tail. The derivative of the entire region was obtained using a Savitzky-Golay filter, then a liner fit to the derivative of the two tail regions alone was subtracted to remove third order contributions from the tail. Integrating this gave a smooth peak with a well behaved tail. Finally, we minimized the area of this tail over different frequency ranges to find the best frequency interval to find the area of the AsF_6^- peak. The total area under a curve at different temperatures was calculated and the area at the room temperature was treated as the reference area. All spectra were normalized by multiplying by the ratio between the area of the AsF_6^- peak and the reference area. The normalized spectra of both pure PEO and PEO:LiTf were used in all further studies.

Smoothing IR spectra

The most important step in quantitative analysis of a spectrum is the proper handling of the baseline correction. Various noise elements contribute to small changes in transmission intensity causing tails of spectral bands to deviate from a simple Gaussian shape. As mentioned earlier, the amount of species is determined from the area under a peak, and it is vital to have a proper baseline in order to accurately determine this. Simple techniques such as moving average, may remove actual features of spectra and hence, cannot be utilized in baseline correction. Therefore, we use third order Savitzky-Golay smoothing with ten points before and after for smoothing the region of interest of the spectrum. This was done by simply convolving the above mentioned Savitzky-Golay filter with the data. We then use two different methods for baseline correction: a polynomial-fit based method and a technique adapted from Liu *et al.* [15]. The fact that the AsF_6^- amount is constant in every spectrum is used to compare both methods extensively. The range 716-672 cm^{-1} is chosen around the AsF_6^- peak, the baseline is corrected for each temperature, and the resultant area inside the peak is measured and compared.

The basic idea behind the first method is that the tails can be approximated by a straight line. We start by finding the local minima of each tail, and then 20 data point ranges were selected from either side. Each side was then fitted with quadratic polynomials of the form $a + bx + cx^2$. A simple least square calculation

is used to obtain the coefficients as,

$$\begin{pmatrix} a \\ b \\ c \end{pmatrix} = \begin{pmatrix} n & \sum x_i & \sum x_i^2 \\ \sum x_i & \sum x_i^2 & \sum x_i^3 \\ \sum x_i^2 & \sum x_i^3 & \sum x_i^4 \end{pmatrix}^{-1} \begin{pmatrix} \sum y_i \\ \sum x_i y_i \\ \sum x_i^2 y_i \end{pmatrix}.$$

The sum runs over all $n = 20$ data points (x_i, y_i) under consideration. This allows us to calculate the minima of each side by finding the zero point of the second derivative of the parabola given by $x_{min} = -b/2c$. The line joining these two points is considered the baseline correction in this method and hence, it was subtracted from the entire data range before integrating the peak to find the enclosed area.

Liu *et al.* proposed to fit the entire spectrum with a straight line or a quadratic polynomial and rejected data points that are one standard error or more away [15]. This procedure is repeated until the difference between the fit and the remaining data points is less than a preset tolerance limit. The tolerance should be sufficiently small and has no direct influence on the final result if enough data points are used. We tested this technique with n-tuple polynomials and found a quadratic fit is best for the AsF_6^- peak. The two programs that we used for quantitative studies are attached in the appendix 1(program 1 and 2).

4.3 Results and Discussion

In this section, we report results obtained using the latter method (Liu method [15]), since it was the most consistent. Fig. 4.6(a) shows the temperature-dependent IR spectra for the the AsF_6^- peak in pure PEO after baseline correction. Similarly, the same baseline correction was applied for PEO:LiTf complexes. The relative

intensity variation of AsF_6^- peak in the PEO:LiTf complex is shown in Fig. 4.6(b). According to this graph, intensities are constant at each temperature as we expected. This result verifies that an AsF_6^- band can be used as a marker to scale other spectral regions and to verify the validity of the technique. We examined the relative areas of the $\delta_s(CF_3)$ and $\delta_s(SO_3)$ vibrational modes and bands in the polymer fingerprint region using the same method.

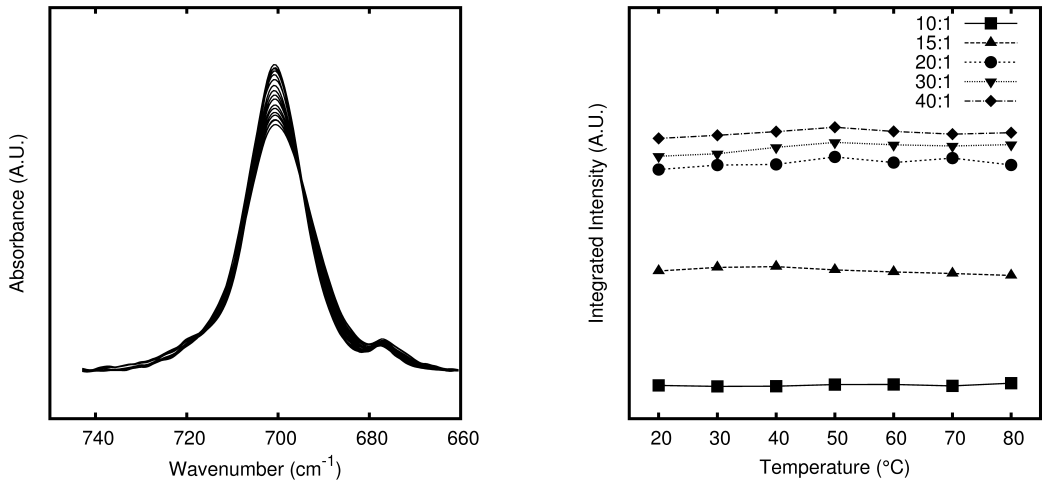

(a) **(b)**

Figure 4.6: Baseline corrected FTIR spectra of AsF_6^- in pure PEO

Figure 4.7 illustrates the relative integrated intensities of PEO:LiTf complexes plotted as functions of temperature in the region 800 to 900 cm^{-1} (see Fig. 4.5). This figure clearly demonstrates that the total intensity is unchanged until 40°C, and then it starts to decrease during the intermediate temperature at 50°C. Upon heating above 60°C, intensities for all concentrations remained constant. Similar behavior was observed for the 900-1000 cm^{-1} spectral region. This change can

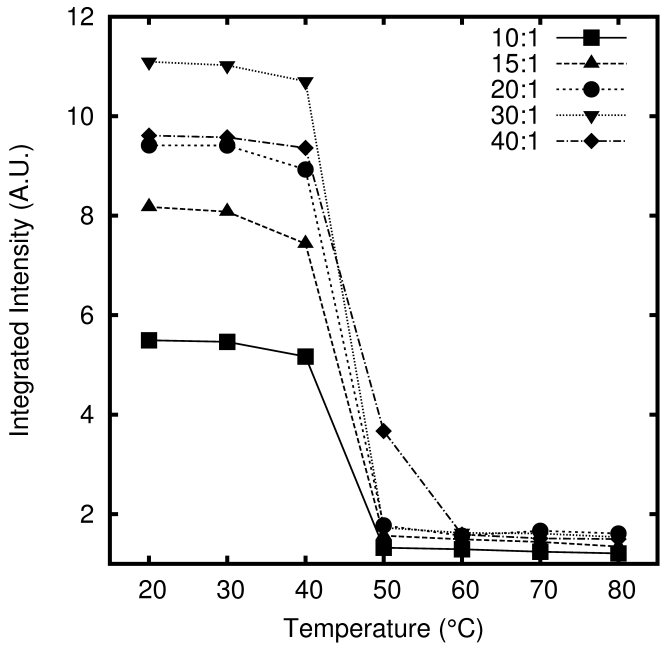

Figure 4.7: Relative intensity versus temperature for PEO_xLiTf complexes in the region 800 to 900 cm^{-1}.

be attributed to the phase change from crystalline to amorphous of the polymer complex. However, it is interesting to observe this behavior not only in the polymer region but also in the ionically associated regions. Temperature-dependent integrated intensities of $\delta_s(CF_3)$ and $\delta_s(SO_3)$ modes are shown in Fig. 4.8(a) and (b), respectively.

Previous studies based on Beer's law suggest that the total intensity of a $\delta(CF_3)$ peak is independent of ionic association; hence, we expect constant absorption intensity across all temperatures [9]. On the contrary, we observed a clear change of intensity around 60°C. One possible reason may be the phase change from crystalline to amorphous of the PEO around the same temperature. Another

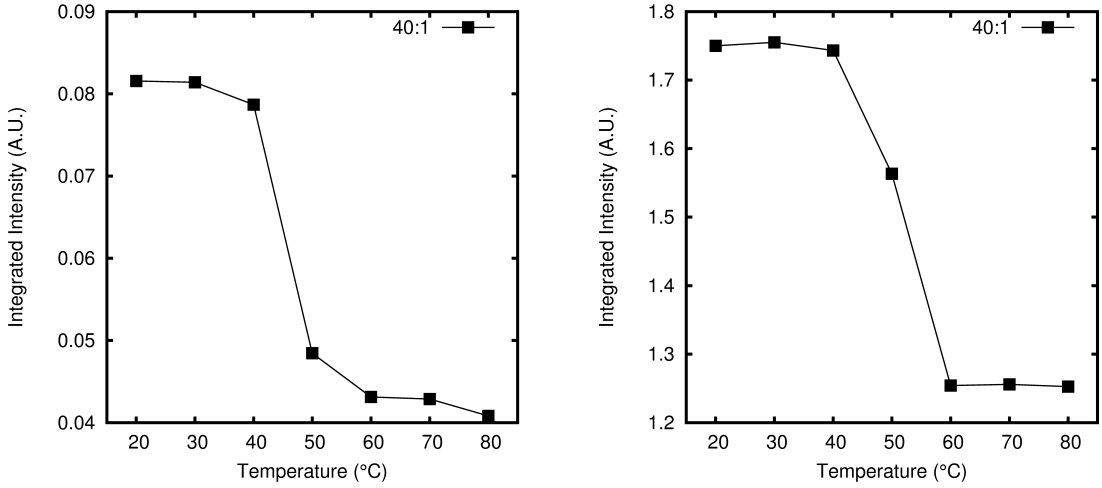

(a) **(b)**

Figure 4.8: (a) Relative intensity versus temperature for (a) $\delta_s(CF_3)$ mode (740-770 cm^{-1}) (b) $\delta_s(SO_3)$ mode (600-675 cm^{-1}) in PEO:LiTf 40:1 complex.

possible explanation is the wiggles on the tail that might affect the region selection process by the code. With a sharper peak, the intensities of the wiggles are negligible compared to a lower intensity, broader peak. Also, baseline selection may be affected by the peak broadening as it becomes curved for higher temperatures. As a solution, a Gaussian curve fitting procedure was attempted with a similar result. Therefore, we propose to use a different number of Gaussian lines depending on the temperature. This was left as future work. Another explanation would be to assume that areas under peaks interchange due to ionic interactions caused by phase change. One plausible explanation could be that the area change occurs at

the phase transition temperature. However, further investigations are necessary to understand this phenomena.

4.4 Conclusions

We used an algorithm to define proper baselines of FTIR spectral regions and normalize based on the constant intensity an AsF_6^- peak from doping. Resulting spectra yields a constant area for the AsF_6^- peak, although the same is not true for other peaks. The total intensity is not constant for the polymer region due to the phase transformation from the crystalline phase to the amorphous phase of PEO. According to previous studies, the intensity of the $\delta(CF_3)$ mode is independent of Li^+ association, and thus, we expected a constant intensity with temperature. However, it is not observed in our results. Several possible scenarios have been proposed and further investigations are necessary to exactly understand this discrepancy.

References

[1] A. Vallee, S. Besner, and J. Prud'homme, Electrochim. Acta **37**(9), 1579 (1992).

[2] C. D. Robitaille and D. Fauteux, J. Electrochem. Soc. **133**, 315 (1986).

[3] M. Z. A. Munshi and B. B. Owens, App. Phys. comm. **6**(4), 279 (1986-1987).

[4] R. Frech, S. Chintapalli, P. G. Bruce, and C. A. Vincent, Macromolecules **32**(3), 808 (1999).

[5] R. Frech and W. Huang, Macromolecules **28**(4), 1246 (1995).

[6] M. A. K. L. Dissanayake and R. Frech, Macromolecules **28**(15), 5312 (1995).

[7] C. P. Rhodes, *Crystalline and Amorphous Phases in Polymer Electrolytes and Model Systems*, Ph.D. thesis, University of Oklahoma, The Department of chemistry and Biochemistry, Norman (2001).

[8] V. A. Seneviratne, *Local Structures in Poly(Ethylene Oxide) - LiX(X=SbF_6, BF_4, CF_3SO_3 and Glyme -LiX(X=SbF_6, BF_4) systems*, Ph.D. thesis, University of Oklahoma, The Department of Physics and Astronomy, Norman (2004).

[9] J. E. Furneaux, A. M. McCoy, V. Seneviratne, and R. Frech, in *Proceedings of the 10th Asian Conference on Solid State Ionics Advanced Materials for Emerging Technologies* (World Scientific, 2006), p. 469.

[10] A. Savitzky and M. J. E. Golay, Analytical Chemistry **36**(8), 1627 (1964).

[11] W. Huang and R. Frech, Polymer **35**(2), 235 (1994).

[12] R. Frech and W. Huang, Solid State Ionics **72**, 103 (1994).

[13] J. R. MacCallum and C. A. Vincent, *Polymer Electrolyte Reviews 1* (Elsevier Applied Science Publishers Ltd., 1987), 1st ed.

[14] J. R. MacCallum and C. A. Vincent, *Polymer Electrolyte Reviews 2* (Elsevier Applied Science Publishers Ltd., 1989), 1st ed.

[15] J. Liu and J. L. Koenig, Appl. Spectros. **41**(3), 447 (1987).

Chapter 5

Temperature-Dependent Ion and Mass Transport of TbaTf-n-acetates and 2-ketones

Portions of this chapter have appeared in:

Bopege, D. N.; Petrowsky, M.; Fleshman, A. M.; Frech R.; Johnson, M. B. *J. Phys. Chem. B* **2012**, *116*, 71-76

Bopege, D. N.; Petrowsky, M.; Frech R.; Johnson, M. B. " Mass and Ion Transport in Pure Ketones and Dilute Ketone solutions." *J. Phys. Chem. Lett.*, to be submitted(2012)

5.1 Introduction

It is important to understand charge and mass transport in organic liquid electrolytes and polymer electrolytes (PEs) due to their importance in applications such as lithium rechargeable batteries and other electrochemical devices [1–4]. The temperature dependence of ionic conductivity and diffusion in these electrolytes can provide information about complex system dynamics. The simple Arrhenius equation shown in Eq. 5.1 describes the temperature dependence of ionic conductivity below the glass transition temperature, T_g, for PEs [5–8].

$$\sigma = \sigma_0 \mathrm{e}^{-\frac{E_a}{RT}} \tag{5.1}$$

Here σ denotes the ionic conductivity, σ_0 is the temperature independent prefactor, T is the temperature, and E_a is the activation energy. It has been found that liquid

electrolytes and PEs above T_g often show non-Arrhenius temperature-dependent conductivity that is commonly described using the VTF or the WLF empirical equations [9–12]. Because these are empirical equations, the resulting fitting parameters do not provide information on the underlying mechanism of ion transport. Conductivities and diffusion coefficients are conventionally described with viscosity-related models that often predict results contrary to experiment [3, 4, 13].

Recently, a new approach has been proposed to describe charge and mass transport in pure liquids and liquid electrolytes [14–17]. The temperature-dependent conductivity is formally written as an Arrhenius-like expression; however, in contrast to Eq. 5.1, there exists a temperature dependence in the exponential prefactor that is due to the temperature dependence of the solvent/solution static dielectric constant (ε_s). Therefore, the ionic conductivity can be written as

$$\sigma(T, \varepsilon_s) = \sigma_0(\varepsilon_s(T))\mathrm{e}^{-\frac{E_a}{RT}} \tag{5.2}$$

The compensated Arrhenius formalism (CAF) has been used to describe self-diffusion and dielectric relaxation transport phenomena in addition to ionic conductivity [14, 17]. The self-diffusion coefficients(D) and dielectric relaxation rate constant(k) can be presented in the following form analogous to 5.2.

$$D(T, \varepsilon_s) = D_0(\varepsilon_s(T))\mathrm{e}^{-\frac{E_a}{RT}} \tag{5.3}$$

$$k(T, \varepsilon_s) = k_0(\varepsilon_s(T))\mathrm{e}^{-\frac{E_a}{RT}} \tag{5.4}$$

Here, $D_0(\varepsilon_s(T))$ and $k_0(\varepsilon_s(T))$ are the exponential prefactors.

This dielectric constant dependence in the prefactor is removed by using a

scaling procedure that requires a reference curve. A reference conductivity curve is constructed from the isothermal conductivity and static dielectric constant values of each member of a solvent family. The temperature at which each reference conductivity is measured is termed the reference temperature, T_r. The end result of this scaling procedure is the compensated Arrhenius equation (CAE) [14–20]. Eq. 5.5 and 5.6 are compensated Arrhenius equations for ionic conductivity and self-diffusion, respectively.

$$\ln\left[\frac{\sigma(T,\varepsilon_s)}{\sigma(T_r,\varepsilon_s)}\right] = -\frac{E_a}{RT} + \frac{E_a}{RT_r} \tag{5.5}$$

$$\ln\left[\frac{D(T,\varepsilon_s)}{D_0(T_r,\varepsilon_s)}\right] = -\frac{E_a}{RT} + \frac{E_a}{RT_r} \tag{5.6}$$

If CAE behavior is observed, a plot of $\ln(\sigma(T,\varepsilon_s)/\sigma(T_r,\varepsilon_s))$ versus $1/T$ yields a straight line with slope $-E_a/R$ and intercept $E_a/(RT_r)$. The activation energy can be calculated from either the slope or the intercept of Eq. 5.5 or 5.6. The agreement between these two activation energies provides one measure of the validity of this procedure. This activation energy is used to determine the exponential prefactor, σ_0, by dividing $\sigma(T,\epsilon_s)$ by the Boltzmann factor ($\exp[-\frac{E_a}{RT}]$). Previous work has shown that a master curve results when the prefactors are plotted against the dielectric constant [14–17]. The formation of a master curve supports the postulates underlying Eq. 5.2.

Translational diffusion data complement ionic conductivity data in studies of transport in an electrolyte. Pulsed Field Gradient Nuclear Magnetic Resonance (PFG-NMR) spectroscopy is a powerful tool for determining diffusion coefficients and is used in this work and related studies [21–30]. It has been shown that

temperature-dependent diffusion coefficients exhibit the same compensated Arrhenius behavior as ionic conductivities [14]. The temperature dependence of both ionic conductivities and self-diffusion coefficients for alcohol-based electrolytes and pure alcohols, respectively, have been studied using the CAF [14, 15]. Similar studies must be performed for other solvent systems in order to test the generality of this approach.

This chapter describes the temperature-dependent conductivities and self-diffusion coefficients of pure solvents and dilute liquid electrolytes. In this study, the temperature dependence is examined for 0.0055 M TbaTf-acetate, 0.0055 M TbaTf-acetate, pure acetate, and pure ketone systems. In the conductivity studies, TbaTf was chosen as the solute because it minimizes the cation-anion interactions in solution. The bulky butyl groups prevent contact ionic association and therefore only "free" ions exist in solution [31, 32]. The main objective of this work is to examine the validity of the CAF using pure acetates, pure ketones and dilute acetate and ketone based electrolytes. Ketones and acetates are both aprotic solvents with structural similarities in that they have carbonyl groups. However, the permittivity of ketones is much higher than that for acetates. Considering the prominent role the dielectric constant plays in transport phenomena, it is important to compare conductivity and diffusion data between ketones and acetates. Here, the dependence of the activation energy on alkyl chain length is also examined.

5.2 Experimental Methods

5.2.1 Sample preparation

All acetates, ketones and TbaTf were purchased from either Aldrich or Alfa Aesar and used as received. All materials were stored and electrolyte solutions were prepared in a dry box under a nitrogen atmosphere ($\leq$ 1 ppm H_2O and approximate temperature 25°C). A 0.0055 M (molar concentration, mol/L) sample was made by dissolving an appropriate amount of TbaTf into a particular acetate or ketone solvent, followed by stirring for 24 hours.

5.2.2 Conductivity and static dielectric constant measurements

For the conductivity and dielectric constant measurements, the dilute solution or pure solvent was contained in a liquid cell (HP 16452A with 2 mm spacer) immersed in an oil bath [33]. The capacitance and conductance were measured at each temperature with an impedance analyzer (HP 4192A scanning the frequency range 1 kHz to 13 MHz). The measured conductance, in conjunction with the known cell geometry, was used to determine the solution conductivity at each temperature. The conductivity (σ) is calculated using the relation $\sigma = LG/A$, where L is the electrode gap, G is the measured conductance, and A is the electrode area. Temperature was controlled using using a Huber ministat 125 with an accuracy ±0.1°C. All measurements were carried out over a temperature range from 0 to 80°C for acetates and 5 to 80°C for ketones. The solution and pure solvent static dielectric constants were calculated using the relation $\varepsilon_s = \alpha C/C_0$,

where C is the sample capacitance and C_0 is the atmospheric capacitance. The parameter α, which is close to unity, accounts for stray capacitance [33].

5.2.3 PFG NMR self-diffusion measurements

An NMR capillary tube (5 mm OD and 20 cm long) was filled to a 0.8 cm height with pure acetate or ketone solvents for the NMR-PFG measurements. This tube was sealed with parafilm after filling the sample in a drybox ($\leq$ 1ppm H_2O). PFG measurements were performed using a Varian VNMRS 400 MHz NMR spectrometer, which was operated with an Auto-X-Dual broad band 5 mm probe tuned to 399.870 MHz for protons. The standard Stejskal-Tanner pulsed gradient sequence was performed at each temperature by arraying the gradient field strength from 6 to 62 G/cm [24, 34–36]. The integrated intensity of each attenuated signal was calculated. The diffusion coefficient was calculated from the slope of the plot Ln(intensity) versus square of the gradient strength. Temperature was controlled using an FTS XR401 air-jet regulator. The duration of the gradient pulse encompassed the range from 0.27 ms (butyl acetate at 70°C) to 1.7 ms (decyl acetate at 0°C). Similarly, gradient pulse of duration was varied for ketones from 0.225 ms (2-pentanone at 65°C) to 1 ms (2-decanone at 5°C).

5.3 Results and Discussion

5.3.1 Temperature dependence of ion transport in Tbatf-aprotic solvents

The ionic conductivities and dielectric constants of dilute solutions were calculated from the measured conductance and capacitance data, respectively. Electrode polarization produces artificially high capacitance measurements at lower frequencies, but this effect decreases as the frequency increases. At higher frequencies a plateau region for the capacitance was observed between 10^4 and 10^7 Hz for each acetate and ketone solutions. The value of the real part of the dielectric constant calculated from this plateau capacitance is designated as ε_s and is taken as the static dielectric constant.

0.0055 M TbaTf-acetate solutions

As mentioned earlier, choosing a reference conductivity curve is very important for the scaling procedure. In acetate studies, reference curves were constructed for six different reference temperatures (20, 30, 40, 50, 60, 80°C). Each reference curve includes butyl, pentyl, hexyl, octyl and decyl acetate and was fitted using the empirical function $\sigma = A \times exp(\varepsilon_s/t) + B$ (ExpGro1 in Origin 8.1 software). Here, A, B and t are the fitting parameters. Fig 5.1 presents a comparison of the simple Arrhenius plot and compensated Arrhenius plot for 0.0055 M TbaTf in hexyl acetate from 0 to 80°C. The left and right y axes denote scaled temperature dependent ionic conductivities (CAE) and conductivity values for the simple Arrhenius equation,

respectively. The compensated Arrhenius plot was prepared using a reference temperature, T_r= 40°C. Both plots show linear behavior and have correlation coefficients close to unity. However, very different E_a values result from the CAF

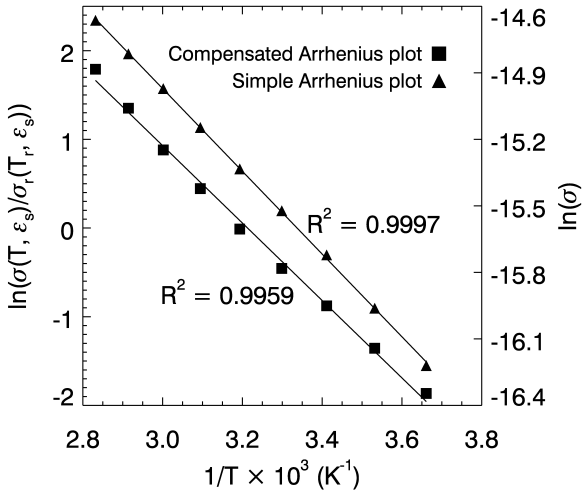

Figure 5.1: Simple Arrhenius and compensated Arrhenius plot for 0.0055 M TbaTf-hexyl acetate

analysis compared to the simple Arrhenius analysis. For example, the activation energy calculated from the conductivity data for 0.0055 M TbaTf-hexyl acetate using the simple Arrhenius plot is 15.5±0.1 kJ mol^{-1}, while the compensated Arrhenius plot yields a value of 36.4±0.9 kJ mol^{-1} at T_r= 40°C. This difference results from the significant disparity in the two slopes, noting the difference in scale in the two ordinate axes. Table 5.1 shows E_a values from CAE plots that result from the conductivity data of 0.0055 M TbaTf-acetates and also E_a values from the simple Arrhenius plots of these data. The CAE E_a values in table 5.1

are closely grouped when an appropriate reference temperature is chosen for each acetate member. The reference temperature is chosen such that the temperature dependent dielectric constant range of the family member is encompassed by the dielectric constant range of the reference conductivity curve.

Table 5.1: Activation energies from compensated Arrhenius and simple Arrhenius plots resulting from conductivity data for 0.0055 M TbaTf-acetates

		CAE E_a (kJ/mol)		simple Arrhenius E_a (kJ/mol)	
0.0055 M TbaTf	T_r			0.0055 M TbaTf	
Solvent	(°C)	Slope	Intercept	Solvent	Slope
pentyl acetate	20	36.3± 0.8	36.3± 0.8	butyl acetate	11.3± 0.1
	30	35.7± 0.8	35.8± 0.8	pentyl acetate	13.1± 0.1
	40	35.7± 0.8	35.9± 0.8	hexyl acetate	15.5± 0.1
hexyl acetate	20	36.1± 0.9	36.1± 0.8	octyl acetate	19.4± 0.1
	30	38± 1.0	38± 1.0	decyl acetate	28± 1.0
	40	36.3± 0.9	36.5± 0.9		
	50	35.9± 0.7	36.0± 0.7		
	60	36.4± 0.7	36.5± 0.7		
octyl acetate	60	39.2± 0.9	39± 1.0		
	80	35.8± 0.9	35± 1.0		

The average activation energy calculated from the CAF is 36.5±0.8 kJ mol^{-1}, while E_a values resulting from simple Arrhenius plots increase systematically

with acetate chain length. Simple Arrhenius behavior is observed over the entire temperature range in each acetate member except decyl acetate, which is the longest chain member studied and has very low conductivities. The conductivity data collected at sub-ambient temperatures for decyl acetate are close to the detection limit of the impedance analyzer and were therefore omitted from the analysis.

Fig 5.2 plots conductivity versus static dielectric constant for 0.0055 M TbaTf-acetate solutions over the temperature range from 0 to 80°C. Five distinct curves are observed, each one consisting of the temperature-dependent data for a particular acetate member.

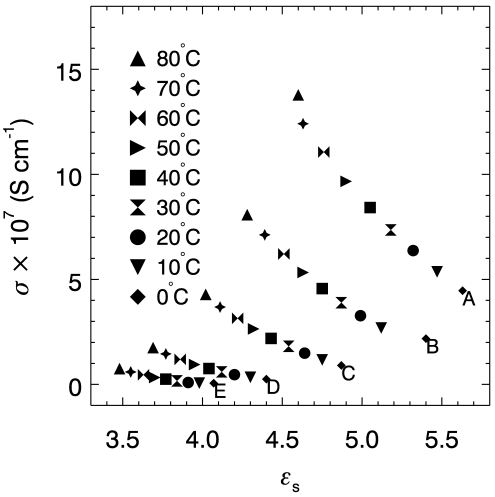

Figure 5.2: Conductivity versus static dielectric constant over the temperature range 0 to 80°C for 0.0055 M TbaTf-acetate solutions of (A) butyl acetate (B) pentyl acetate (C) hexyl acetate (D) octyl acetate (E) decyl acetate over the temperature range 0 to 80°C.

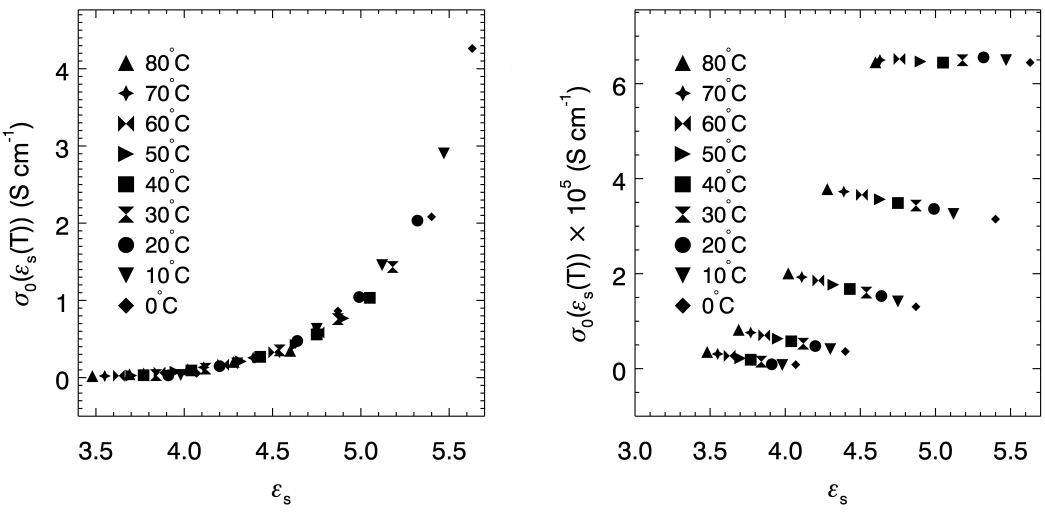

Figure 5.3: Exponential prefactor versus dielectric constant for 0.0055 M TbaTf-acetate solutions using (a) E_a = 36.5 kJ mol^{-1} (b) E_a = 11.3 kJ mol^{-1}

The exponential prefactor is obtained by dividing the temperature-dependent conductivity by exp(-$\frac{E_a}{RT}$). Figure 5.3 graphs the exponential prefactor against the dielectric constant for two different E_a values. All data points lie on a single curve as shown in Fig 5.3(a) when the CAE average E_a value is used. A master curve is still observed when arbitrarily choosing an E_a value in the range from 32 to 42 kJ mol^{-1}. It is interesting to note that the median value of this range (37 kJ mol^{-1}) is close to the average E_a (36.5 kJ mol^{-1}). Fig 5.3(b) was plotted using E_a = 11.3±0.06 kJ mol^{-1} obtained from the simple Arrhenius plot of butyl acetate. It is evident that the data do not form a single master curve. According to these results, the qualitative shape of the graph varies significantly depending on the E_a value.

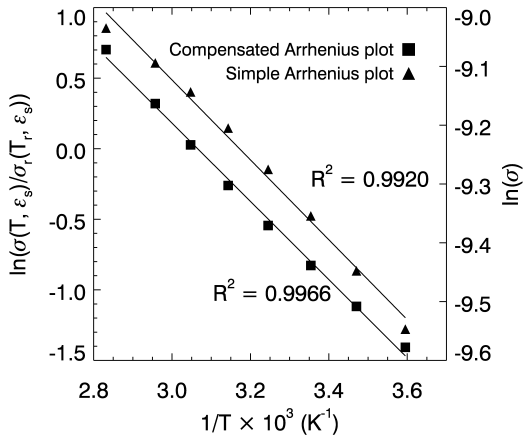

Figure 5.4: Simple Arrhenius and compensated Arrhenius plots (T_r= 55°C) for conductivity data of 0.0055 M TbaTf-2-heptanone over the temperature range 5 to 80°C.

0.0055 M TbaTf-ketone solutions

Figure 5.4 presents both simple Arrhenius and compensated Arrhenius plots for conductivity data of 0.0055 M TbaTf-2 heptanone over the temperature range 5 to 80°C. The CAE plots exhibit linear behavior and the simple Arrhenius plot is approximately linear but does show slight curvature. The resulting CAE and simple Arrhenius E_a values from conductivity data are reported in the Table 5.2. Similar to the acetate data, simple Arrhenius E_a values are lower than those from the CAE. The average CAE activation energy from the data in table 5.2 is 24.1±0.8 kJ mol^{-1} and this value was utilized to determine the conductivity exponential prefactors by dividing the temperature-dependent conductivities by the Boltzmann factor.

Temperature-dependent ionic conductivities are plotted against temperature-

Table 5.2: Activation energies from compensated and simple Arrhenius plots resulting from conductivity data for 0.0055 M TbaTf-ketones.

		CAE E_a(kJ/mol)		simple Arrhenius E_a (kJ/mol)	
0.0055 M TbaTf	T_r			0.0055 M TbaTf	
Solvent	(°C)	Slope	Intercept	Solvent	Slope
2-hexanone	25	23.1± 0.6	23.2± 0.6	2-pentanone	5.05± 0.07
	35	22.7± 0.5	22.8± 0.5	2-hexanone	5.2± 0.1
2-heptanone	25	24± 1	24± 1	2-heptanone	5.6± 0.2
	35	24.1± 0.9	24.3± 0.9	2-octanone	6.3± 0.2
	45	23.4± 0.8	23.6± 0.8	2-nonanone	7.2± 0.2
	55	23.0± 0.5	23.2± 0.6	2-decanone	8.5± 0.2
2-octanone	45	25± 1	25± 1		
	55	25.3± 0.9	25.3± 0.9		
	65	24.8± 0.9	24.7± 0.9		
2-nonanone	80	25.4± 0.8	25.1± 0.9		

dependent dielectric constants in Fig 5.5(a) for the 0.0055 M TbaTf-ketone data. Six distinct curves are observed; one each for the temperature-dependent data of each ketone electrolyte. However, a single master curve is observed when the exponential prefactors are plotted against the static dielectric constant, as shown in Fig 5.5(b). A master curve is only observed for E_a values in the narrow range from 22 to 27 kJ mol^{-1}.

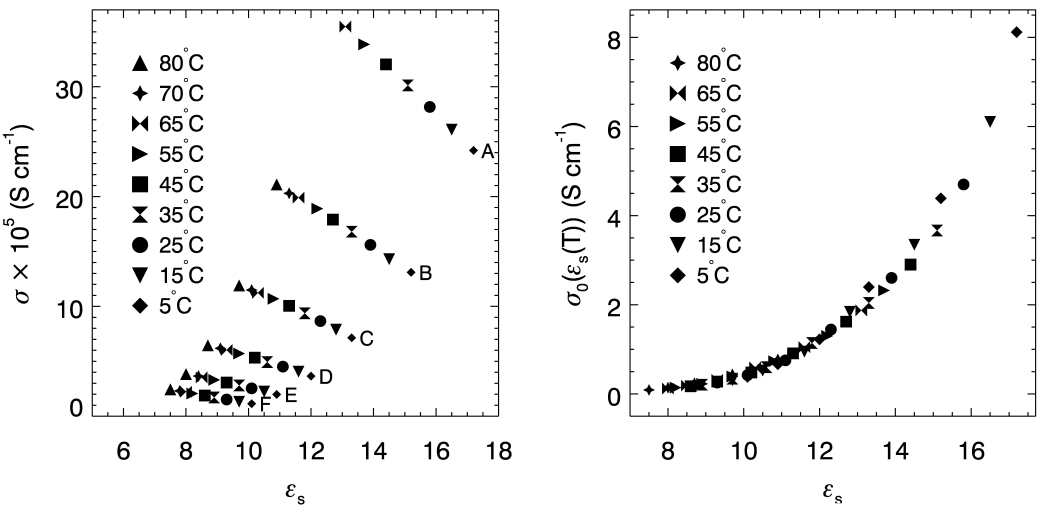

(a) (b)

Figure 5.5: (a) Conductivity versus static dielectric constant over the temperature range 5 to 80°C for 0.0055 M TbaTf-ketone solutions of (A) 2-pentanone (B) 2-hexanone (C) 2-heptanone (D) 2-octanone (E) 2-nonanone (F) 2-decanone. (b) Exponential prefactor versus dielectric constant for 0.0055 M TbaTf-ketone solutions using $E_a = 24.1$ kJ mol^{-1}.

5.3.2 Temperature dependence of self-diffusion coefficients for pure acetate and ketone solvents

In this section, the CAF is used to analyze the self-diffusion coefficients measured with PFG-NMR. As mentioned in the Introduction, temperature-dependent self-diffusion coefficients can be described using a simple Arrhenius-like expression (Ref. Eq. 5.3). Energy of activation values were calculated using a procedure similar to that for temperature dependent conductivity data. The compensated Arrhenius equation for temperature-dependent self-diffusion in Eq. 5.6 was utilized to find

activation energies of pure acetates and pure ketones.

Pure acetate solvents

All measurement were taken for pure acetates (n-butyl, n-pentyl, n-hexyl, n-octyl, and n-decyl) over the temperature range 0 to 80°C. Linear behavior is observed for both simple Arrhenius and compensated Arrhenius plots as shown in Fig 5.6(a) for pure octyl acetate. The E_a value calculated from a simple Arrhenius plot is substantially different from that found from a compensated Arrhenius plot, as was observed with the conductivity data. Based on the compensated Arrhenius plots for hexyl and octyl acetate at five reference temperatures (20, 30, 40, 50, 60°C), an average activation energy of 25.5±0.9 kJ mol^{-1} is obtained. Table 5.3 summarizes E_a values calculated from the CAE slope and intercept for two pure acetates. Table 5.3 also reports activation energies obtained from simple Arrhenius plots.

Figure 5.6(b) plots temperature-dependent self-diffusion coefficients versus dielectric constants for the family of pure acetates. The temperature-dependent diffusion coefficients for each member lie in well-separated curves, similar to the conductivity data depicted in Fig 5.2 and Fig 5.5.

The exponential prefactor, $D_0(\varepsilon_s(T))$, can be determined by dividing the diffusion coefficient by the Boltzmann factor according to Eq. 5.3. Fig 5.7(a) plots the exponential prefactor vs dielectric constant for pure acetates using the average CAE E_a value, while Fig 5.7(b) presents this data using the E_a value obtained from the simple Arrhenius plot for hexyl acetate. Similar to the conductivity data, a master curve is not observed for E_a values obtained from a simple Arrhenius

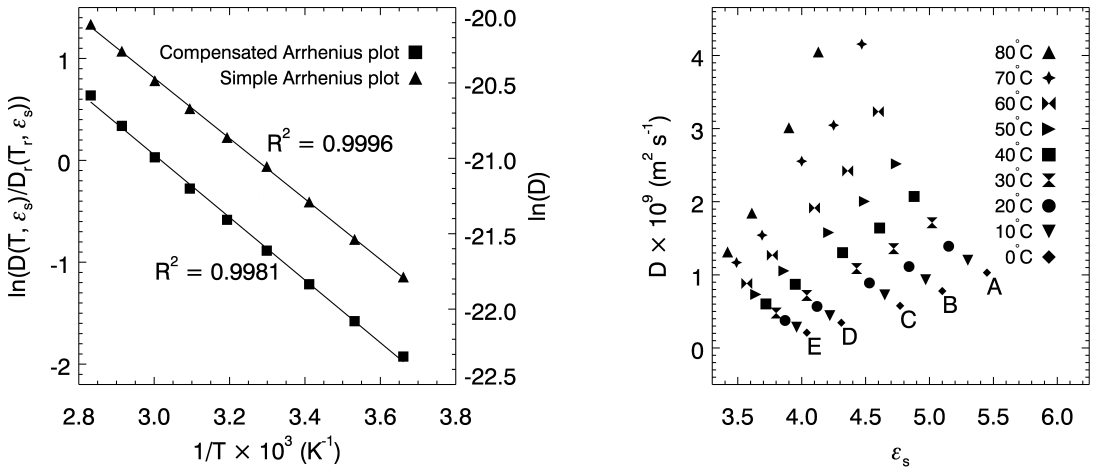

(a) **(b)**

Figure 5.6: (a) Simple Arrhenius and compensated Arrhenius (at T_r= 60°C) plots for pure octyl acetate. (b) Self-diffusion coefficients versus static dielectric constant for (A) butyl acetate (B) pentyl acetate (C) hexyl acetate (D) octyl acetate (E) decyl acetate.

Table 5.3: Activation energies from compensated and simple Arrhenius plots resulting from diffusion data for pure acetates

		CAE E_a(kJ/mol)		simple Arrhenius E_a (kJ/mol)	
Solvent	T_r(°C)	Slope	Intercept	Solvent	Slope
hexyl acetate	20	26± 1	26± 1	butyl acetate	15± 1
	30	25± 1	26± 1	pentyl acetate	16.0± 0.8
	40	25± 1	25± 1	hexyl acetate	16.4± 0.6
	50	26± 1	26± 1	octyl acetate	16.7± 0.1
octyl acetate	50	24.9± 0.5	25.0± 0.5	decyl acetate	18.4± 0.3
	60	25.6± 0.4	25.7± 0.4		

plot. A master curve does result for E_a values within the narrow range from 24 to 27 kJ mol^{-1}. The average activation energy from the CAF analysis is equal to the median value of this range. The diffusion master curve exhibits more scatter in the data than the analogous plot for conductivity. It is likely that at least some of the scatter is due to convection effects. Pronounced thermal gradients can exist in the NMR sample when the sample temperature significantly deviates from room temperature. These thermal gradients produce artificially high values for the diffusion coefficients. Convection related error was minimized in this study by focusing on the longer chain acetates that are less susceptible to this phenomenon, and also by constricting the sample volume in the NMR tube. However, it is difficult to completely eliminate convection effects and consequently some error is introduced into the diffusion data at higher temperatures.

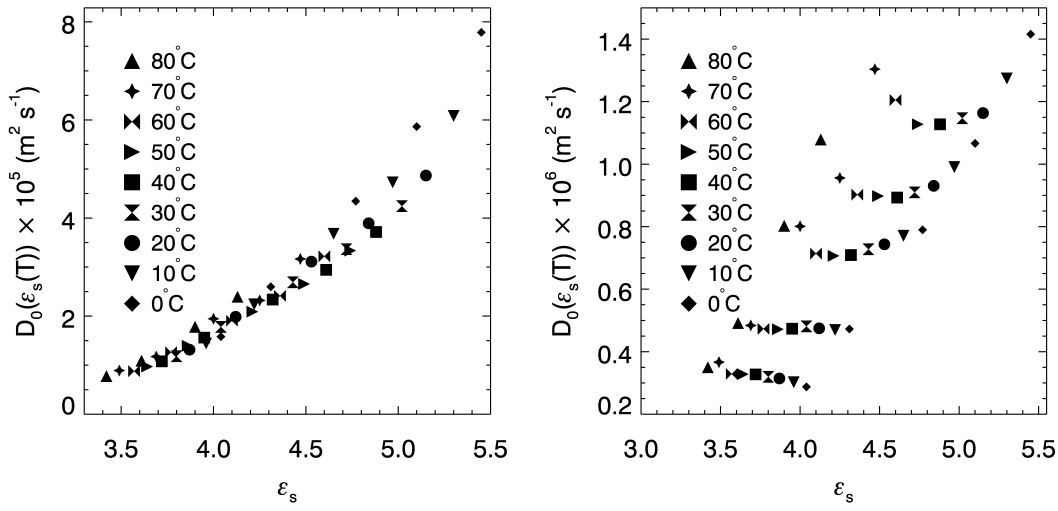

(a) **(b)**

Figure 5.7: Exponential prefactor versus dielectric constant for the diffusion data of pure acetates using (a) $E_a = 25.5$ kJ mol^{-1} (b) $E_a = 16.4$ kJ mol^{-1}

Pure ketone solvents

The simple Arrhenius and compensated Arrhenius plots for the diffusion data of pure 2-hexanone are shown in Fig 5.8. A high degree of linearity is observed for both graphs, as indicated by the value of the correlation coefficients. The simple Arrhenius E_a value calculated for the 2-hexanone data is 15.2 kJ mol^{-1}, while those calculated from the slope and intercept using the CAE are 23.7 and 23.8 kJ mol^{-1}, respectively. The E_a value obtained from the simple Arrhenius plot is lower than the corresponding CAE activation energies, which is a trend that has been observed in other systems [14–17].

Table 5.4 summarizes compensated Arrhenius E_a values at five different reference

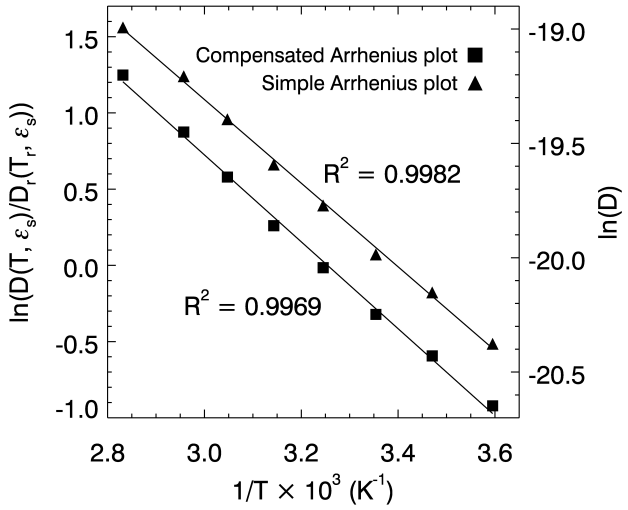

Figure 5.8: Simple Arrhenius and compensated Arrhenius (at T_r= 35°C) plots for self-diffusion coefficient data of pure 2-hexanone over the temperature range 5 to 80°C.

temperatures (25, 35, 45, 55, 65°C) for pure 2-hexanone, 2-heptanone, and 2-nonanone. The average CAE activation energy from the data in table 5.4 is 23.9±0.8 kJ mol^{-1}. Table 5.4 also lists the simple Arrhenius E_a values for each ketone. Fig 5.9(a) plots diffusion coefficients versus static dielectric constant for pure ketones. Six well-separated curves are observed; one each for the temperature dependent data of each ketone. The exponential prefactors, D_0 are calculated by dividing the temperature dependent diffusion coefficients by the Boltzmann factor, exp(-$\frac{E_a}{RT}$) (5.3). The plot of exponential prefactor versus dielectric constant yields a single master curve in Fig 5.9(b). This single master curve can be observed only for a narrow range of E_a values (22.5-25.5 kJ mol^{-1}).

Table 5.4: Activation energies from compensated and simple Arrhenius plots resulting from diffusion data for pure ketones.

		CAE E_a(kJ/mol)		simple Arrhenius E_a (kJ/mol)	
Solvent	T_r(°C)	Slope	Intercept	Solvent	Slope
2-hexanone	25	23.8± 0.5	23.9± 0.5	2-hexanone	15.2± 0.2
	35	23.7± 0.5	23.8± 0.5	2-heptanone	15.2± 0.6
2-heptanone	25	23.8± 0.9	24.0± 0.8	2-octanone	16.1± 0.7
	35	23.8± 0.9	24.0± 0.9	2-nonanone	15.1± 0.1
	45	23.8± 0.9	24.0± 0.9	2-decanone	15.7± 0.2
	55	23.9± 0.9	24.0± 0.9		
	65	23.9± 0.9	23.9± 0.9		
2-nonanone	65	24.0± 0.7	23.9± 0.7		

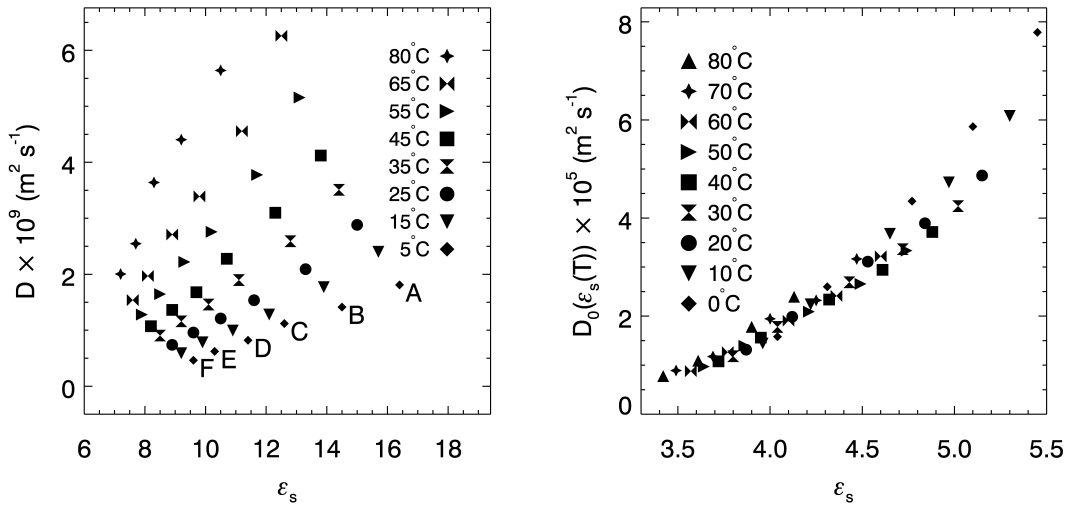

(a) **(b)**

Figure 5.9: (a) Self-diffusion coefficients versus static dielectric constant over the temperature range 5 to 80°C for (A) 2-pentanone (B) 2-hexanone (C) 2-heptanone (D) 2-octanone (E) 2-nonanone (F) 2-decanone. (b) Exponential prefactor versus dielectric constant for the diffusion data of pure ketones using $E_a = 23.9$ kJ mol^{-1}.

5.4 Conclusions

In this study, we extend the scope of the CAF by examining the families of n-acetates and 2-ketones, which are aprotic solvents. Ketones are structurally very similar to the acetates, but have much higher dielectric constants. A comparison between acetate and ketone conductivity and diffusion data is necessary to better understand the role of the static dielectric constant in controlling mass and charge transport in liquids. Here, temperature-dependent conductivities are reported for 0.0055 M TbaTf-acetate electrolytes and 0.0055 M TbaTf-ketone electrolytes, respectively.

Also, self-diffusion coefficients are presented for pure acetates and pure ketone liquids. Our results indicate that both temperature-dependent ionic conductivity and diffusion coefficient data for acetates and ketones obey the compensated Arrhenius formalism. The average activation energy from diffusion data of pure acetates is 25.5 kJ mol^{-1}, while that obtained from conductivity data for 0.0055 M TbaTf acetates is 36.5 kJ mol^{-1} [18]. The difference between these two activation energies (approximately 11 kJ mol^{-1}) is significant. Similarly, the activation energy from diffusion data of pure ketones is 23.9 kJ mol^{-1} and that calculated from conductivity data of 0.0055 M TbaTf-ketone solutions is 24.1 kJ mol^{-1} [20]. The small difference between E_a values of conductivity and diffusion data is negligible since it is well within the error.

Figure 5.10 compares temperature-dependent conductivities between 0.0055 M TbaTf-ketone and acetate electrolytes. Both ketone and acetate have conductivities that increase with increasing with temperature and decreasing alkyl chain length as expected. However, ketone conductivities are significantly higher than those for the acetates. This conductivity difference is explained by examining both contributions to the conductivity: the exponential prefactor σ_0 and the Boltzmann factor $\exp(-\frac{E_a}{RT})$. Fig 5.11(b) shows that the conductivity prefactors are comparable between the acetates and ketones. Hence, the acetate conductivity data are orders of magnitude lower than those for the ketones because the acetates have a much higher E_a value (36.5 kJ mol^{-1}) compared to the ketones (24.1 kJ mol^{-1}). In contrast to the conductivity data, diffusion coefficients are comparable between pure acetates and ketones for similar temperatures and chain lengths.

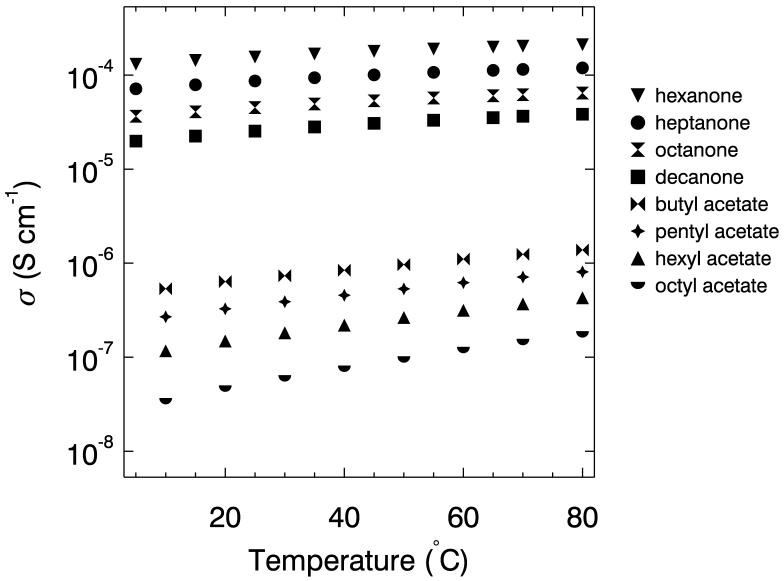

Figure 5.10: Conductivity versus temperature for 0.0055 M TbaTf-2-ketone and 0.0055 M-TbaTf-n-acetate solutions over the temperature range 5 to 80°C.

Figure 5.11(a) shows that this is not unexpected considering that both diffusion prefactors and E_a values between the acetates and ketones are close in value to each other. The prefactors are similar in magnitude between acetates and ketones in both Fig 5.11(a) and Fig 5.11(b), and the primary difference between these two solvent families is that the acetate master curve is horizontally shifted from that of the ketones. This shift results from the large difference in permittivity between acetates and ketones that is due primarily to the substantial difference in dipole moment for these two solvent families. Additionally, the dielectric constant changes much less with temperature for the acetates and therefore the prefactors increase more sharply for the acetates compared to the ketones in Fig 5.11(a) and (b).

An intriguing question arises from the data presented in Fig 5.11. The activa-

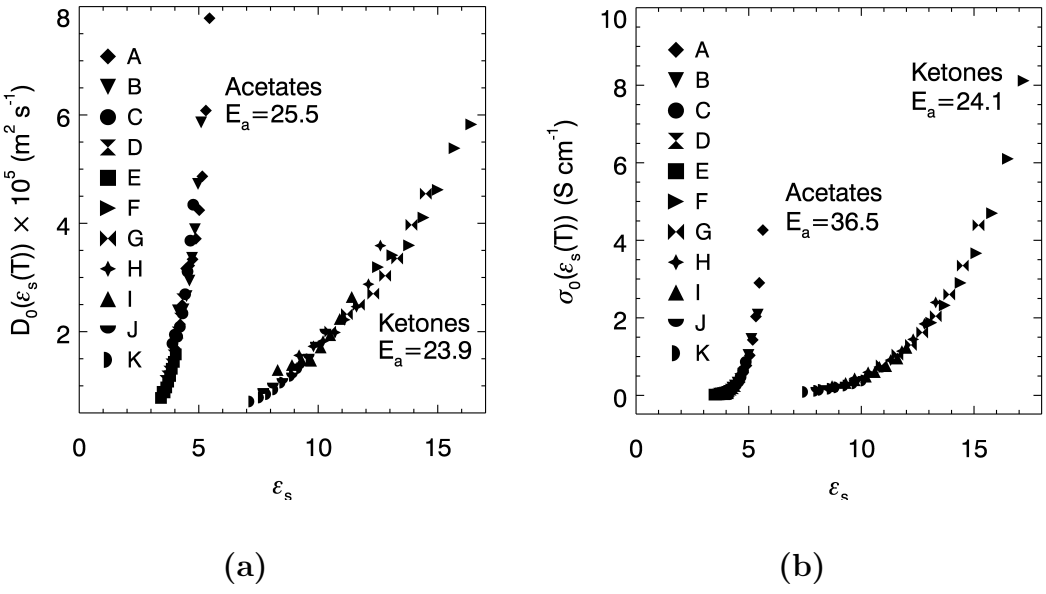

Figure 5.11: (a) Exponential prefactor versus dielectric constant for the diffusion data of (left) pure acetates, (right) pure ketones (b) Exponential prefactor versus dielectric constant for the ionic conductivity data of (left) 0.0055 M TbaTf-acetates, (right) 0.0055 M TbaTf-ketones. The letters designate the various compounds as follows: (A) butyl acetate (B) pentyl acetate (C) hexyl acetate (D) octyl acetate (E) decyl acetate (F) 2-pentanone (G) 2-hexanone (H) 2-heptanone (I) 2-octanone (J) 2-nonanone (K) 2-decanone. The units of E_a are kJ/mol.

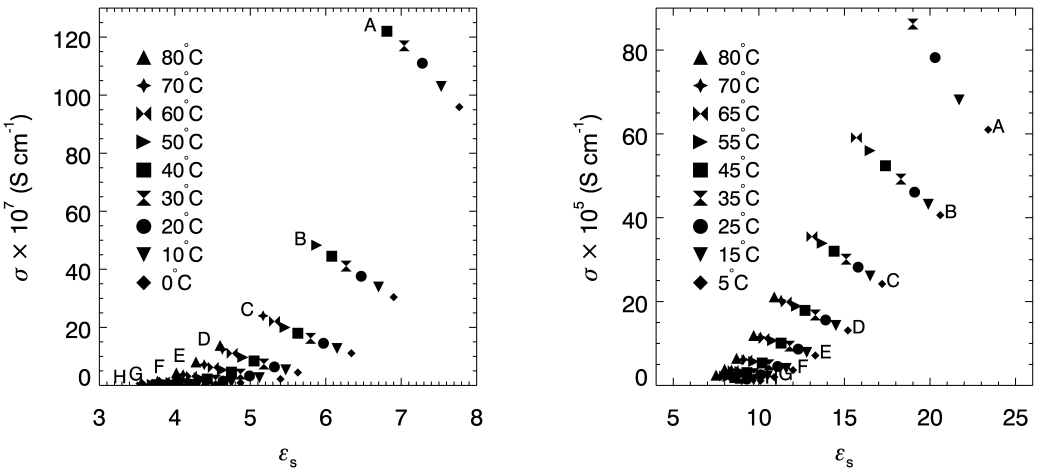

(a) **(b)**

Figure 5.12: (a) Conductivity versus static dielectric constant over the temperature range 0 to 80°C for 0.0055 M TbaTf-acetate solutions of (A) methyl acetate (B) ethyl acetate (C) propyl acetate (D) butyl acetate (E) pentyl acetate (F) hexyl acetate (G) octyl acetate (H) decyl acetate.(b) Conductivity versus static dielectric constant over the temperature range 5 to 80°C for 0.0055 M TbaTf-ketone solutions of (A) 2-acetone (B) 2-butanone(c) 2-pentanone (D) 2-hexanone (E) 2-heptanone (F) 2-octanone (G) 2-nonanone (H) 2-decanone.

tion energy for diffusion in pure ketones is approximately equivalent to that for conductivity in dilute ketone solutions. These results could have been anticipated, but why then would the addition of a small amount of salt to an acetate result in an E_a increase of more than 10 kJ mol^{-1} from the diffusion value to the conductivity value? Since acetate permittivities are much lower than those for ketones, it is expected that ion-solvent and ion-ion interactions will be much stronger in the acetates. It is unclear why change in the intermolecular interactions could result in a 11 kJ mol^{-1} increase in E_a value.

The conductivity and diffusion data presented here for both acetates and ketones are described very well with the CAF. However, acetates and ketones with shorter alkyl chains were not included in the analysis because their transport behavior is not entirely consistent with that for the long chain members. Fig 5.12(a) plots conductivity versus dielectric constant for 0.0055 M TbaTf-acetates. This graph is similar to Fig 5.2 except that data are included for methyl, ethyl, and propyl acetate. The conductivities for the three shortest chain members are significantly higher than those for the longer members. If data for methyl, ethyl, and propyl acetate are included in the reference curve, the conductivity CAE plots for ethyl and propyl acetate result in E_a values around 28 kJ mol^{-1}. This activation energy is well below the average E_a value calculated for the longer members (36.5 kJ mol^{-1}). Furthermore, CAE plots for each of the longer members give E_a values that are close to the average value of 36.5 kJ mol^{-1} (see table 5.1). The CAF can only completely describe the acetate data if this family is subdivided into two groups that have different E_a values. The lower activation energy for methyl, ethyl, and propyl

acetate helps explain the high conductivity values observed for these members in Fig 5.12(a).

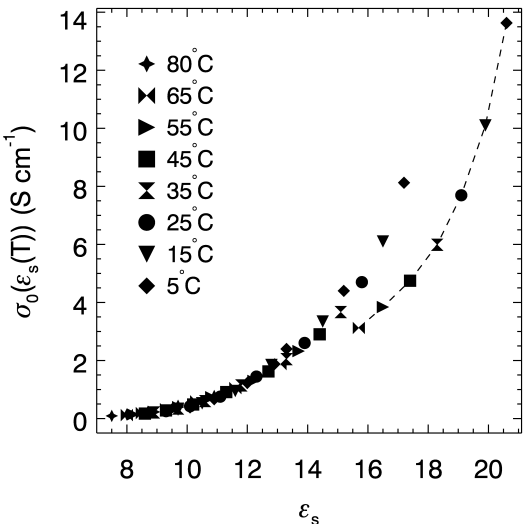

Figure 5.13: Conductivity exponential prefactor versus dielectric constant for 0.0055 M TbaTf-ketone solutions including 2-butanone data (dashed line).

Similar to acetates, short carbon chain dilute ketones display surprisingly high ionic conductivities as shown in Fig 5.12(b). These data show that the average E_a value is lower for the short chain members (19.2 kJ mol^{-1}) than that of long chain members (24.1 kJ mol^{-1}) similar to acetate data. Petrowsky *et al.* has reported the ionic conductivities of 0.0055 M solutions including short carbon ketones like acetone, 2-butanone, over the temperature range from -15 to 80°C [15]. They reveal that average E_a is about 16 kJ mol^{-1} and this value agrees with there results.

Methyl acetate, ethyl acetate, propyl acetate, acetone, and 2-butanone are

not the only short chain members of a solvent family to show deviations from the CAF. Both dielectric relaxation data for acetonitrile [17] and diffusion data for methanol [14] have been shown to exhibit transport behavior that is different from their long chain family members. Previous work has shown that the CAF can be applied to dielectric relaxation data for pure acetates [17]. However, data for methyl and propyl acetate were included in the previous calculation of the activation energy. Therefore, it is possible that the reported E_a value is somewhat different from an activation energy calculated using only long chain acetates.

Figure 5.13 shows the same data as Fig 5.5(b) only with 2-butanone data included (shifted curve with dashed line). The exponential prefactors for short chain members show the same qualitative dielectric constant dependence as that for long chain members, but these data are offset to the right of the master curve. The master curve demonstrates this unique behavior for both acetate and ketone systems when short chain members are included. It is quite possible that in order for the CAF to completely describe a particular solvent family, this family must be subdivided into two groups: short alkyl chain members with lower E_a values and long alkyl chain members with higher E_a values.

References

[1] D. Fauteux, A. Massucco, M. McLin, M. V. Buren, and J. Shi, Electrochim. Acta **40**(13-14), 2185 (1995).

[2] K. Xu, Chem. Rev. **104**(13-14), 4303 (2004).

[3] J. R. MacCallum and C. A. Vincent, *Polymer Electrolyte Reviews 1* (Elsevier Applied Science Publishers Ltd., 1987), 1st ed.

[4] J. R. MacCallum and C. A. Vincent, *Polymer Electrolyte Reviews 2* (Elsevier Applied Science Publishers Ltd., 1989), 1st ed.

[5] J. Bendler, J. J. Fontanella, and M. F. Shlesinger, Phys. Rev. Lett. **87**(19), 195503 (2001).

[6] S. Arrhenius, Z. Phys. Chem. **4**(E2), 226 (1889).

[7] J. Fontanella, M. Wintersgill, M. Smith, J. Semancik, and C. Andeen, J. Appl. Phys **60**(8), 2665 (1986).

[8] P. G. Bruce, *Solid State Electrochemistry* (Cambridge University Press, 1995), 1st ed.

[9] M. L. Williams, R. F. Landel, and J. Ferry, J. Am. Chem. Soc. **77**, 3701 (1955).

[10] H. Vogel, Physik Z. **22**, 645 (1921).

[11] G. S. Fulcher, J. Am. Ceram. Soc. **8**(E2), 339 (1925).

[12] G. Tammann and W. Hesse, Z. Anorg. Allg. Chem. **156**(E2), 245 (1926).

[13] J. Bockris and A. Reddy, *Modern Electrochemistry*, vol. 1 (Plenum press, 1998), 2nd ed.

[14] M. Petrowsky and R. Frech, J. Phys. Chem. B **114**(26), 8600 (2010).

[15] M. Petrowsky and R. Frech, J. Phys. Chem. B **113**(17), 5996 (2009).

[16] M. Petrowsky and R. Frech, Electrochim. Acta **55**(17), 1285 (2010).

[17] M. Petrowsky and R. Frech, J. Phys. Chem. B **113**(17), 16118 (2009).

[18] D. N. Bopege, M. Petrowsky, A. M. Fleshman, R. Frech, and M. B. Johnson, J. Phys. Chem. B **116**(1), 71 (2012).

[19] A. M. Fleshman, M. Petrowsky, J. D. Jernigen, R. Bokalawela, M. B. Johnson, and R. Frech, Electrochim. Acta **57**(0), 147 (2011).

[20] D. N. Bopege, M. Petrowsky, R. Frech, and M. B. Johnson (2012), to be submitted.

[21] M. J. Williamson, H. V. S. A. Hubbard, and I. M. Ward, Polymer **40**(26), 7177 (1999).

[22] N. Boden, S. Leng, and I. Ward, Solid State Ionics **45**(3-4), 261 (1999).

[23] M. Williamson, J. Southall, H. S. A. Hubbard, S. Johnston, G. Davies, and I. Ward, Electrochim. Acta **43**(10-11), 1415 (1998).

[24] X. X. Zhu and P. M. Macdonald, Macromolecules **25**(17), 4345 (1992).

[25] K. Hayamizu, Y. Aihara, S. Arai, and G. Martinez, J. Phys. Chem. B **103**(3), 519 (1999).

[26] A. Johansson, A. Gogoll, and J. Tegenfeldt, Polymer **37**(8), 1387 (1996).

[27] Y. Aihara, T. Bando, H. Nakagawa, H. Yoshida, K. Hayamizu, E. Akiba, and W. S. Price, J. Electrochem. Soc. **151**(1), A119 (2004).

[28] K. Hayamizu, A. Matsuo, and J. Arai, J. Electrochem. Soc. **156**(9), A744 (2009).

[29] M. Holz, S. R. Heil, and A. Sacco, Phys. Chem. Phys. **2**(20), 4740 (2000).

[30] A. Ferry, G. Ordd, and P. Jacobsson, Electrochim. Acta **43**(10-11), 1471 (1998).

[31] R. Frech and W. Huang, J. Sol. Chem. **23**, 469 (1994).

[32] M. Petrowsky and R. Frech, J. Phys. Chem. B **112**(28), 8285 (2008).

[33] *Agilent 16452A Liquid Test Fixture Operation and Service Manual* (2000).

[34] E. O. Stejskal and J. Tanner, J. Chem. Phys. **42**(8), 288 (1965).

[35] W. S. Price, Concepts Magn. Reson. **9**(E2), 299 (1997).

[36] W. S. Price, Concepts Magn. Reson. **10**(4), 197 (1998).

Chapter 6

Ion Transport and Infrared Spectroscopic Studies of Lithium Triflate in Aprotic Solvents

6.1 Introduction

Study of the organic liquid electrolytes containing lithium salts in aprotic solvents is of great interest due to their utilization in electrochemical devices. Carbonate-based solvents such as ethyl methyl carbonate and ethylene carbonate have been used in conventional organic electrolytes. Recently, ester-based, ketone-based and ether-based solvents have been increasingly used in Li-ion batteries. Battery electrolytes can be made from these solvents alone or by mixing with other solvents [1, 2]. Understanding ion transport and ionic species present in these electrolytes is a necessary step in enhancing electrolyte performance. Recently we investigated the temperature-dependent ion conductivities of 0.0055 M tetrabutylammonium triflate (TbaTf) acetate and ketone solutions, as well as self-diffusion coefficients in pure ketones and acetates. Data from both systems were interpreted using the compensated Arrhenius formalism (CAF) [3, 4]. This formalism was developed to explain the non-Arrhenius behavior often observed in the temperature dependence of ionic conductivity. As we mentioned in chapter 5, the CAF postulates that the non-Arrhenius behavior is due to the temperature dependence of exponential prefactor, σ_0, in the usual Arrhenius expression. Because the conductivity also depends on the dielectric constant, which also depends on the temperature, the

compensated Arrhenius expression is re-written as:

$$\sigma(T, \varepsilon_s) = \sigma_0(\varepsilon_s(T))\mathrm{e}^{-\frac{E_a}{RT}} \tag{6.1}$$

where, σ denotes the ionic conductivity, σ_0 is the temperature independent prefactor, T is the temperature, and E_a is the activation energy. A scaling procedure (described in detail in chapter 5) is then used to cancel out the exponential prefactor and allow the calculation of the activation energy E_a.

Ketones have high dielectric constants due to the presence of large permanent dipole moments(about 3.0 Debye). Acetates are low dielectric constant solvents and exhibit low dipole moments(about 1.7-1.9 D) compared to ketones [5]. The electronic charge in the carbonyl group is redistributed due to the extra oxygen atom between carbonyl group and the CH_2 of n-acetate, hence lowering the net dipole moment of the acetate system. With the addition of salt, it is possible to have dipole-dipole and dipole-ion interactions in the electrolytic solution.

In this chapter, the CAF is applied to temperature-dependent conductivities of concentrated LiTf-acetate and ketone solutions; these electrolytes are much more relevant to battery technology. The LiTf salt is highly associated in acetate and ketone solutions compared to the TbaTf-solvent systems we studied earlier. To date, the CAF has not been tested in electrolytes that have strong ion-ion and ion-solvent interactions as in the concentrated LiTf-acetate and ketone solutions examined here. Although these results provided valuable information regarding the activation energies, dielectric constants, ionic conductivities, and the role of heteroatoms, it is particularly important to understand the ionic association in these systems both

qualitatively and quantitatively, because the degree of association greatly impacts the ionic conductivity.

During the last few decades, research groups have studied ionic association in polymer and liquid electrolytes using a variety of spectroscopically sensitive salts [6–13]. LiTf was largely used because it has high solubility in most organic solvents and polymers. Solutions of LiTf in both acetates and ketones show strong ion-solvent and ion-ion interactions. Ion-ion interactions lead to the observations of "free" ions, ion pairs, triplets, and higher aggregates in these solutions [6, 9, 14, 15]. If the solvent dielectric constant is sufficiently low, the ions exhibit a complex behavior due to the formation of clusters [7, 16]. Vibrational spectroscopy is one of the most powerful tools used to probe ionic association of polymer and liquid electrolytes [12, 15, 17–20].

The objective of the present study is to investigate the temperature dependence and concentration dependence of ionic conductivities for concentrated solutions of LiTf in acetates and ketones. More importantly, the formation of multiple ionically-associated species at high concentrations provides a stringent test of the CAF formalism, which has been tested in dilute solutions of TbaTf. The bulky cation of TbaTf minimizes ionic association to the point where it is not spectroscopically observed. Here, the SO_3 symmetric stretching and CF_3 symmetric deformation modes of the triflate ion are used to examine ionic association in LiTf-acetate and ketone solutions over the temperature range 5 to 75°C using FTIR spectroscopy. Additionally, the carbonyl stretching mode of the solvent is studied to better understand the lithium-solvent interactions. In order to gain insight into the

aggregate formation, equilibrium constants were calculated for both concentrated acetate and ketone solutions. In parallel to these studies, self-diffusion coefficients were examined using pulsed field gradient NMR.

6.2 Experimental Methods

Acetate and ketone solvents were obtained from either Aldrich or Alfa Aesar. Lithium trifluoromethanesulfonate (99.5%) was purchased from Aldrich and used as received. The composition of all samples are reported as molal concentration, m, i.e. the number of moles of salt per kg of solvent (mol kg^{-1}). All samples (0.3 and 0.8 m) were prepared by dissolving a weighed amount of LiTf in acetate or ketone solvents. Each sample was stirred for at least 24 hours in a glove box ($\leq$ 1 ppm H_2O and approximate temperature 25°C) before taking measurements.

The conductivities and dielectric constants were calculated using the same experimental process as we explained in the section 5.2.2 (chapter 5) for both concentrated LiTf-acetate and ketone solutions. Infrared spectra were collected under a flowing dry nitrogen atmosphere over the temperature range 5 to 75°C using a Bruker IFS66V FTIR spectrometer for both salt concentrations (0.3 and 0.8 m). The samples were sealed in a liquid cell (model-TFC-M25-3) with sodium chloride windows (25× 2 mm dimensions) that were separated by either 0.025 and 0.05 mm path length teflon spacers. Sodium chloride windows were utilized to avoid the fringing effect of the sample spectrum. All spectra resulted from 64 scans and were collected over the spectral range 400-4000 cm^{-1} using 1 cm^{-1}

spectral resolution. The samples equilibrated for 20-30 minutes prior to recording a spectrum at each temperature. A Laird Technologies thermoelectric module (TEM) was used to extract heat for temperatures less than 25°C. The current is supplied using a DC power supply(HP 6002A) to maintain the temperature gradient between the hot and cold sides. The sample temperature was regulated using a temperature controller and Neslab CFT-33 refregirated recirculater and also measured with a resistance temperature detector(RTD). The sample temperature was monitored using an Omega temperature controller(model-CN9000A)

For the equilibrium constant analysis, IR spectra were collected at room temperature. The LiTf-hexyl acetate samples filled the semi-permanent KBr rectangular liquid cell equipped with 0.1 mm teflon spacer and nine spectra were recorded for each concentration (0.3, 0.5, 0.8 m). For LiTf-heptanone solution, 0.3, 0.5, 0.7 and 1.0 m concentration samples were prepared. Each sample ($\sim$ 1-3 drops of LiTf-heptanone solution) was sandwiched between two NaCl windows and twelve IR spectra were collected. Each spectrum was curve-fitted using OriginPro software (OriginLab Origin 8.5). A Varian VNMRS 400 MHz NMR spectrometer operated with an Auto-X-dual broad band probe(5 mm) was utilized to measure self-diffusion coefficients. The Larmor frequency for ^{7}Li and ^{19}F were 376.22 and 154.40 MHz, respectively.

6.3 Results and Discussion

6.3.1 Ionic conductivities of LiTf in acetate and ketone-based electrolytes

Our present study reports the ionic conductivities and dielectric constants of LiTf in acetate and ketone solvents as functions of concentration and temperature. Here, ionic conductivities and dielectric constants were measured for 0.30 m and 0.80 m LiTf in five acetates (n-butyl, n-pentyl, n-hexyl, n-octyl, n-decyl acetates) in the temperature range of 5 to 85°C. The dependence of ionic conductivity on the static dielectric constant of the solutions is illustrated in Fig. 6.1 for both 0.3 m and 0.8 m LiTf-acetates. This figure shows that both conductivity and dielectric constant increase with increasing salt concentration. The ionic conductivities of the 0.8 m solution are approximately one order of magnitude higher than that of the 0.3 m solution. The data falls on well-separated curves for each family member at both concentrations.

In the Introduction, the variation of molar conductivity with concentration for low dielectric constant liquid electrolytes has been discussed. The three different regions (I, II, III) represent different qualitative behavior of the molar conductivity with respect to the concentration [21]. In this chapter, we present measured conductivities for two different concentrations of LiTf-acetate solutions and examine the molar conductivities using $\lambda = \sigma/c$. We noticed that the molar conductivity increases with the concentration. This behavior may be due to increased ion mobility.

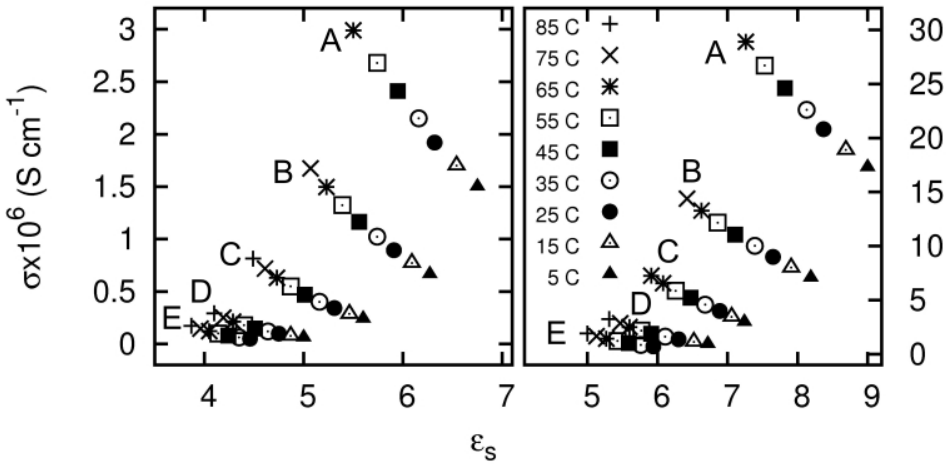

Figure 6.1: Conductivity versus static dielectric constant for solutions of LiTf in (A) butyl acetate (B) pentyl acetate (C) hexyl acetate (D) octyl acetate (E) decyl acetate over the temperature range 5 to 85°C for 0.3 m LiTf (left hand figure) and 0.8 m LiTf (right hand figure). Note the diffrence in the ordinate scales.

The compensated Arrhenius equation (previously described in detail) was applied to the conductivity data at both 0.3 and 0.8 molal concentrations [22, 23]. A high degree of linearity was observed in both simple Arrhenius and the compensated Arrhenius plots for 0.3 and 0.8 m concentrations. As an example, Fig. 6.2 demonstrates the simple Arrhenius and compensated Arrhenius plots for 0.3 mol kg^{-1} concentration.

These data indicate that the compensated Arrhenius formalism can be applied to temperature dependent ionic conductivities in concentrated solutions with ionic association as well as in dilute solution. The activation energy was obtained from slopes and intercepts of both CAE and simple Arrhenius plots [3, 22–25]. Table 6.1 summarizes the activation energies of 0.3 m LiTf-acetate solutions. These

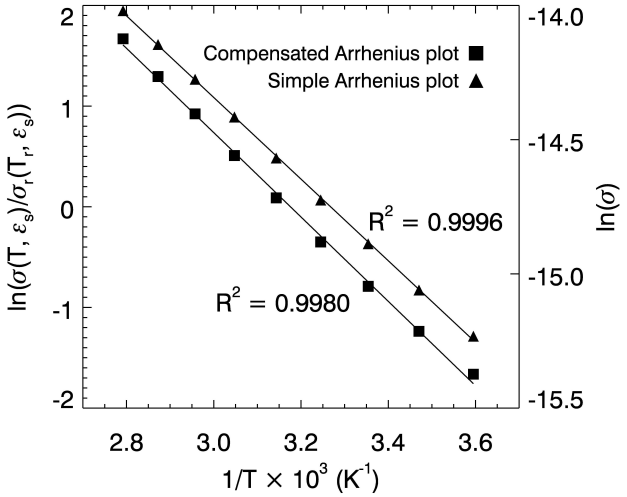

Figure 6.2: Simple Arrhenius and compensated Arrhenius plot for 0.3 mol kg^{-1} LiTf-acetate solutions

values were calculated for pentyl and hexyl acetates at four different reference temperatures (25, 35, 45, 55°C). The average activation energy calculated from the CAF is 35.4±0.6 kJ mol^{-1}, while E_a values resulting from simple Arrhenius plots increase systematically with acetate chain length.

Following a similar procedure, the average activation energies were found for 0.8 m LiTf-acetates and also reported in Table 6.2. The calculated average activation energy was 32.7 ± 1.0 kJ mol^{-1}, which is smaller than that observed for 0.3 m acetates (35.4 kJ mol^{-1}).

In order to more closely examine ion transport in acetate and ketone electrolytes, ionic conductivities and dielectric constants of 0.3 m LiTf-ketone solutions were collected over the temperature range 5 to 85°C. These solutions were made by using

Table 6.1: Activation energies from compensated Arrhenius and simple Arrhenius plots resulting from conductivity data for 0.3 m LiTf-acetates

		CAE E_a (kJ/mol)		simple Arrhenius E_a (kJ/mol)	
0.3 m LiTf	T_r			0.3 m LiTf	
Solvent	(°C)	Slope	Intercept	Solvent	Slope
pentyl acetate	25	35.8± 0.6	35.8± 0.6	butyl acetate	9.0± 0.1
	35	35.8 ± 0.6	35.9± 0.6	pentyl acetate	10.6± 0.1
hexyl acetate	25	34.7± 0.6	35.0± 0.5	hexyl acetate	12.6± 0.1
	35	35.0± 0.7	35.4± 0.7	octyl acetate	16.0± 0.1
	45	34.8± 0.6	35.2± 0.6	decyl acetate	18.6± 0.1
	55	35.4± 0.5	35.8± 0.5		

five ketones (2-hexanone, 2-heptanone, 2-octanone, 2-nonanone,and 2-decanone). The CAE plot exhibits linear behavior and the simple Arrhenius plot is approximately linear but does show slight curvature for the 0.3 m LiTf-octanone systems as shown in Fig. 6.3. We reported this non linear behavior of simple Arrhenius plot for 0.0055 M TbaTf-2-ketones in chapter 5 [4]. Non-Arrhenius behavior is expected due to the temperature dependence of the dielectric constant contained in the exponential prefactor.

Figure 6.4 shows the conductivity versus static dielectric constant of these solutions. This graph consists of well separated curves similar to Fig. 6.1 and shows higher conductivity for lower chain length ketone electrolytes. Calculated activation energies from Compensated Arrhenius plot for LiTf in four ketones

Table 6.2: Activation energies from compensated Arrhenius and simple Arrhenius plots resulting from conductivity data for 0.8 mol kg^{-1} LiTf-acetates

		CAE E_a (kJ/mol)		simple Arrhenius E_a (kJ/mol)	
0.8 m LiTf	T_r			0.8 m LiTf	
Solvent	(°C)	Slope	Intercept	Solvent	Slope
pentyl acetate	25	33.7± 0.7	33.7± 0.7	butyl acetate	6.69± 0.08
	35	32.2± 0.7	32.3± 0.7	pentyl acetate	8.17± 0.02
hexyl acetate	35	32.8± 1.4	33.3± 1.4	hexyl acetate	10.30± 0.03
	45	33.0± 1.3	33.4 ± 1.3	octyl acetate	12.67± 0.04
	55	32.1± 1.1	32.4± 1.1	decyl acetate	14.55± 0.14
	65	31.6± 0.9	31.7± 1.0		

(heptanone, octanone, nonanone, decanone) are listed in Table 6.3. The resulting average activation energy was 26.1 ± 0.6 kJ mol^{-1}.

To determine the exponential prefactors of acetate and ketone solutions, temperature dependent ionic conductivities of each family member were divided by the Boltzmann factor, $\exp(-\frac{E_a}{RT})$. Fig. 6.5 presents the comparison of exponential factor versus dielectric constant for 0.3 and 0.8 m LiTf-acetates, and 0.3 m LiTf-ketone. This figure shows that all set of electrolyte data lie on a single master curve. This behavior also seen in other system studied in the chapter 5. These results give supporting evidence to the validity of the two fundamental assumptions of the compensated Arrhenius formalism. Further, it is clear that we need to use the CAE

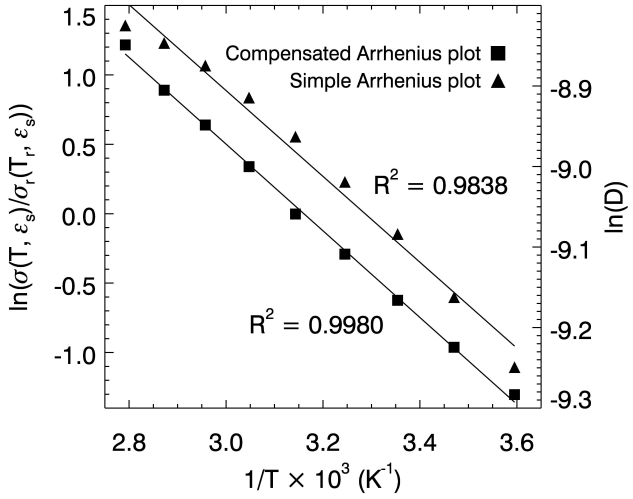

Figure 6.3: Simple Arrhenius and compensated Arrhenius(at T_r=45°C) plots for 0.3 mol kg^{-1} LiTf-octanone solutions.

to get meaningful activation energy values. These data also support the idea that ion transport is governed by a single activated process in these electrolyte solutions. The master curve was plotted for arbitrarily chosen E_a values to determine the sensitivity of those values to produce a single master curve. The master curve for 0.3 m LiTf-acetate is observed only for a narrow range of E_a values (31-40 kJ mol^{-1}), while for 0.8 m master curve has a range of 28-37 kJ mol^{-1}. Similarly, the master curve for 0.3 m LiTf-ketone does result for E_a values within the range from 24-30 kJ mol^{-1}. It is interesting to note that the median value of all three ranges are close to average E_a values of those three systems.

The three curves in Fig. 6.5 are horizontally displaced from each other due to the different dielectric constant range encompassed by the concentrated acetate

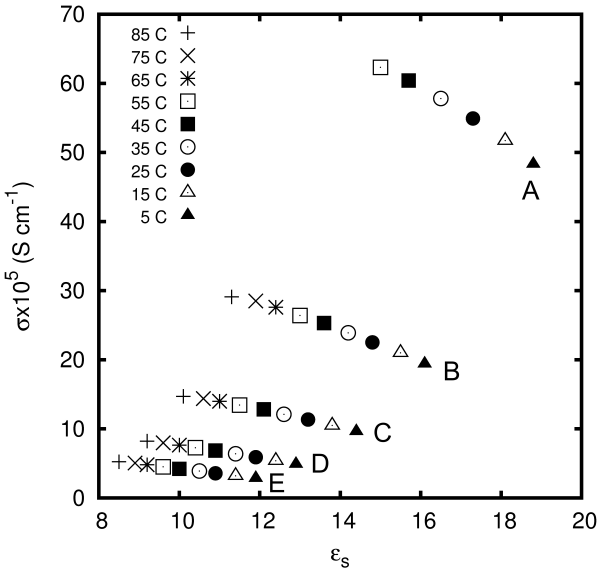

Figure 6.4: Conductivity versus static dielectric constant for 0.3 m LiTf-ketone solutions of (A) 2-hexanone (B) 2-heptanone (C) 2-octanone (D) 2-nonanone (E) 2-decanone over the temperature range 5 to 85°C.

and ketones solutions. The exponential prefactors for 0.3 m LiTf-ketones are larger than those for 0.3 LiTf-acetates. Further, the higher the concentration, the higher the dielectric constant range for each acetate family member over the temperature interval 5 to 85°C. This is in contrast with the TbaTf-alcohol solutions studied by Fleshman *et. al.* [21]. This is mainly due to the fact that alcohols are strongly self-associated through H-bonding and span a greater dielectric constant range even for low salt concentrations. In acetate-based electrolytes, the exponential prefactor is a weaker function of temperature for both low and high concentrations than ketone-based electrolytes. This non-negligible dependence of σ_0 is causes linear behavior in the Arrhenius plot of both concentrations.

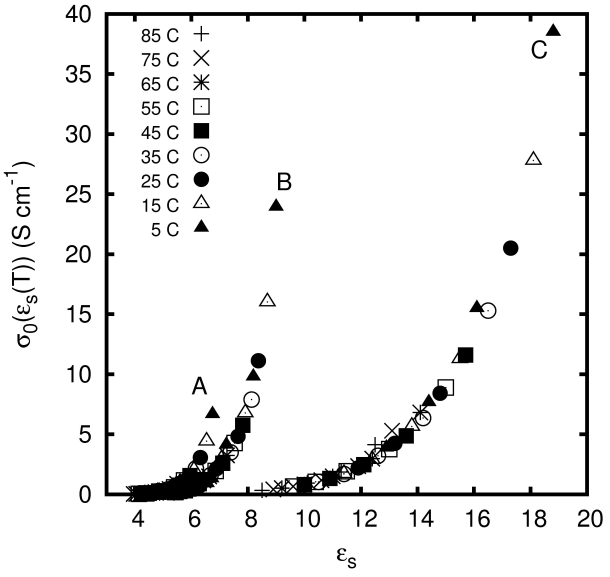

Figure 6.5: Exponential prefactor versus dielectric constant for (A) 0.3 m LiTf-acetate, $E_a = 35.4$ kJ mol^{-1} (B) 0.8 m LiTf-acetate, $E_a = 32.7$ kJ mol^{-1} (C) 0.3 m LiTf-ketone, $E_a = 26.1$ kJ mol^{-1}

Table 6.3: Activation energies from compensated Arrhenius plots from conductivity data for 0.3 m LiTf-ketones

		CAE E_a(kJ/mol)	
0.3 m LiTf Solvent	T_r (°C)	Slope	Intercept
2-heptanone	15	26.7± 1.0	26.7± 0.9
	25	25.8± 0.8	25.9± 0.8
	35	25.5± 0.6	25.6± 0.6
	45	26.5± 0.5	26.6± 0.5
2-octanone	45	26.0± 0.4	26.1± 0.4
	55	25.6± 0.4	25.7± 0.4
2-nonanone	65	26.2± 0.3	26.2± 0.3

6.3.2 Temperature dependent IR spectroscopic measurements

TbaTf-acetate/ketone solutions

Our previous study considered TbaTf-acetate and ketone based electrolytes. The most important observation is that TbaTf does not show discrete ionically associated species. Fig. 6.6 illustrates that temperature dependence of vibrational modes of acetates and ketones. The $\delta_s(CF_3)$ symmetric deformation mode of 0.2 mol kg^{-1} TbaTf-acetate is shown in Fig. 6.6(a). The single band visible at 753 cm^{-1} is attributed to the "free" ions. This band frequency is unchanged at all temperatures we measured. Similarly, the SO_3 symmetric stretching vibrational mode, $\nu_s(SO_3)$ of

0.2 TbaTf-heptanone is illustrated in Fig. 6.6(b). At each temperature, there is only one band observed at 1032 cm^{-1}, assigned to "free" ions. Both data clearly indicate that there is no ionic association in TbaTf-organic solvents when temperature changes.

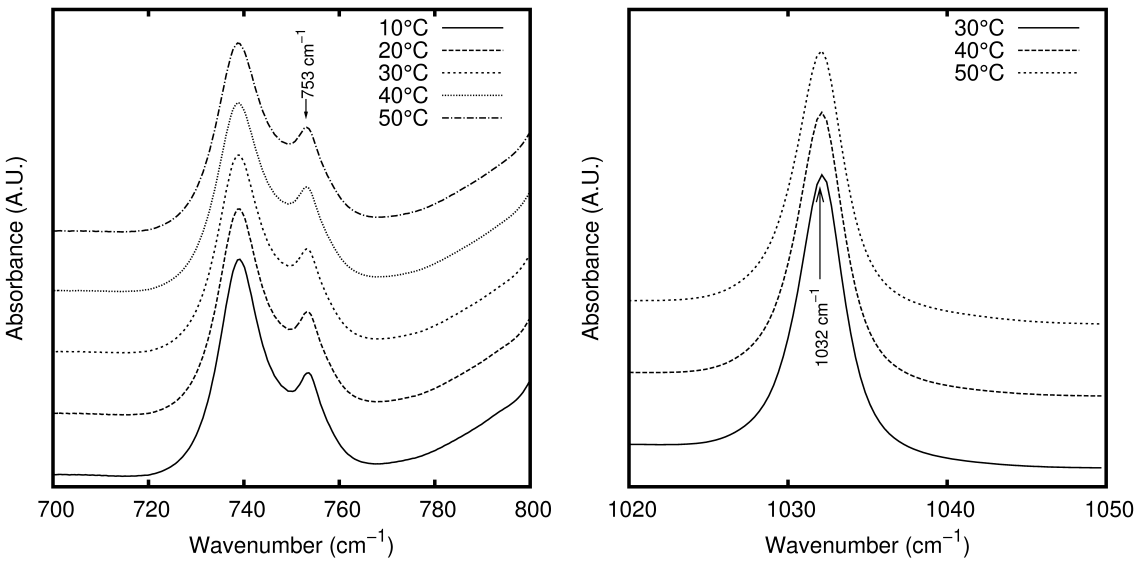

(a) **(b)**

Figure 6.6: (a) Temperature-dependent IR spectrum of 0.2 m TbaTf-butyl acetate solution for $\delta_s(CF_3)$ (b) Temperature-dependent IR spectrum of 0.2 m TbaTf-heptanone solution for $\nu_s(SO_3)$

LiTf-acetate solutions

In order to gain insight into the ionic association of LiTf-acetate and ketone solutions, temperature and concentration dependent spectroscopic studies were

carried out using Fourier Transform Infrared Spectroscopy.

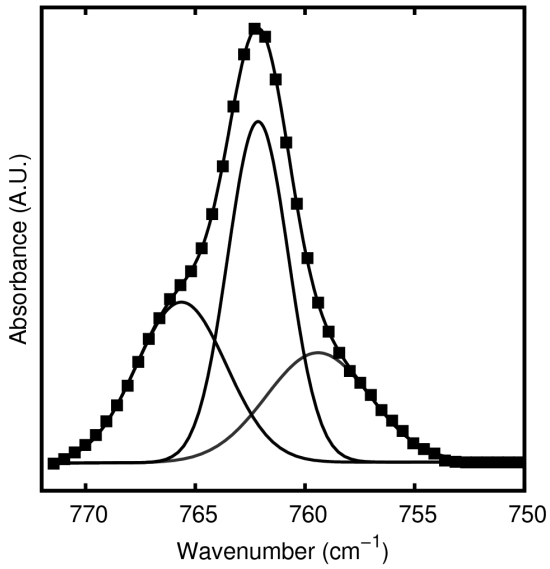

Figure 6.7: IR spectra of the symmetric CF_3 bending mode for 0.8 m LiTf-hexyl acetate at 35°C. (squares = experimental data, solid and dotted lines = fit from deconvolution analysis.)

Figure 6.7 shows the IR spectra of the non-degenerate symmetric bending or deformation mode, $\delta_s(CF_3)$, for LiTf-hexyl acetate in the 750-770 cm^{-1} spectral region. Three distinct bands were observed in this spectral mode corresponding to three different ionic species. The band at lower frequency (758-759 cm^{-1}) is attributed to contact ion pairs. The middle band at 762 cm^{-1} is due to either a triple cation (Li_2Tf^+) or a dimer (Li_2Tf_2). These spectroscopically indistinguishable ion species are described as aggregate I throughout the paper. The highest frequency band at 765-766 cm^{-1} is designated as aggregate II. According to Huang *et al.*, ion aggregate II is a Li_3Tf^{2+} entity and is observed in low dielectric, aprotic solutions [7]. The relative intensities of each species change with both temperature

and concentration. To study the temperature dependence of ionic species, IR spectra measured at different temperatures were curve-fitted using advanced non-linear curve fitting software (OriginPro 8.5). Gaussian functions were used to obtain the best fits for data. The relative band intensity or area fraction, defined as the ratio of each area to the total area of all the species, is calculated.

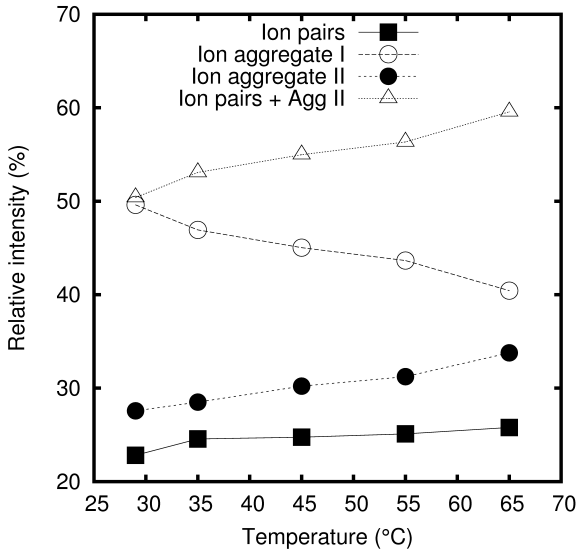

Figure 6.8: Relative intensity versus temperature for $\delta_s(CF_3)$ in 0.8 m LiTf-hexyl acetate

Figure 6.8 illustrates relative intensities of $\delta_s(CF_3)$ mode in 0.8 m LiTf-hexyl acetate as a function of temperature. The IR temperature data were collected three times for the 0.8 m LiTf-hexyl acetate sample and average intensities are reported in the Fig. 6.8. As the temperature increased, the relative intensities of contact ion pairs and aggregate II bands increased, while intensity of aggregate I decreased. The same behavior was observed for 0.8 m LiTf-butyl, octyl and decyl acetates.

These observations, can be described in terms of following mechanisms:

$2\ \{Li_2Tf\}^+ \longrightarrow \{Li_3Tf\}^{2+} + \{LiTf\}^0$

The superscript denotes the net charge of the ionic species. In this process, we assume that the ion aggregates I are present as triple ions $\{Li_2Tf\}^+$ in the sample. The spectroscopic data indicate that there is contact ion pairing between Li^+ cation and Tf^- anion. Ion pair formation is expected in acetates because it a low dielectric constant solvent.

The relative intensity change of the $\delta_s(CF_3)$ spectral mode for different acetate family members is shown in Fig. 6.9. All spectra were collected for a 0.8 molal concentration at 35°C temperature. The amount of ionic species at higher frequencies which are noted as ion aggregate II increase with the chain length of the acetate. Further, the amount of ion-pairs is higher in short-carbon chain acetates compared to the long-carbon chain acetates.

LiTf-ketone solutions

In ketones, the symmetric deformation mode, $\delta_s(CF_3)$ overlaps the solvent band at 762 cm^{-1}. Therefore, the SO_3 symmetric stretching vibrational mode, $\nu_s(SO_3)$ was analyzed in the spectral range from 1000 to 1100 cm^{-1} as shown in Fig. 6.10.

There are three components in this region for 0.3 m LiTf-heptanone. These component bands are assigned to "free" ions (1032-1033 cm^{-1}), contact ion pairs (1040-1041 cm^{-1}) and ion aggregates I (1048-1050 cm^{-1}). A weak shoulder was observed at 1060 cm^{-1} for LiTf in octanone, nonanone and decanone solutions. We believe this additional peak may be due to highly associated ion aggregates

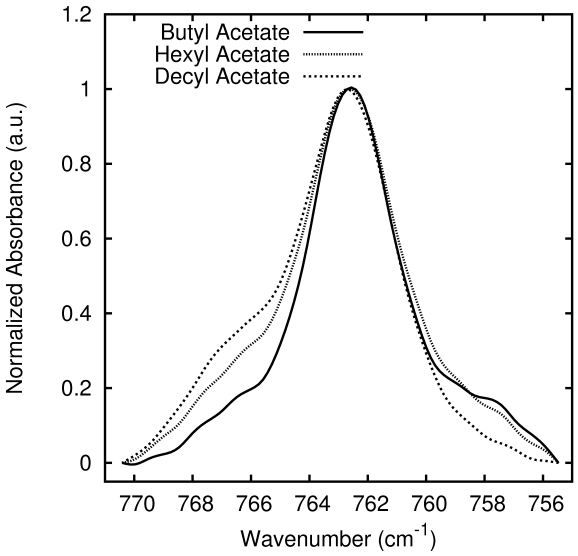

Figure 6.9: Relative intensity variation of $\delta_s(CF_3)$ spectral mode for 0.8 m LiTf-butyl, hexyl, and decyl acetates.

that appear in longer chain ketones. The estimated relative intensities of 0.3 m LiTf-heptanone are plotted as a function of temperature as shown in Fig. 6.11(a). In this figure, ion aggregate I and ion pairs are dominant in the solution while "free" ions are a minor species. We interpret these observations by proposing the following two temperature-dependent processes:

(1) 2 $\{LiTf\}^0 \longrightarrow \{Li_2Tf_2\}^0$ (dimers seem as ion aggregate I)

(2) $\{LiTf\}^0 \longrightarrow \{Li\}^+ + \{Tf\}^{1-}$

Based on the slower rate of appearance, the formation of the dimer, Li_2Tf_2, from two ion pairs (process 1) appears to be more favorable than the dissociation of the ion pairs to form "free" lithium and triflate ions (process 2).

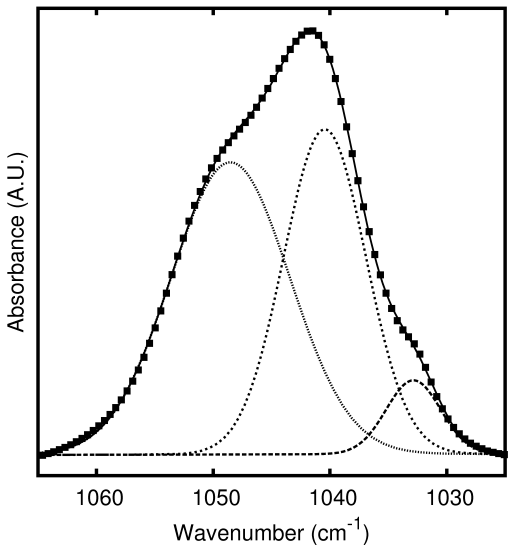

Figure 6.10: IR spectra of the $\nu_s(SO_3)$ mode in 0.3 m LiTf-heptanone at 45°C. (squares = experimental data, solid and dotted lines = fit from deconvolution analysis.)

The band assignment of the $\nu(SO_3)$ mode for LiTf-acetone has been previously studied by several research groups [9, 15]. Our band assignment is closer to that reported by Alia *et. al.*. Stevens *et. al.* reported four band components for LiTf-acetone molar ratio 16 at 300 K [9]. However, the broad band with a maximum at 1076 cm^{-1} was not seen in our spectra. Also, they suggested that the band located at 1051 cm^{-1} is due to the triplet species $Li^+Tf^{-1}Li^+$ [15].

Figure 6.11(b) shows the intensity change of the SO_3 band with increasing carbon chain length of ketones. Here the intensity of the high frequency band, which is designated as aggregate I, increases with chain length of the ketone.

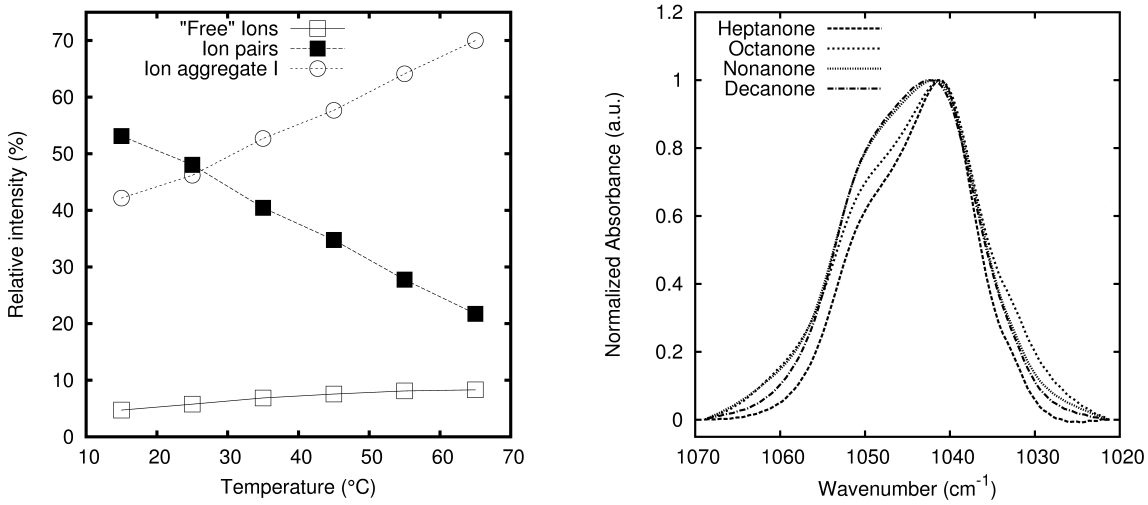

(a) **(b)**

Figure 6.11: (a) Relative intensity versus temperature for the $\nu_s(SO_3)$ mode in 0.3 m LiTf-heptanone. (b) Relative intensity variation of $\nu_s(SO_3)$ spectral mode for 0.3 m LiTf-heptanone, octanone, nonanone, and decanone.

CO stretch of LiTf-acetate and ketone solutions

The CO stretching vibrational mode, ν(CO), occurs as a strong IR absorption band in the region 1660-1800 cm^{-1}. The frequency depends on the potential energy environment of the CO group and the physical state of the sample. Fig. 6.12 shows the CO stretch band of the pure decyl acetate and a 0.3 m LiTf-decyl acetate solution. The single contour on the high wave number side (at 1744 cm^{-1}) is due to the ν(CO) of pure acetate. The small band at 1714 cm^{-1} results from the Li cation coordination with carbonyl group. The shift of 30 cm^{-1} indicates

a strong interaction between the lithium ion and the carbonyl oxygen atoms of the acetate molecules. Similar observations have been reported by Deng *et.al.* for $LiAsF_6$-methyl acetate solutions using Raman spectroscopy. According to their results, the CO stretching vibrational mode of methyl acetate shows a band at 1740 cm^{-1} and a shoulder at 1720 cm^{-1} due to the solvation of Li cation through carbonyl group in electrolyte solution [18]. Further, we studied the temperature dependence of CO stretching vibrational mode over the 25-75°C temperature range for 0.3 m LiTf-decyl acetate solution. The frequencies of the two ν(CO) bands were not changed when the temperature increases.

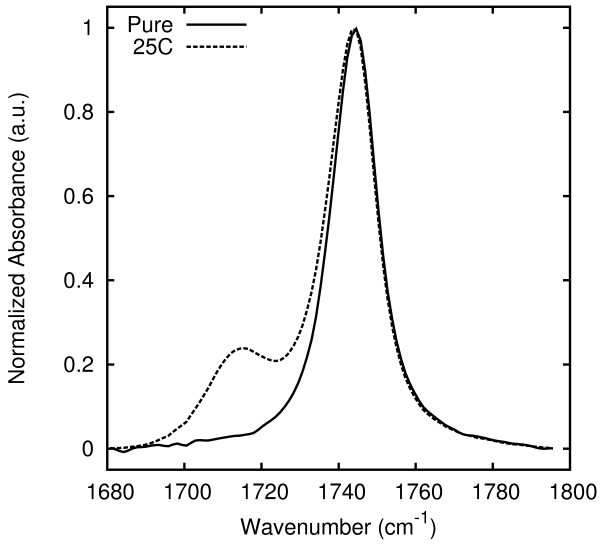

Figure 6.12: CO stretching vibrational mode of pure decyl acetate at 25°C and 0.3 m LiTf-decylacetate at 25°C and 75°C.

Similarly, IR spectra were observed for both pure ketone and LiTf-ketone electrolytes. Fig. 6.13(a) presents the CO stretching region for both pure octanone

and 0.3 m LiTf-octanone solutions. The two bands have a very similar asymmetric broad band features. However, the deconvoluted spectra for pure octanone shows two components under the asymmetric band, which shows a maximum peak at 1711-1713 cm^{-1}. This kind of band splitting can be expected due to the vibrational coupling between neighboring molecules [26]. As shown in the Fig. 6.13(b), deconvolution of 0.3 m LiTf-octanone band feature reveals the presence of two components, suggesting that the ketone molecule exists in two different environments. The band at 1712 cm^{-1} can be assigned to pure solvent. The new band at 1723 cm^{-1} is attributed to the Li solvated ketone molecules. In this case, 0.3 m is quite a low concentration to observe the two clearly separated bands compared to acetate solutions. Deng *et.al.* have reported the concentration dependence of $LiAsF_6$-acetone in the CO stretching region. For the electrolyte solution, they have observed two separate bands for concentration above 2.0 m. They suggested that the band on the high frequency side originates in cation solvation [27].

Equilibrium constants

As we mentioned earlier, some association-dissociation processes of ion species are observed in concentrated acetate and ketone solutions. The equilibrium constant of these processes can be determined by considering the equilibrium between different ion species. It is important to understand the concentration dependence of equilibrium constant of LiTf in acetate and ketone solutions. Petrowsky *et al.* reported equilibrium constants at various salt concentrations of diglyme-LiTf solutions. They showed that equilibrium constant for dimer formation is constant

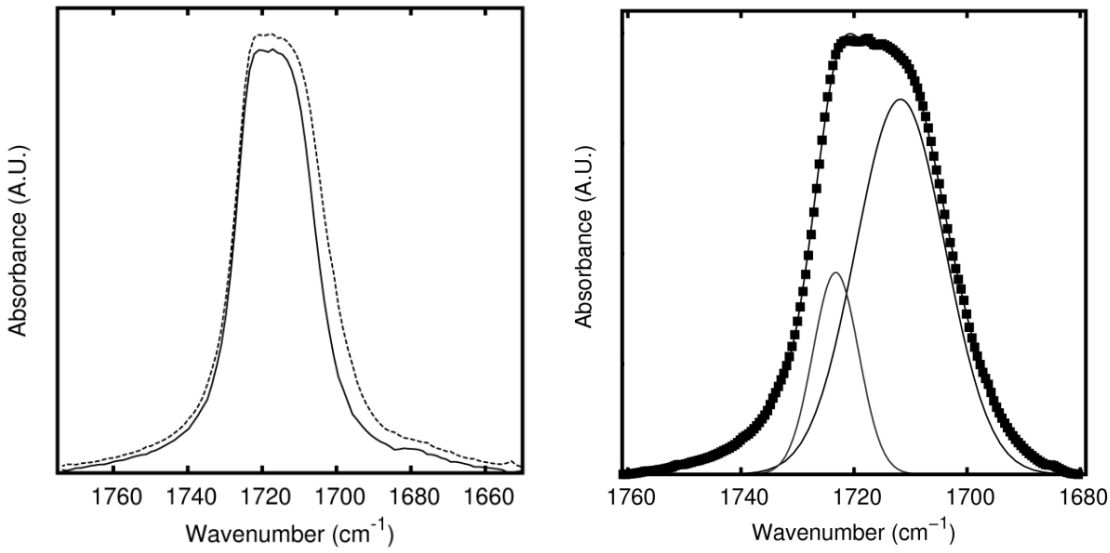

(a) **(b)**

Figure 6.13: (a) CO stretch vibrational mode of pure octanone(solid line) and 0.3 m LiTf-octanone(dash line) at room temperature.(b) Band deconvolution and component fitting in 0.3 m LiTf-octanone. (squares = experimental data, solid lines = fit from deconvolution analysis.)

over a wide range of concentrations [17]. In our case, equilibrium constants were determined for LiTf-n-hexyl acetate and LiTf-2-heptanone solutions. For the former solution, samples were prepared for three concentrations (0.3, 0.5, 0.8 m) and the latter solutions, four concentrations were used (0.3, 0.5, 0.7, 1.0 m). An equilibrium process between ion pairs and dimers can be written as follows [17]:

$2\ [LiTf]^0 \rightleftharpoons [Li_2Tf_2]^0$

Here, both species are electrically neutral. The equilibrium constant of this process can be calculated using following relation.

$$K = \frac{\gamma_{Li_2Tf_2} c_{Li_2Tf_2}}{(\gamma_{LiTf} c_{LiTf})^2} \tag{6.2}$$

Here $\gamma_{Li_2Tf_2}$ and γ_{LiTf} are the activity coefficients of Li_2Tf_2 and LiTf, respectively and are approximated as 1. $C_{Li_2Tf_2}$ and C_{LiTf} are the concentrations of Li_2Tf_2 and LiTf, respectively. Calculated equilibrium constants(K) for LiTf-n-hexyl acetate and LiTf-2-heptanone solutions are listed in table 6.4. Values of these constants decrease with salt concentration. This may be due to the formation of triple ions in addition to the simple equilibrium between ion pairs and dimers [17]. However this observation contradicts with the NMR results which are described in the next section. Neglecting activity coefficients may play a role in IR data.

Table 6.4: Equilibrium constants of LiTf-n-hexyl acetate and LiTf-2-heptanone solutions at different concentrations

total salt concentration-(mol/kg)	LiTf-hexyl acetate K(kg/mol)	LiTf-heptanone K(kg/mol)
0.3	2.84	0.99
0.5	2.67	0.80
0.7	2.05	-
0.8	-	0.71
1.0	1.59	-

^{7}Li and ^{19}F Self-diffusion measurements

Self-diffusion coefficients of cations(^{7}Li) and anions(^{19}F) in 0.3 m LiTf-2-heptanone solution were determined at room temperature (25°C). Calculated diffusion coefficients for Li^{+} and $CF_3SO_3^{-}$ ions in solution are virtually identical each other for the 0.3 m concentration (see table 6.5). Williamson *et al.* claim that fluorine diffusion coefficients are slightly greater than that of lithium at low salt concentrations for polymer electrolytes [28]. Similar values of anion and cation coefficients in different solvents has been observed by number of groups [28]. According to their suggestion, Li^{+} and $CF_3SO_3^{-}$ ions in ion pairs can move as single species with increasing ionic association. In addition, they suggested that there is a correlated motion of the anions and cations in neutral ion pairs or clusters. We believe that these suggestions are valid for our observations. Further, we proposed two possible processes based on our temperature-dependent IR data. According to both NMR and IR data, it may be concluded that observed ion aggregate I in 0.3 m LiTf-ketone solution as dimers. However, equilibrium constants described in previous section are not consistent with this argument. IR data indicate that there is triple ion formation with concentration.

Table 6.5: Values of self diffusion coefficients

0.3 m LiTf-heptanone	Diffusion coefficient (m^2s^{-1})
^{7}Li	4.15×10^{-10}
^{1}9F	4.11×10^{-10}

6.4 Conclusions

The results in this chapter are based on three major set of data: (1) temperature-dependent ionic conductivity measurements (2) concentration-dependant ionic conductivities (3) temperature-dependent and concentration-dependent measurements of ionic association. The purpose of this study was to understand temperature-dependent charge transport behavior in electrolytes that exhibits ionic association. A second purpose was to verify the validity of the compensated Arrhenius formalism in concentrated electrolytes. Ionic conductivities and dielectric constants were examined for 0.3 m LiTf-acetate, 0.8 m LiTf-acetate, 0.3 m LiTf-ketone systems. These data showed that dielectric constant of the pure solvent is significantly increased with the addition of LiTf. Both low and high concentrations of acetate-based electrolytes exhibit simple Arrhenius behavior due to the weaker dependance of σ_0 on temperature. However, a non-linear behavior is observed in the simple Arrhenius plot of 0.3 m LiTf-ketone due to the strong temperature dependence of σ_0. This strong temperature dependence arises through the temperature dependence of the dielectric constant. The results presented here (temperature-dependent ionic conductivities for both acetates and ketones) obey the compensated Arrhenius formalism. As expected, the ionic conductivity and the molar conductivity are observed to increase with concentration. The calculated activation energies are summarized in Table 6.6.

In the table, the activation energy appears to slightly decrease when the molal concentration increases. Further, the CAF E_a is slightly lower than that for 0.0055

Table 6.6: Values of activation energies from CAE plots

Solvent system	Average activation energy from CAE (kJ/mol)
0.3 m LiTf-acetate	35.4±0.6
0.8 m LiTf-acetate	33± 1
0.3 m LiTf-ketone	26.1 ± 0.6

M TbaTf-acetate solutions (36.5 kJ mol^{-1}) [3].

In the IR studies, ion-ion and ion-molecule interactions are observed for both ketone and acetate-based electrolytes. It is concluded that "free" ions, contact ion pairs and more highly associated ionic aggregates exist in LiTf-ketone solutions. Two types of ion aggregates are observed in LiTf-acetate solutions. These two distinct aggregates have been reported by a few other groups [7, 20]. It would be helpful to study crystal structures of acetates and ketone-based electrolytes with LiTf to understand the coordination bonds of these aggregate species. The longer the chain length of acetates, the higher the fraction of ion aggregates II. In contrast, the fraction of contact ion pairs decreases. Similarly, the relative amount of aggregate I is increased with the chain length of ketones. From IR spectra studies it is evident that there is contact ion pairing in both acetate and ketone solutions. Further, IR data of both LiTf acetates and ketones suggest that lithium cations are binding through the carbonyl functional groups.

Concentration-based equilibrium constants are estimated for both LiTf-acetate and ketone solutions assuming a simple equilibrium process between contact ion

pairs and dimers. Our results show that these values are changed with the total salt concentration. This behavior may be due to the neglect of activity coefficients; alternatively there may be equilibria between additional ionic species. PFG-NMR data show that the diffusion constants for ^{7}Li and ^{19}F are identical, suggesting the presence of contact ion pairs and dimers.

References

[1] J. G. Kim, E. G. Shim, and T. H. Nam, *Organic electrolytes for li-ion battery and li-ion battery comprising the same*, U.S. Patent 20100173186, July 2010.

[2] Y. Jan, L. Ho, S. Li, T. Hsieh, and W. Chuang, *Electrolytes for rechargeble battery*, U.S. Patent 2006/0121356 A1, June 2006.

[3] D. N. Bopege, M. Petrowsky, A. M. Fleshman, R. Frech, and M. B. Johnson, J. Phys. Chem. B **116**(1), 71 (2012).

[4] D. N. Bopege, M. Petrowsky, R. Frech, and M. B. Johnson, *Mass and ion transport in pure ketones and dilute ketone solutions* (2011), to be submitted.

[5] Y. Koga, H. Takahashi, and K. Higasi, Bull. Chem. Soc. Japan, **47**(1), 84 (1974).

[6] R. Frech and W. Huang, J. Sol. Chem **30**(4), 469 (1994).

[7] W. Huang and R. Frech, Polymer **35**(2), 235 (1994).

[8] G. Petersen, P. Jacobsson, and L. Torell, Electrochim. Acta **37**, 1495 (1992).

[9] J. R. Stevens and P. Jacobsson, Can. J. Chem. **69**, 1980 (1991).

[10] J. R. MacCallum and C. A. Vincent, *Polymer Electrolyte Reviews 1* (Elsevier Applied Science Publishers Ltd., 1987), 1st ed.

[11] J. R. MacCallum and C. A. Vincent, *Polymer Electrolyte Reviews 2* (Elsevier Applied Science Publishers Ltd., 1989), 1st ed.

[12] W. Huang, R. Frech, P. Johansson, and J. Lindgren, Electrochim. Acta **40**, 2147 (1995).

[13] Z. Chen and M. Hojo, J. Phys. Chem. B **101**, 10896 (1997).

[14] J. M. Alia, Y. D. de Mera, H. G. M. Edwards, F. J. Garca, and E. E. Lawson, J. Mol. Struct. **408-409**, 439 (1997).

[15] J. Alia and H. Edwards, Vib. Spectrosc. **24**, 185 (2000).

[16] M. Nicolas and R. Reich, J. Phys. Chem. **83**(6), 749 (1979).

[17] M. Petrowsky, R. Frech, S. N. Suarez, J. R. P. Jayakody, and S.Greenbaum, J. Phys. Chem. B **110**(46), 23012 (2006).

[18] Z. Deng and D. E. Irish, Can. J. Chem. **69**(11), 1766 (1991).

[19] R. Frech, S. York, H. Allcock, and C. Kellam, Macromolecules **37**, 8699 (2004).

[20] S. York, R. Frech, A. Snow, and D. Glatzhofer, Electrochim. Acta **46**(10-11), 1533 (2001).

[21] A. M. Fleshman, M. Petrowsky, J. D. Jernigen, R. Bokalawela, M. B. Johnson, and R. Frech, Electrochim. Acta **57**(0), 147 (2011).

[22] M. Petrowsky and R. Frech, J. Phys. Chem. B **114**(26), 8600 (2010).

[23] M. Petrowsky and R. Frech, J. Phys. Chem. B **113**(17), 5996 (2009).

[24] M. Petrowsky and R. Frech, Electrochim. Acta **55**(17), 1285 (2010).

[25] M. Petrowsky and R. Frech, J. Phys. Chem. B **113**(17), 16118 (2009).

[26] G. Fini and P. Mirone, J. Chem. Soc. **70**, 1776 (1974).

[27] Z. Deng and D. E. Irish, J. Chem. Soc. Faraday Trans. **88**(19), 2891 (1992).

[28] M. J. Williamson, H. V. S. A. Hubbard, and I. M. Ward, Polymer **40**(26), 7177 (1999).

Chapter 7

Vibrational Spectroscopic and X-Ray Crystallographic Study of Secondary Amine/Phosphoric Acid Systems

7.1 Introduction

Linear and branched poly (ethyleneimine) (PEI, -CH_2CH_2NH-)-acid systems have been widely studied during past few years because of their potential as polymeric proton conductors [1–4]. It has been shown that the membranes made from these materials exhibit good proton conducting properties. Glatzhofer *et al.* [1] reported IR studies for LPEI-HCl/H_3PO_4 systems. This work concluded that NH groups of PEI form hydrogen bonds with oxygen atoms of phosphoric acid due to protonation. This gives rise to NH_2^+ stretching modes between 2000 and 2500 cm^{-1} in the IR spectrum. Further, they suggested that the membranes made from LPEI-HCl/H_3PO_4 could be used as electrolytes in H_2/air fuel cells. An understanding of the proton transport mechanism is important to make well-functioning proton exchange membranes. However, due to the complex structure of polymer electrolytes, it is very difficult to identify various factors that affect the proton transport mechanism. Therefore, model compounds are used to explain the parts of the local structure of polymer electrolytes [5–9]. In particular, the crystal structures of these model compounds provide insight into the local structure or chemical environment of the polymer segments. Amine hydrohalide salts and amine-acid systems are good candidates to examine the hydrogen bond network.

Since H_3PO_4 is a promising electrolyte in the fuel cell industry, it is useful to study the secondary amine-H_3PO_4 systems. However, no previous study has obtained crystal structures or vibrational assignments for these systems. The aim of the present work is to understand the hydrogen bonding network of secondary amine-phosphoric acid model compounds. Particularly, protonation of nitrogen atoms in the backbone of the amine leads to hydrogen bonding that can be observed in the NH stretching mode and the NH bending mode. These modes can generally be recognized using Fourier Transform Infrared (FTIR) and Raman spectroscopy. This study also provides essential insight needed to understand many other vibrational modes of amine/phosphate materials.

A number of groups have studied IR vibrational modes of protonated amino groups in different regions. They observed strong IR bands of NH_2^+ stretching vibrational modes in the region 2000-2900 cm^{-1} for secondary amine salts [10–12]. Furthermore, authors observed weak band features in 2000-2900 cm^{-1} that were assigned as strong overtone and combination bands. Other IR bands in the region of 1500-1700 cm^{-1} have been observed, which were assigned to the NH_2^+ deformation (scissors) mode [10–13].

In this chapter, crystal structures for three secondary amine/phospheric structures are presented. We studied diethylamine ($CH_3CH_2NHCH_2CH_3$), piperazine ($C_4H_{10}N_2$), and N,N'- dimethylethylenediamine ($C_4H_{12}N_2$) complexed with phosphoric acid. All three amines are secondary amines. Piperazine is the simplest cyclic member of the ethyleneamine family and has two secondary amine groups. Three crystal structures were solved by single crystal X-ray diffraction methods.

Examination of the vibrational spectra of these crystals revealed distinct broad IR bands at 2300-2600 cm^{-1} for the NH_2^+ stretching mode and bands at 1500-1700 cm^{-1} for the NH_2^+ bending mode. This clearly agrees with literature values for PEI-acid systems. Therefore, these model compounds can be used to study future fuel cell candidates. In addition, vibrational assignments for H_3PO_4 ion species were studied.

7.2 Experimental Methods

7.2.1 Sample preparation

The N,N' dimethylethylenediamine (DMEDA) and diethyleneamine (DEA) were obtained from Aldrich. Piperazene was purchased from Alfa Aesar. The sample solution was prepared by adding a weighted amount of concentrated phosphoric acid and pure amine solvent into distilled water. All samples were stirred for a few hours before use. All solution samples were reported as an amine:phosphoric acid molar ratio ($N:H^+$). During this study three samples were prepared with 1:1, 2:1, and 3:1 $N:H^+$ ratio for each compound. Crystals were formed by a slow evaporation process of solution after 1-2 weeks. The crystals were observed in 2:1 and 3:1 samples for both DEA and DMEDA compounds. However, crystals were formed in 1:1 and 2:1 solutions of piperazine.

7.2.2 X-ray crystallography

Intensity data of crystal samples were collected using a diffractometer with a Bruker APEX CCD area detector and graphite-monochromated Cu Kα radiation (λ = 1.54178 Å) [14, 15]. The sample was cooled to 100(2)K. Cell parameters were determined from a non-linear least-squares fit, and the data were corrected for absorption by the semi-empirical method giving minimum and maximum transmission factors [16]. The triclinic space group was determined by statistical tests and verified by subsequent refinement. The structure was solved by direct methods (SHELXTL) and refined by the full-matrix least squares method on F^2 [17, 18]. Hydrogen atom positions were initially determined by geometry and refined by a riding model. Non-hydrogen atoms were refined with anisotropic displacement parameters. Hydrogen atom displacement parameters were set to 1.2 (1.5 for methyl) times the displacement parameters of the bonded atoms. In this study, all structural data were obtained only for 2:1 crystals of each compounds.

DEA:phosphoric acid

A total of 182 parameters were refined against 2886 points to give wR(F^2) = 0.0878 and S = 1.128 for weights of w = 1/[σ (F^2) + (0.0480 P)^2], where P = [F_o^2 + 2F_c^2]/3. The final R(F) was 0.0328 for the 2481 observed, [F > 4σ(F)], data. The largest shift/s.u. was 0.001 in the final refinement cycle. The final difference map had maxima and minima of 0.308 and -0.321 e/3, respectively.

DMEDA:phosphoric acid

A total of 147 parameters were refined against 3390 points to give wR(F^2) = 0.1416 and S = 1.011 for weights of w = $1/[\sigma\ (F^2) + (0.0760\ P)^2 + 0.3600\ P]$, where P = $[F_o^2 + 2F_c^2]/3$. The final R(F) was 0.0530 for the 2838 observed, [F > 4σ(F)], data. The largest shift/s.u. was 0.000 in the final refinement cycle. The final difference map had maxima and minima of 0.374 and -0.348 e/3, respectively.

Piperazine:phosphoric acid

A total of 130 parameters were refined against 2163 points to give wR(F^2) = 0.1804 and S = 1.057 for weights of w = $1/[\sigma^2\ (F^2) + (0.1240\ P)^2 + 0.2400\ P]$, where P = $[F_o^2 + 2F_c^2]/3$. The final R(F) was 0.0480 for the 1745 observed, [F > 4σ(F)], data. The largest shift/s.u. was 0.000 in the final refinement cycle. The final difference map had maxima and minima of 0.511 and -1.125 e/3, respectively.

7.2.3 Vibrational spectroscopy

The crystal and solution sample spectra were collected by using Fourier Transform Infrared and Raman spectroscopy. For IR measurements, a Bruker IFS66v spectrometer was used and all crystal sample data were recorded from 400 to 4000 cm^{-1} with a spectral resolution of 1 cm^{-1}, 64 scans with a KBr beam splitter, and a DTGS detector. Crystal samples were prepared as KBr pellets, which were made using a finely ground mixture of crystal and potassium bromide. All IR spectra for crystal samples were recorded under a vacuum (pressure=13 mbar). A thin sample layer sandwiched between two ZnSe windows was used to observe IR spectrum of

solutions. These samples were run under a dry air purge. The Raman spectra were collected using a Bruker Equinox 55 FRA 106/S. A Coherent Nd:YAG laser was used for excitation at a power level of 300 mW at 1064 nm. The crystal sample was packed in a NMR capillary tube and the spectra were taken at a spectral resolution 2 cm^{-1} with 1000 scans in the 50-3500 cm^{-1} range with a CCD detector.

7.3 Results and Discussion

7.3.1 Crystallographic structures

Both DEA:H_3PO_4 and DMEDA:H_3PO_4 crystals form triclinic unit cells belonging to the $P\bar{1}$ space group. The former has four asymmetric units in the unit cell and the latter two asymmetric units in the cell. Piperazene:H_3PO_4 crystal forms a monoclinic unit cell with the $P2_1/n$ space group, with four asymmetric units in the cell.

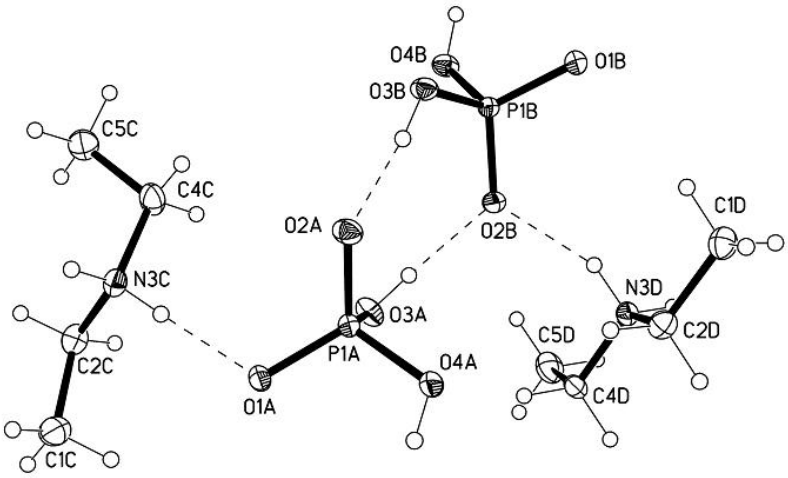

Figure 7.1: Asymmetric unit of DEA:H_3PO_4.

Fig. 7.1 shows the asymmetric unit of DEA:H_3PO_4. In this figure, the nitrogen atom from a single DEA molecule is protonated and makes a hydrogen bond

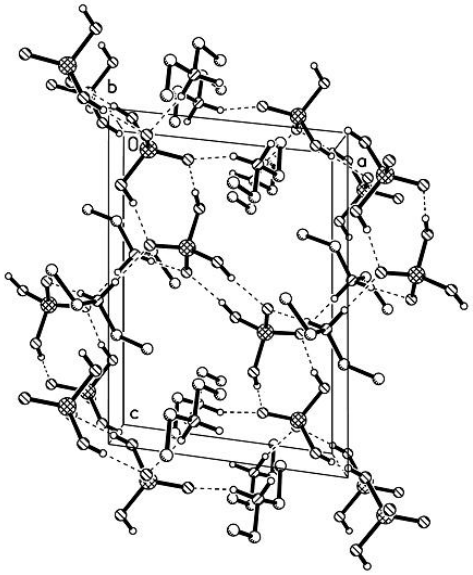

Figure 7.2: Packing diagram of the DEA:H_3PO_4 crystal structure

(N-H–O) between it and oxygen atom in phosphoric acid. Also, remaining oxygen atoms in H_3PO_4 form hydrogen bonds (O-H–O) with oxygen atoms from different H_3PO_4 molecules. The packing diagram is shown in Fig. 7.2. All four ammonium hydrogen atoms form hydrogen bonds with oxygen. Two (N-H–O) bonds have the same bond lengths and angles while the other two have different values. This may be due to different environments of the ammonium hydrogen atoms.

The hydrogen bond network in the DMEDA:H_3PO_4 crystal structure is presented in Fig. 7.3(a). Both N atoms are protonated and make hydrogen bonds with the oxygen atoms of H_3PO_4. Two water molecules contained in the system coordinate with oxygen atoms from H_3PO_4 molecule, forming a very complex crystal structure. Only four hydrogens out of the eight ammonium hydrogens make hydrogen bonds in this structure, and their bond angles and lengths differ from each other. According to the diagram in Fig. 7.3(b), DMEDA:H_3PO_4 crystals are packed in a polymeric one-dimensional network along the crystallographic c axis.

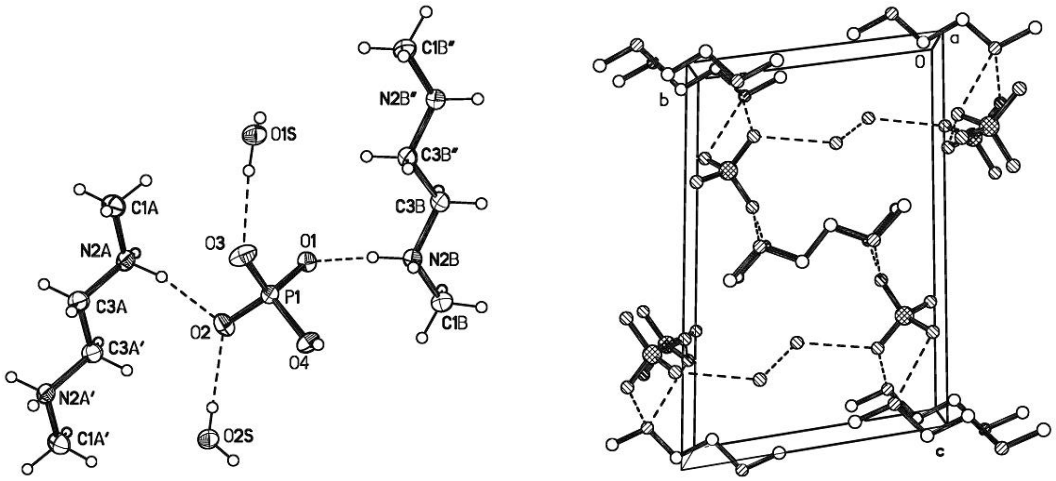

Figure 7.3: (a) Asymmetric unit of DMEDA:H_3PO_4. (b) Packing diagram of the DMEDA:H_3PO_4 crystal structure

The third crystal structure was obtained for piperazine:H_3PO_4 as shown in Fig. 7.4(a). Piperazine compound is different from the other two secondary amines due to its six membered ring structure. Even though it has a complex structure, both nitrogen atoms of the piperazine form hydrogen bonds with the oxygens from the H_3PO_4 molecule. The asymmetric unit of the cell contained two half cations, one anion and one water molecule. The water molecule is coordinated with the one of the oxygen atoms from H_3PO_4. Fig 7.4(b) presents the packing diagram of the piperazine:H_3PO_4 crystal structure.

The detailed parameters of these three crystal structures are given in table 7.1

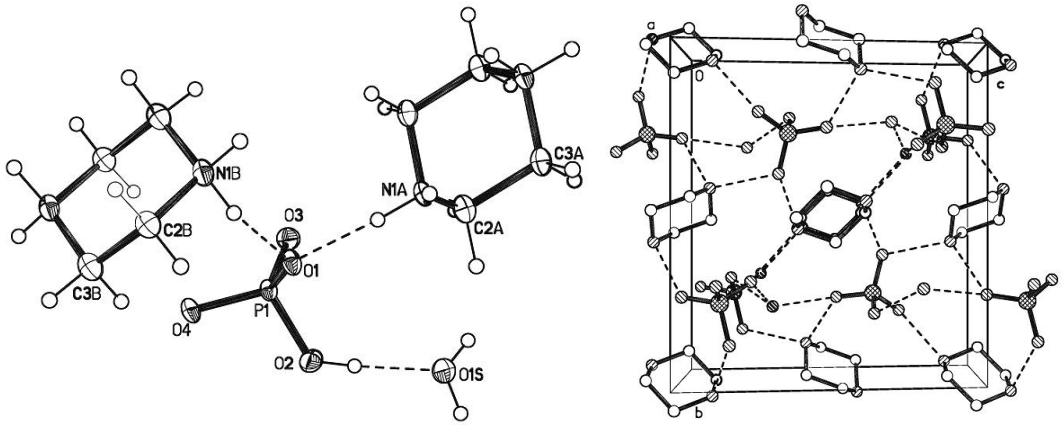

(a) **(b)**

Figure 7.4: (a) Asymmetric unit of piperazine:H_3PO_4. (b) Packing diagram of the piperazine:H_3PO_4 crystal structure

7.3.2 Vibrational spectroscopy

The three crystal structures provide a deep insight into the local structures and their hydrogen bond networks. The parallel studies of IR and Raman spectra of DEA:H_3PO_4, DMEDA:H_3PO_4 and piperazene:H_3PO_4 were used to probe the nature of the amino group hydrogen-bonding network and their interactions with phosphoric acid. In this study, IR spectra of two spectral regions were analyzed: the NH_2^+ stretching vibrational modes in the range of 2200-2600 cm^{-1} and NH_2^+ bending vibrational modes in the range of 1500-1700 cm^{-1}. Both IR modes are very sensitive to hydrogen bonding.

The crystal structure formation of 2:1 DMEDA:H_3PO_4 compound was investigated. Fig. 7.5(a) shows the IR spectra of neat DMEDA, phosphoric acid/water solution and crystal structure of DMEDA:H_3PO_4 in the spectral region from 2200 to

Table 7.1: Structural data for crystal structures

Parameters	DEA:H_3PO_4	DMEDA:H_3PO_4	Piperazene:H_3PO_4
Crystal system	Triclinic	Triclinic	Monoclinic
Space group	$P\bar{1}$	$P\bar{1}$	$P2_1/n$
Temperature(K)	100(2)	100(2)	100(2)
a	8.2884(4)	4.6531(12)	6.372(4)
b	8.7311(4)	8.6765(16)	12.215(7)
c	11.5419(6)	13.171(2)	11.150(7)
α	89.381(6)	80.822(6)	90
β	82.995(6)	82.411(8)	96.958(14)
γ	79.229(7)	81.967(9)	90
Volume(A^3)	814.35(7)	516.50(18)	861.5(9)
Z	4	2	4
Density(Mg/m^3)	1.396	1.429	1.559
R1	0.0328	0.0530	0.0480
crystal size(mm^3)	0.34×0.26× 0.08	0.52×0.24× 0.14	0.49×0.42× 0.24

2600 cm^{-1}. This figure also shows the time evolution of this band of DMEDA:H_3PO_4 solution after 6 hours, 1 day, and 2 days. The broad band feature appeared after 6 hours in the region of 2200-2600 cm^{-1}. After 48 hrs, the intensity of this band was increased, and the broad band split into two components in the crystal DMEDA:H_3PO_4. These bands are attributed to the NH_2^+ stretching vibrational mode. Specially, the NH_2^+ stretching mode is sensitive to the hydrogen bonding

interactions, which increases the dipole moment derivatives, leading to prominent IR bands. Similarly, IR spectra in the region of 1400-1800 cm^{-1} are shown in Fig. 7.5(b). Mixed band features were observed in this region due to NH_2^+ stretching and the OH stretching modes. It was noted that the intensity of the OH band decreases and the NH_2^+ stretching band intensity increases with time.

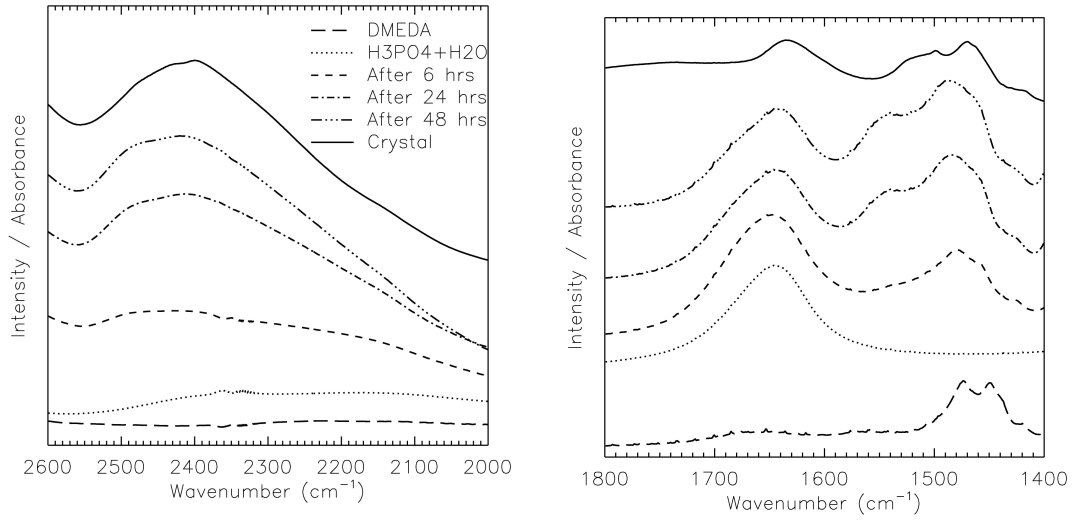

(a) **(b)**

Figure 7.5: (a) IR spectra of DMEDA:H_3PO_4 in the region 2200-2600 cm^{-1} (b) IR spectra of DMEDA:H_3PO_4 in the region 1400-1800 cm^{-1}

NH_2^+ stretching band region, $\nu(NH_2^+)$

In general, free NH stretching vibrations for secondary amines can be observed between 3000 cm^{-1} and 3400 cm^{-1} as a single band. For a complex structure like amine:H_3PO_4, NH_2^+ stretching bands are shifted to the lower frequency side of the

NH stretching vibrational modes. Fig. 7.6 illustrates the IR and Raman spectra of the NH_2^+ stretching region (2200-2600 cm^{-1}) for three crystalline structures (DEA:H_3PO_4, DMEDA:H_3PO_4 and piperazene:H_3PO_4).

DEA:H_3PO_4

Figure 7.6(a) shows the IR spectrum of NH_2^+ stretch mode for DEA:H_3PO_4 crystal structure. The four bands appear at 2518, 2468, 2408 and 2379 cm^{-1} in this IR spectrum within ± 1 cm^{-1} uncertainty. It is important to note that, while two bands are well separated, the other two are broadened with similar intensities in the IR spectrum. This behavior may be due to the different ammonium hydrogen environments in the crystal structure. The Raman spectrum contains a strong band at 2518 cm^{-1} and a weak shoulder at 2422 cm^{-1}. These features appear in both IR and Raman spectra due to the protonation of a secondary amine. Early studies revealed that the band on the higher frequency side can be attributed to the symmetric NH_2^+ stretch mode and that on the lower frequency side corresponds to asymmetric NH_2^+ stretch mode [19].

According to group theory, the NH_2^+ vibrational stretching modes can be classified in terms of irreducible representations of the C_i unit cell group as follows:

$\Gamma(\nu(NH_2)^+) = 2A_g + 2A_u$.

This predicts two infrared active modes and two Raman active modes for each $\nu_s(NH_2^+)$ and $\nu_{as}(NH_2^+)$ vibrations in the crystal structure. However, four IR active modes and two Raman active modes were observed in the spectra. The IR spectrum suggests that there is vibrational coupling between the asymmetric units

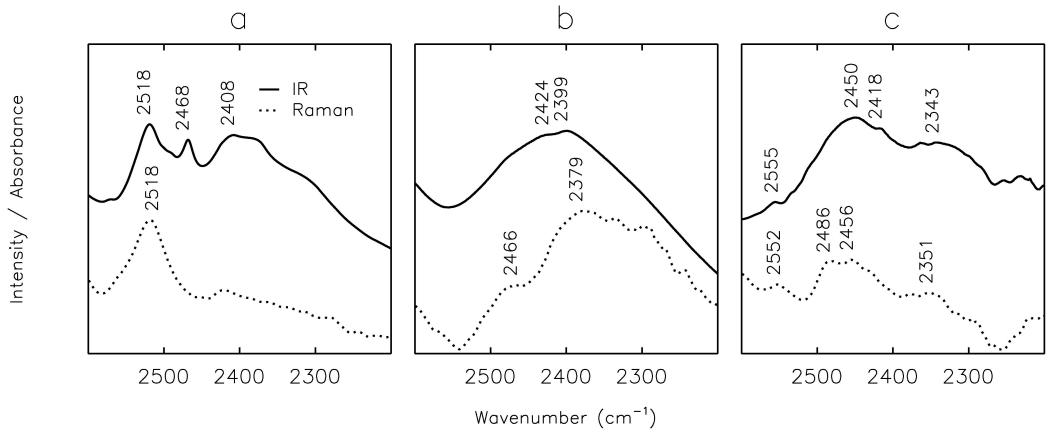

Figure 7.6: Symmetric $(NH_2)^+$ stretching mode of (a) DEA:H_3PO_4 (b) DMEDA:H_3PO_4 (c) Piperazene:H_3PO_4

in the unit cell. In the IR and Raman spectra, many sub maxima are observed with low intensities. These kind of bands can appear due to combination or overtone bands or due to disorder in crystal symmetry.

It is also noted that N-H stretching band at 2518 cm^{-1} is both Raman and IR active, despite their different intensities. Usually symmetrical modes tend to be Raman active and hence appear as strong peaks in the spectrum. Therefore, one expects distinct Raman peaks for symmetric vibrational modes. The infrared band at 2408 cm^{-1} appears to correspond with the Raman band at 2422 cm^{-1} in the higher frequency side. The maximum shift ($\Delta\nu$) of the bands was approximately 14 cm^{-1}. In the Fig. 7.6(a), Raman bands were not observed for the two IR bands at 2468 and 2379 cm^{-1}. This behavior can be interpreted as a result of the mutual exclusion principle. According to this rule, IR active modes are strictly Raman inactive, while Raman active modes are strictly IR inactive, if there is a center of symmetry of the crystal structure. It is reasonable to suggest that NH_2^+ stretching

vibrational modes obey the mutual exclusion principle and hence the crystal has a crystallographic symmetry.

DMEDA:H_3PO_4

Figure 7.6(b) shows the IR and Raman spectra of the NH_2^+ stretching mode in DMEDA:H_3PO_4 crystal. In contrast to the DEA:H_3PO_4 vibrational data, broad band features were observed in the region of 2200-2600 cm^{-1}. In the IR spectrum, two bands were centered at 2424 and 2399 cm^{-1}, while the Raman spectrum contains two bands at 2466 and 2379 cm^{-1}.

The N-H stretching modes in DMEDA:H_3PO_4 can be described according to the irreducible representations of the C_i ($P\bar{1}$ space group) unit cell group as:

$\Gamma(\text{N-H}) = 2A_g + 2A_u$.

Similarly, O-H vibrational modes can be classified using the following irreducible representations:

$\Gamma(\text{O-H}) = 2A_g + 2A_u$.

This suggests that mixed vibrational modes of N-H stretching and OH stretching may occur between 2200 and 2600 cm^{-1}. On the other hand, four amino hydrogens do not form hydrogen bonds as mentioned earlier. Accordingly, DMEDA:H_3PO_4 molecules undergo minimal or no hydrogen-bonding interactions and hence, very little spectral change can be expected. These two scenarios can explain the strong and broadened band features in both the IR and Raman spectra. In the DMEDA:H_3PO_4 spectra, all band intensities appears to obey the mutual exclusion rule resulting from the crystallographic center of symmetry of the crystal structure.

Piperazine:H_3PO_4

The IR spectrum of the piperazine:H_3PO_4 crystal shows four prominent band features at 2555, 2450, 2418 and 2343 cm^{-1} (see Fig. 7.6(c)). In the Raman spectrum, four bands are observed at 2552, 2486, 2456, and 2351 cm^{-1}. Both IR and Raman vibrational modes appear to be poorly resolved and a significant amount of frequency shifts were noted as well. This behavior is a result of the intermolecular coupling of NH vibrational modes in the unit cell. The piperazine:H_3PO_4 crystal structure belongs to the $P2_1/n$ (C_{2h}) space group. $(NH_2)^+$ stretching modes can be classified according to the irreducible representation of the C_{2h} unit cell group as:

$\Gamma(\nu(NH_2)^+)) = 2A_g + 2B_g + 2A_u + 2B_u$.

The group theory analysis predicts four infrared-active (A_u and B_u) modes and four Raman-active (A_g and B_g) modes for piperazine:H_3PO_4 spectra. Several weak intensity bands appearing in this region may be attributed to overtones and combination bands. The band intensities of both structures(in Fig. 7.6 b and c) appears to obey the mutual exclusion rule. Glatzhofer *et al.* showed that broad band features between 2200 to 2500 cm^{-1} for polymer electrolytes based on cross-linked LPEI-HCl/H_3PO_4 systems and that are ascribed to NH_2^+ vibrations. Further, they suggested that the oxygen atoms in the phosphate species coordinates with NH group of PEI via hydrogen bonding [1, 20]. These results give supporting evidence to the our IR spectroscopic data.

NH_2^+ deformation region, $\delta_s(NH_2^+)$

Figure 7.7 presents the IR and Raman spectra of DEA:H_3PO_4, DMEDA:H_3PO_4 and piperazene:H_3PO_4 in the range 1500-1700 cm^{-1}. The bands located in this region can be assigned to the symmetric NH_2^+ deformation mode, which is also known as NH_2^+ scissoring mode. As shown in Fig. 7.5(b), these bands overlapp with the OH bend mode of the water molecules. The DEA:H_3PO_4 crystalline structure (Fig. 7.7(a)) has two IR bands at 1624 and 1591 cm^{-1}. Raman bands appear at 1630 and 1607 cm^{-1}. Bands at lower frequencies are attributed to the NH_2^+ deformation mode, while higher frequency side bands correspond to the OH bending mode. Only a single band is found at 1635 cm^{-1}. Similar to the DEA:H_3PO_4 spectra, two Raman bands were observed for the piperazene:H_3PO_4. Here, IR band at 1632 cm^{-1} and Raman bands at 1649 and 1633 cm^{-1}.

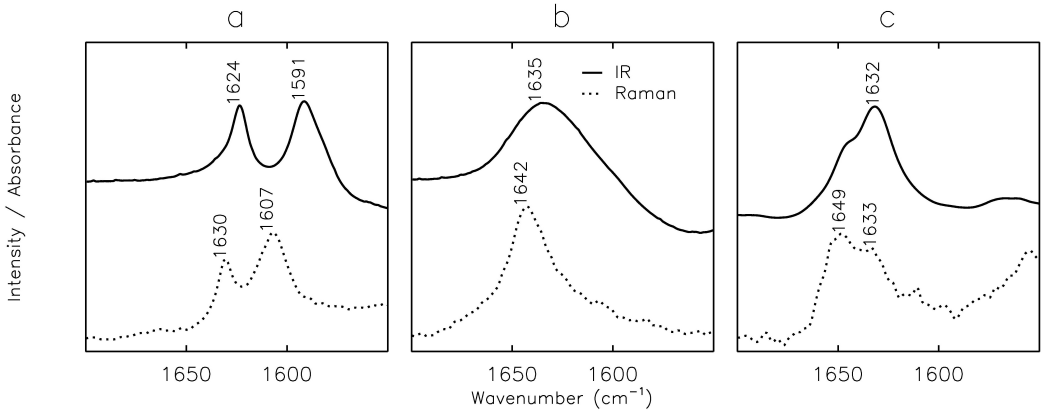

Figure 7.7: Symmetric $(NH_2)^+$ deformation mode of (a) DEA:H_3PO_4 (b) DMEDA:H_3PO_4 (c) Piperazene:H_3PO_4

H_3PO_4 acid species

Aqueous phosphoric acid and orthophosphoric acid have been extensively studied using Raman and IR spectroscopy [21–24]. In general, H_3PO_4 can be dissociated into three species in an aqueous solution: dihydrogen phosphate($H_2PO_4^-$), monohydrogen phosphate(HPO_4^{2-}), and phosphate(PO_4^{3-}). Vibrational spectroscopy was used to examine the abundance of phosphoric species in the amine:H_3PO_4 compounds. PO_4^{3-} exhibits T_d symmetry while HPO_4^{2-} and $H_2PO_4^-$ possesses C_{3v} and C_{2v} symmetry, respectively. The "free" phosphate ion(PO_4^{3-}) consists of nine vibrational modes. The irreducible representations of this vibrational mode can be described as:

$\Gamma(T_d) = a_1 + e + 2f_2$.

According to group theory, two infrared-active modes and four-Raman active modes can be assigned for phosphate ions (ν_1, ν_2, ν_3, ν_4). Previous studies reveal that an IR band appears at 540-560 cm^{-1} due to the ν_4 mode. Further, Raman bands at 900-1100 can be attributed to ν_1 and ν_3 modes, and the peak at 400 cm^{-1} corresponds to the ν_2 mode in the Raman spectrum [21–24].

Both IR and Raman spectra of DEA:H_3PO_4, DMEDA:H_3PO_4 and piperazene:H_3PO_4 crystals in two regions are shown in Fig. 7.8(left) and (right). These regions can be used to extract details about the phosphate ion species. In Fig. 7.8(right), several Raman bands are shown in the 900-1100 cm^{-1}, which probably correspond to ν_1 and ν_3 vibrations of PO_4^{3-} ion. Most of the IR and Raman bands observed in the 1200-800 cm^{-1} region may be due to the stretching vibration of P-O and

P-OH bonds. It is also noted that bands around 400-500 are due to ν_2 and ν_4 vibrational modes. $HPO_4{}^{2-}$ and $H_2PO_4{}^{-}$ can be produced by the acid dissociations [1, 21, 22, 25, 26]. In the 1000-1100 cm^{-1} region, a number of sharp Raman bands are located. These bands may be attributed to the $H_2PO_4{}^{-}$ anions [21–24]. These spectral data clearly indicate that phosphate vibrational modes are primarily a mixture of different H_3PO_4 species in these samples. Therefore, it is difficult to precisely interpret these vibrational modes.

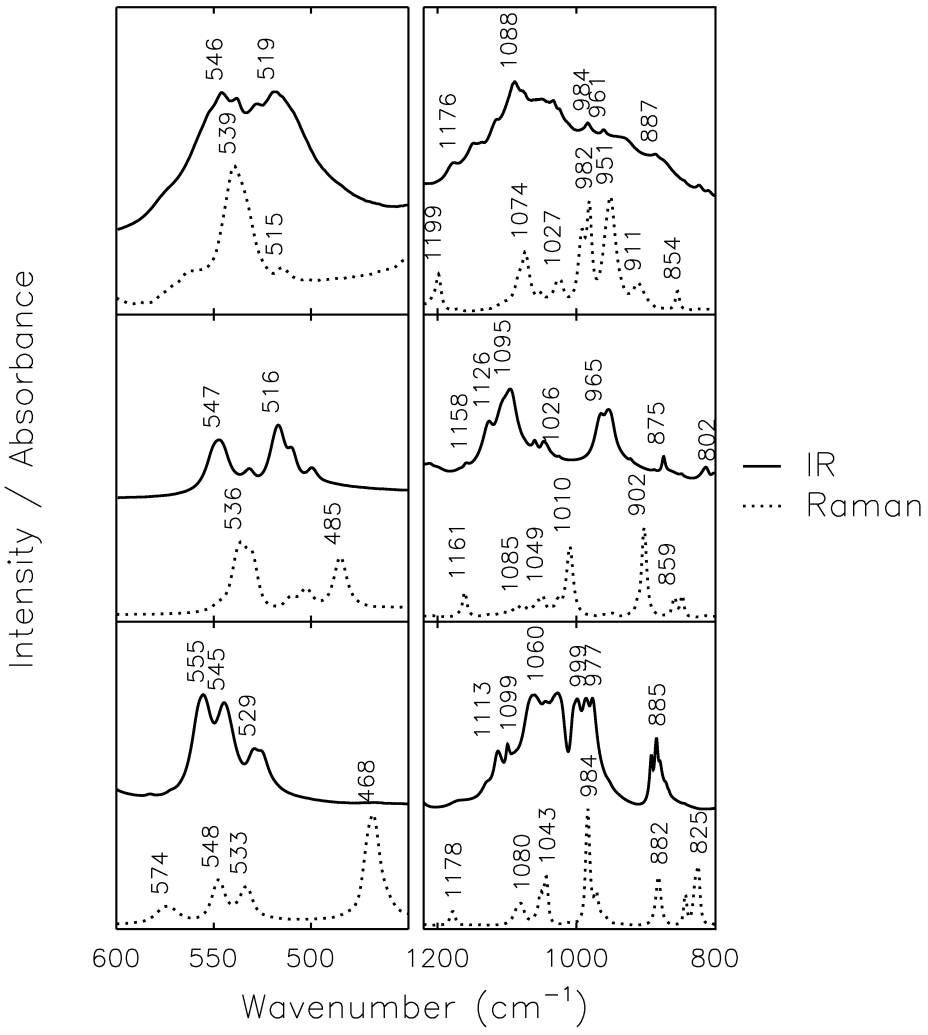

Figure 7.8: Abundance of Phosphate species (a) DEA:H_3PO_4 (b) DMEDA:H_3PO_4 (c) Piperazene:H_3PO_4

7.4 Conclusions

In this study, three crystal structures are reported for DEA:H_3PO_4, DMEDA:H_3PO_4, piperazene:H_3PO_4. We arrive at several conclusions from the results. Strong bands are observed in the NH stretching frequency region due to the strong H-bonding between Nitrogen atom of amine and the oxygen atom from the phosphoric acid. Both NH_2^+ stretching vibrations and NH_2^+ deformations can be observed as a result of amine protonations. All three crystal form N-H–O hydrogen bonds. In addition, there are O-H–O bonds due to the interaction between water and phosphoric molecule. Many weak bands were noticed in the 2200- 2600 cm^{-1} region and they can be assigned as strong overtone and combination bands. Spectroscopic evidence supports the presence of hydrogen bonding interactions between secondary amine and H_3PO_4. These results are in good agrement with the crystallographic data.

References

[1] D. Glatzhofer, M. Erickson, R. Frech, F. Yepez, and J. Furneaux, Solid State Ionics **176**, 2861 (2005).

[2] R. Tanaka, H. Yamamoto, A. Shono, K. Kubo, and M. Sakurai, Electrochim. Acta **45**(8), 1385 (2000).

[3] R. Tanaka, H. Yamamoto, A. Shono, K. Kubo, and M. Sakurai, Electrochim. Acta **40**(13-14), 2421 (2000).

[4] M. Daniel, B. Desbat, F. Cruege, O. Trinquet, and J. Lassegues, Solid State Ionics **28-30**, 637 (1988).

[5] S. S. York, S. E. Boesch, R. A. Wheeler, and R. Frech, Macromolecules **36**(19), 7348 (2003).

[6] N. M. Rocher, R. Frech, and D. R.Powell, J. Phys. Chem. B **110**(31), 15117 (2006).

[7] N. M. Rocher and R. Frech, J. Phys. Chem. A **111**, 2662 (2007).

[8] R. A. Sanders, R. Frech, and M. A. Khan, J. Phys. Chem. B **108**(34), 12729 (2004).

[9] R. A. Sanders, R. Frech, and M. A. Khan, J. Phys. Chem. B **108**(7), 2186 (2004).

[10] B. Chenon and C. Sandorfy, Can. J. Chem. **36**, 1181 (1958).

[11] R. A.Heacock and L. Marion, Can. J. Chem. **34**, 1782 (1956).

[12] C. Brissette and C. Sandorfy, Can. J. Chem. **38**, 34 (1960).

[13] R. J. Mureinik and W. Robb, Spectrochim. Acta **24A**, 377 (1968).

[14] *Data Collection: SMART Software Reference Manual*, Bruker-AXS, 5465 E. Cheryl Parkway, Madison, WI 53711-5373, USA (1998).

[15] *Data Reduction: SAINT Software Reference Manual*, Bruker-AXS, 5465 E. Cheryl Parkway, Madison, WI 53711-5373, USA (1998).

[16] G. M. Sheldrick, *SADABS. Program for Empirical Absorption Correction of Area Detector Data.*, University of Göttingen, Germany (2007).

[17] G. M. Sheldrick, Acta Cryst. **A 64**, 112 (2008).

[18] *International Tables for Crystallography*, vol. C (Tables 6.1.1.4, 4.2.6.8, and 4.2.4.2, Kluwer: Boston, 1995).

[19] G. A. Giffin, S. Boesch, D. N. Bopege, D. R. Powell, R. A. Wheeler, and R. Frech, J. Phys. Chem. **113**, 15914 (2009).

[20] M. J. Erickson, *Synthesis, Structure and Electrochemical Performance of Poly(ethylenimine)-based Electrolytes*, Ph.D. thesis, University of Oklahoma, The Department of Chemistry and Biochemistry, Norman (2004).

[21] A. Zwick, F. Lakhdar-Ghazal, and J.-F. Tocanne, J. Chem. Soc., Faraday Trans. 2 **85**, 783 (1989).

[22] Y. Kameda, K. Sugawara, T. Hosaka, T. Usuki, and O. Uemura, Bull. Chem. Soc. Japan **73**(5), 1105 (2000).

[23] C. M. Preston and W. A. Adams, Can. J. Spectros. **22**(6), 125 (1977).

[24] M. Cherif, A. Mgaidi, N. Ammar, G. Vallée, and W. Fürst, J. Sol. Chem. **29**(3), 255 (2000).

[25] J. W. Akitt, N. N. Greenwood, and G. D. Lester, J. Chem. Soc. A pp. 2450–2457 (1971).

[26] W. L. Marshall and G. M. Begun, J. Chem. Soc., Faraday Trans. 2 **85**(12), 1963 (1989).

Appendix 1

Program 1

```
pro QfitNT_JF_zero
;File:71009_purePEO_norm.txt in F(normalized data,6 decimal friquencies)
file='071709_PEOLT_1to20_norm'
readcol,'F:\IDL\data\'+file+'.txt',x,r1,t30,t40,t50,t60,t70,t80
format='D,D,D,D,D,D,D,D'

tble=dblarr(n_elements(x),21)
tble(*,0)=x
tble(*,1)=r1
tble(*,2)=t30
tble(*,3)=t40
tble(*,4)=t50
tble(*,5)=t60
tble(*,6)=t70
tble(*,7)=t80
;S-G smooting 3rd order 10 pts before & after
;Find min values between pklft:pklft1 & pkrgt1:pkrgt
;Choose 20 pts on either side of min(min moves with T)
;Fit to quadratic polynomial F(x)= Cx^2+Bx+A to this range
;find position of minX=-b/2*c
;Find minx, miny both sides
savgolFilter =savgol(10,10,0,3,/double)
minlx=dblarr(16)
minly=dblarr(16)
minrx=dblarr(16)
minry=dblarr(16)
pklft=min(where(tble(*,0) le 617d));664
pkrgt=min(where(tble(*,0) le 740d));732
pklft1=min(where(tble(*,0) le 628d));682
pkrgt1=min(where(tble(*,0) le 730d));718

A = FINDGEN(16) * (!PI*2/16.)
USERSYM, COS(A), SIN(A),/fill
!x.thick=3
!y.thick=3
!p.thick=2
!p.charsize=1.0
!p.charthick=1.5
!x.charsize=1.1
!y.charsize=1.1
device,set_font='Times',/TT_FONT
plotPosition = ASPECT(1.0/1.0)
area=dblarr(8)

for i=1,7 do begin
tble(*,i)=CONVOL(tble(*,i), savgolFilter, /EDGE_TRUNCATE)
minlft=pklft1+where(tble(pklft1:pklft,i) eq min(tble(pklft1:pklft,i)))
minrgt=pkrgt+where(tble(pkrgt:pkrgt1,i) eq min(tble(pkrgt:pkrgt1,i)))
rngl=tble(minlft-20:minlft+20,i)
      rnglx=tble(minlft-20:minlft+20,0)
```

```
rngr=tble(minrgt-20:minrgt+20,i)
rngrx=tble(minrgt-20:minrgt+20,0)

n=n_elements(rnglx)
sx=total(rnglx)
sx2=total(rnglx*rnglx)
sx3=total(rnglx*rnglx*rnglx)
sx4=total(rnglx*rnglx*rnglx*rnglx)
sy=total(rngl)
syx=total(rngl*rnglx)
syx2=total(rngl*rnglx*rnglx)
tmpl=invert([[n,sx,sx2],[sx,sx2,sx3],[sx2,sx3,sx4]])##[[sy],[syx],[syx2]]
a1=tmpl(0)
b1=tmpl(1)
c1=tmpl(2)
minlx(i)=-b1/(2d*c1)
minly(i)=a1+b1*minlx(i)+c1*minlx(i)*minlx(i)
n=n_elements(rngrx)
sx=total(rngrx)
sx2=total(rngrx*rngrx)
sx3=total(rngrx*rngrx*rngrx)
sx4=total(rngrx*rngrx*rngrx*rngrx)
sy=total(rngr)
syx=total(rngr*rngrx)
syx2=total(rngr*rngrx*rngrx)

tmpr=invert([[n,sx,sx2],[sx,sx2,sx3],[sx2,sx3,sx4]])##[[sy],[syx],[syx2]]
a2=tmpr(0)
b2=tmpr(1)
c2=tmpr(2)
minrx(i)=-b2/(2d*c2)
minry(i)=a2+b2*minrx(i)+c2*minrx(i)*minrx(i)
;Find slope and intercept of the line bet two points
;Fit a linear
;Subtract linear fit from original spectrum data
;repeat the procedure for other peaks
;Write the xmin,ymin values for a file in figPEO
;integrate
slope=(minry(i)-minly(i))/(minrx(i)-minlx(i))
intcpt=minry(i)-slope*minrx(i)
tble(pkrgt:pklft,i)=tble(pkrgt:pklft,i)-(intcpt+slope*tble(pkrgt:pklft,0))
x=tble(pkrgt:pklft,0)
y=tble(pkrgt:pklft,i)
area(i-1)=int_tabulated(x,y,/sort)
if (i eq 1) then plot,tble(pkrgt:pklft,0),tble(pkrgt:pklft,i),$
title=file+'(peak_region_JF)',$
xstyle=2,background='FFFFFF'x,color='000000'x,POSITION=plotPosition
if (i ne 1) then oplot,tble(pkrgt:pklft,0),tble(pkrgt:pklft,i),color='000000'x
endfor

lftstr=strtrim(string(tble(pklft,0)),1)
tmp=strsplit(lftstr,".",/extract)
lftstr=tmp(0)
rgtstr=strtrim(string(tble(pkrgt,0)),1)
```

```
tmp=strsplit(rgtstr,".",/extract)
rgtstr=tmp(0)
taxis=[20,30,40,50,60,70,80]

im1=tvrd()
write_jpeg,'F:\IDL\figPEO\'+file+lftstr+'_'+rgtstr+'_'+'.jpeg',im1
plot,taxis,area,psym=8,xtitle='Temperature',ytitle='Integrated Intensity',$
xstyle=2,background='FFFFFF'x,color='000000'x,POSITION=plotPosition,$
title=file+'(area_JF)'+lftstr+'_'+rgtstr
im2=tvrd()
write_jpeg,'F:\IDL\figPEO\'+file+'_area_JF'+lftstr+'_'+rgtstr+'_'+'.jpeg',im2

end
```

Program 2: Adapted from Liu et al.

```
pro QfitLT_Liu

ncol = 10
file='071409LiTF_PEO_norm'
readcol,'F:\IDL\data\'+file+'.txt',x,r1,t1,t2,t3,t4,t5,t6,t7,t8,t9,$
format='D,D,D,D,D,D,D,D,D,D',/silent

tble=dblarr(n_elements(x),11)
tble(*,0)=x
tble(*,1)=r1
tble(*,2)=t1
tble(*,3)=t2
tble(*,4)=t3
tble(*,5)=t4
tble(*,6)=t5
tble(*,7)=t6
tble(*,8)=t7
tble(*,9)=t8
tble(*,10)=t9

;S-G filtering 3rd order 10 pts before & after
savgolFilter =savgol(10,10,0,3,/double)
pklft_k = 1400.
pkrgt_k = 1200.
pklft = min(where(x le pklft_k))
pkrgt = min(where(x le pkrgt_k))
tble3=dblarr(pkrgt-pklft+1,11)
;this hold only the data of the peak of all the columns
tble3(*,0)=tble(pklft:pkrgt,0)
area=dblarr(ncol)

for i=1,ncol do begin ;do the same for all columns
tble2=dblarr(pkrgt-pklft+1,2)
 ;this is where we do the smoothing using S-G filter
tble(*,i)=CONVOL(tble(*,i), savgolFilter, /EDGE_TRUNCATE)
tble2(*,0)=tble(pklft:pkrgt,0)
tble2(*,1)=tble(pklft:pkrgt,i)
err=0.5d ;initilize the err(or) for the WHILE loop to run
```

```
while (err gt 0.0005d) do begin
tmpx=tble2(*,0)
;Following are the matrix elements needed to get the quadratic least square fit
n=n_elements(tmpx)
sx=total(tmpx)
sx2=total(tmpx*tmpx)
sx3=total(tmpx*tmpx*tmpx)
sx4=total(tmpx*tmpx*tmpx*tmpx)
sy=total(tble2(*,1))
syx=total(tble2(*,1)*tmpx)
syx2=total(tble2(*,1)*tmpx*tmpx)
;Finding fitting parameters a,b,c
tmp=invert([[n,sx,sx2],[sx,sx2,sx3],[sx2,sx3,sx4]])##[[sy],[syx],[syx2]]
a=tmp(0)
b=tmp(1)
c=tmp(2)
;Find the standard error, s
sqdev=total((tble2(*,1)-(a+b*tmpx+c*tmpx*tmpx))^2)
s=sqrt(sqdev/(n_elements(tmpx)-3))
tmp=temporary(tble2) ;deleting table tble2
;Find the indices of the data points where the deviations are
;smaller than the standard errors
igood=where((tmp(*,1)-(a+b*tmpx+c*tmpx*tmpx)) lt s,count)
tble2=dblarr(count,2)
;now tble2 holds the "good" data points
tble2(*,0)=tmp(igood,0)
tble2(*,1)=tmp(igood,1)
tmpx=tble2(*,0)
;err is the average deviation per point. This is the
;quantity we are minimizing
err=total(abs(tble2(*,1)-(a+b*tmpx+c*tmpx*tmpx)))/count
endwhile

tmpx=tble(pklft:pkrgt,0)
tble3(*,i)=tble(pklft:pkrgt,i)-(a+b*tmpx+c*tmpx*tmpx)
pkmax=max(tble3(*,i))
xmax=where(tble3(*,i)eq pkmax)
minlft=min(tble3(0:xmax,i))
xminlft=where(tble3(0:xmax,i)eq minlft)
minrgt=min(tble3(xmax:*,i))
xminrgt=xmax+where(tble3(xmax:*,i)eq minrgt)
x=tble3(xminlft:xminrgt,0)
y=tble3(xminlft:xminrgt,i)
area(i-1)=int_tabulated(x,y,/sort)
endfor
avg=MEAN(area)
taxis=[20,30,40,50,60,70,80,100,120,140]
A = FINDGEN(17) * (!PI*2/16.)
USERSYM, COS(A), SIN(A),/fill
!x.thick=3
!y.thick=3
!p.thick=3
!p.charsize=1.0
!p.charthick=1.5
```

```
!x.charsize=1.1
!y.charsize=1.1
device,set_font='Times',/TT_FONT
plotPosition = ASPECT(1.0/1.0)
lftstr=strtrim(string(tble(pklft,0)),1)
tmp=strsplit(lftstr,".",/extract)
lftstr=tmp(0)
rgtstr=strtrim(string(tble(pkrgt,0)),1)
tmp=strsplit(rgtstr,".",/extract)
rgtstr=tmp(0)
plot,taxis,area,psym=8,xtitle='Temperature',ytitle='Integrated Intensity',$
title=file+'(Liu)'+' '+rgtstr+' to '+lftstr,xstyle=2,$
background='FFFFFF'x,color='000000'x,POSITION=plotPosition
err=dblarr(n_elements(area))
err(*)=stddev(area)
oploterr,area,err
im=tvrd()
write_jpeg,'F:\IDL\figPEO\'+file+'(Liu)'+lftstr+'_'+rgtstr+'.jpeg',im
openw, datfile2, 'F:\IDL\figPEO\'+file+'(Liu)'+lftstr+'_'+rgtstr+'.txt',/get_lun
for i=0,n_elements(area)-1 do begin
printf, datfile2, taxis(i),area(i)
endfor
free_lun,datfile2

end
```

Appendix 2

List of abbreviations

PEO Poly(ethylene oxide)
LiTf Lithium trifluoromethanesulfonate, Lithium triflate
TbaTf Tetrabutylammonium trifluoromethanesulfonate
CH_3CN Acetonitrile
KBr Potassium bromide
DMEDA N, N'-dimethylethylenediamine
DEA Diethylamine
LPEI Linear poly(ethyleneimine)
PEM Proton exchange membrane
H_3PO_4 Phosphoric acid
$\nu_s(NH_2{}^+)$ Symmetric $NH_2{}^+$ stretch mode
$\nu_{as}(NH_2{}^+)$ Asymmetric $NH_2{}^+$ stretch mode
FTIR Fourier transform infrared spectroscopy
NMR Nuclear magnetic resonance
PFG NMR Pulsed field gradient nuclear magnetic resonance
MIR Mid infrared
$\delta_s(CF_3)$ CF_3 symmetric deformation mode
$\nu_s(SO_3)$ SO_3 Symmetric stretch mode
CAE Compensated Arrhenius equation
CAF Compensated Arrhenius formalism
T_g Glass transition tempearture
T_r Reference temperature
T Absolute temperature
c Concentration
D Self-diffusion coefficient
k_B Boltzmann's constant
ε Dielectric constant of solvent medium
ε_0 Dielectric constant of vacuumm
ε_s Relative dielectric constant
λ Wavelength
Λ Molar conductivity
σ Conductivity
E_a Activation energy
σ_0, D_0 Conductivity and diffusion exponential prefactors
C Capacitance